Simulating sprouting angiogenesis

using a new 3D substrate dependent cell-based model

F.D. (Frans) Bookholt

Delft University of Technology

Delft University of Technology

Challenge the future

SIMULATING SPROUTING ANGIOGENESIS

USING A NEW 3D SUBSTRATE DEPENDENT CELL-BASED MODEL

by

F.D. (Frans) Bookholt

in partial fulfillment of the requirements for the degree of

Master of Science
in Applied Mathematics

at the Delft University of Technology,
to be defended publicly on Friday February 13, 2015 at 16:00.

Supervisor:	Dr. Ir. F.J. Vermolen	
Thesis committee:	Dr. Ir. F.J. Vermolen,	Delft University of Technology
	Prof. Dr. Ir. C. Vuik,	Delft University of Technology
	Dr. Ir. J.L.A. Dubbeldam,	Delft University of Technology

This thesis is confidential and cannot be made public until Februari 13, 2015.

A digital version of this thesis is available at `http://repository.tudelft.nl/`.

Delft
University of
Technology

PREFACE

The result of 9 months of work to conclude my studies in Delft lies before you. It has become a project that, I hope, will be appealing to both mathematicians and (theoretical) biologists. Doing my own research has proven to be so much more fun than following courses and doing exams and I hope my enthusiasm is reflected in this work. I want to say thank you to everyone where thanks is due.

Fred, thanks for our great collaboration. It was wonderful to see during meetings how you, within the first five minutes, divided my work in useful things and things I needed to improve upon. Our meetings were insightful and I hope that near the end of the project we were thinking at the same pace concerning this project. I would love to see where the research on mathematical biology goes in the future.

Hanneke, thanks for giving me hands-on insight in biochemistry. I would have never guessed a year ago that I would learn the lab protocol to wash my hands threefold before separating dermis from adipose tissue with a tiny scalpel. Bringing scientific disciplines together can be challenging and I hope not to have annoyed you more than I intended with strange mathematical questions. I have learned a tremendous amount from working together with you and I hope reversibly some of my thoughts may stick around in the lab. And last but not least, thanks for all the cake.

Thanks to my graduation committee for reviewing my work and their interest in the subject.

Seb, thanks for the substantive thinking along with my project where needed (I hopefully fulfilled this role reversibly) and for your remarkably overlapping taste in music. I have enjoyed drawing small crab figures in between your notes on the white board.

Thanks to all of my house mates for keeping up with my endless twaddle about mathematics and cell biology. Special thanks are due to Floris for letting me use the cluster computer of his department. It has saved me a lot of time and it contributed greatly to the variance and sensitivity analyses.

Thanks to Ruben en Astrid for proof reading the concepts of this work.

Thanks to my parents for letting me live my life in Delft very independently and supporting me along the way in the choices I made.

Thanks to my sisters, who I both love dearly.

F.D. (Frans) Bookholt
Delft, February 2015

CONTENTS

Preface iii

Nomenclature vii

1 Introduction 1

2 Angiogenesis 3
- 2.1 In vivo angiogenesis. 3
- 2.2 Setup of the in vitro sprouting assay 4
- 2.3 Driving forces on cells in sprouting angiogenesis 5
  - 2.3.1 Chemotaxis 5
  - 2.3.2 Cell-cell forces 6
  - 2.3.3 Cell-matrix forces 6
  - 2.3.4 Gravity 7

3 Existing Models for angiogenesis 9
- 3.1 The cellular Potts model 9
- 3.2 Continuum models 10
- 3.3 Semi-stochastic cell-based model. 11
  - 3.3.1 Haptotaxis 11
  - 3.3.2 Proliferation 12
  - 3.3.3 Random movement 13
  - 3.3.4 Elastic contact movement 13
- 3.4 Comparison of the model types 13

4 A new 3-D substrate dependent cell-based model (SDCBM) 15
- 4.1 Feedback processes in the SDCBM 15
- 4.2 System of PDE's governing the chemicals and substrate components 16
  - 4.2.1 Boundary values and Initial conditions 18
  - 4.2.2 Solving the system of PDEs and time stepping 18
- 4.3 Substrate dependent cell movement 19
  - 4.3.1 Haptotaxis and contact mechanics in a 3D setting 20
  - 4.3.2 Chemotaxis 21
  - 4.3.3 Cell-matrix adhesion. 22
  - 4.3.4 Gravity 22
  - 4.3.5 Diffusion. 23
- 4.4 Tip cell selection and controlling motility 23
  - 4.4.1 Cell differentiation 23
  - 4.4.2 Different motility tips and stalks 25
- 4.5 Parameters and Domain 25
- 4.6 Data visualization. 27
  - 4.6.1 Chemical slices plot 27
  - 4.6.2 Cells plot. 27
  - 4.6.3 Iso-surface plot 28
  - 4.6.4 Microscopic plot 29
- 4.7 Initial distribution cells 30

5 Results 33
5.1 Model mechanics . . . 33
5.2 Metrics for the amount of sprouting . . . 36
5.3 Estimators for the mean of the metrics . . . 36
5.4 Sensitivity analysis . . . 40
5.4.1 Varying the initial concentration VEGF c_V^0 . . . 40
5.4.2 Varying the protease sourcing rates s_U and s_M . . . 40
5.4.3 Varying the maximal rate of tip cell selection p_{ST} . . . 41
5.4.4 Varying the adhesive scaling constant $\hat{\lambda}$ . . . 41
5.4.5 Varying the elasticity of the substrate E_F . . . 41
5.5 Comparison to the in vitro work . . . 47
5.6 Vasculogenesis-like structure formation . . . 48

6 Conclusions and Recommendations 51
6.1 Conclusions. . . . 51
6.2 Discussion and recommendations . . . 51

A Glossary of biochemical terms and processes 55
A.1 Processes . . . 55
A.2 Physiological definitions . . . 55
A.3 Substances . . . 56

B CPM implementation 57
B.1 Differential equations governing the chemicals . . . 57
B.2 Initial conditions . . . 58
B.3 Stochastic degrading of the substrate . . . 58
B.4 Stochastic elongation of the cells . . . 59
B.5 Results . . . 59

C The FEM for the PDE layer 61
C.1 Galerkin equations for the PDE of c_M . . . 61
C.2 Linear basis functions. . . . 63
C.3 (Approximate) Integration over tetrahedra . . . 63
C.4 Barycentric coordinates, linear interpolation and Dirac delta integration . . . 63
C.5 The elements matrices and vectors for the PDE of c_M . . . 64
C.6 Rest of the element matrices and vectors . . . 66
C.6.1 Element matrices M^{e_l} for the time derivative . . . 66
C.6.2 Element matrices S^{e_l} for the spacial derivatives . . . 67
C.6.3 Element vectors . . . 67

D Cell movement time stepping algorithm 69

E Numerical Considerations 71
E.1 Implicit/Explicit (IMEX) time stepping for PDEs . . . 71
E.2 Meshing and node numbering . . . 72
E.3 Truncation very low substrate densities . . . 73
E.4 Spurious oscillations on source terms using Holand-Bell . . . 73
E.4.1 Proof existence time step and grid size independent spurious oscillations in 1D. . . . 74
E.4.2 Adding diffusion to smear out the oscillations . . . 76
E.4.3 Compensating the spurious oscillations by other numerical schemes . . . 77
E.5 On the equilibrium points and stability of the PDEs. . . . 77

F Computational model options 79

Bibliography 81

NOMENCLATURE

ATECs	Adipose Tissue Endothelial Cells - Endothelial cells derived from fat tissue, mostly from adipose human subjects.
bFGF	basic Fibroblast Growth Factor - An angiogenic growth factor secreted by fibroblasts.
BM	Basement Membrane or Boundary Membrane. A fibrous structure underneath ECs consisting laminin and type IV collagen
CPM	Cellular Potts model
DLL4	Delta-like ligand 4
DTECs	Dermal Tissue Endothelial Cells - ECs derived from the dermis.
ECF	Extracellular Fluid
ECM	Extracellular Matrix - The mixture of proteins, growth-factors and carbohydrates surrounding cells *in vivo*
ECs	Endothelial Cells
FEM	Finite Element Method
MDGFs	Macrophage Derived Growth Factors
MMP	Matrix metalloproteinases - A group of proteases degrading the basement membrane
PDE	Partial Differential Equation
PDF	Probability Density Function
SDCBM	Substrate Dependent Cell-Based Model
TNF-α	Tumor Necrosis Factor alpha - A cytokine secreted by a variety of cells.
TST	Tissue Simulation Toolbox
uPA	urokinase-type Plasminogen Activator - Protease degrading fibrin.
VE-cadherin	Vascular Endothelial Cadherin
VEGF	Vascular Endothelial Growth Factor
VU	Vrije Universiteit

1

INTRODUCTION

Angiogenesis[1] is the biological mechanism by which new blood vessels sprout from existing ones. It differs from vasculogenesis, which is the *de novo* growth of the primary vascular network from initially dispersed endothelial cells (ECs). Vasculogenesis is predominant in embryonic tissue whilst new vasculature in the adult body arises mostly from angiogenesis. ECs, lining the inside of blood vessels, react to different angiogenic stimuli and inhibitors. Among the stimuli is the vascular endothelial growth factor (VEGF) which is up-regulated in tissue where the vascular structure is damaged or insufficiently developed to meet oxygen demand.

The identification of the processes involved in angiogenesis is quite recent and has stirred increased interest in therapeutic and clinical applications according to Carmeliet et al. [1]. One can think of tissue repair in wound beds, inhibition of growth of tumorous tissue or vascular reform during the female reproductive cycle. Rossiter et al. [2] showed that VEGF induced angiogenesis is crucial for wound healing in an experiment where wounds were inflicted upon normal and VEGF-deficient mice. New vasculature ensures supply of oxygen and lymphocytes and disposal of carbon dioxide and lactates, accelerating wound healing and tissue reconstruction. The increased creation of new vasculature around tumorous tissue is believed to follow the same process and inhibiting angiogenesis is therefore an important topic in clinical studies on cancer treatment.

Biochemical laboratory experiments can be hard, time consuming, expensive or unethical. Computational models can be used to provide an easy, quick and cheap way to get insights that would otherwise require laboratory experiments. The understanding of biological processes needs quantification and in this sense mathematical formulation of the relations involved becomes useful. Their mathematical interpretation and experimental verification is an iterative process resulting in better understanding of the process itself. Computer simulation will never make laboratory experiments obsolete, but it can provide guidance in targeting viable hypotheses before conducting *in vitro* or *in vivo* experiments.

Mathematical modeling of biological cellular processes dates back to the simulation by Glazier and Graner in 1992. They describe natural sorting behavior of different cell types [3] and different re-arrangement patterns driven by the differential adhesion hypothesis [4]. This hypothesis states that cells of different types have specific potential energies upon adhesion, driving sorting behavior. In these simulations, the cellular Potts model[2] (CPM) is used. A CPM for vasculogenesis based on this work was made by Merks et al. [5, 6] in which a layer of partial differential equations (PDEs) models the chemoattractants. Later, Merks added Vascular Endothelial cadherin (VE-cadherin) caused contact-inhibited chemotaxis to simulate angiogenic-like sprout formation [7]. From an initial clump of ECs in the model sprouting behavior appears. Merks postulates that both vasculogenesis and angiogenesis must be driven by the same principles. To produce these results, a generic library called the Tissue Simulation Toolkit (TST) was written in C++ starting from 2004 modeling the CPM described by Glazier et al. [4] in a generic way. Merks [7] extensively describes the advantages of a cell

---

[1] We present a useful glossary of biochemical terms for the mathematical reader in Appendix A.

[2] Also sometimes referred to as the large-Q Potts model or Glazier-Graner-Hogeweg model.

based approach over a continuum approach that is widely used in mathematical biology. Although his CPM is a nice method that increases insight in the angiogenic process, it is computationally heavy, limiting the scalability of the tractable problem domain.

Vermolen and Gefen [8] described tissue behavior using a semi-stochastic cell-based formalism to model the migration of cells in colonies in the context of wound healing, tumor growth, bone ingrowth and contraction formation. Movement of cells is assumed to be the result of a strain energy density working as a mechanical stimulus. Like the CPM, the model tracks displacement and viability of individual cells.

The aim of this study is to adapt this semi-stochastic cell-based formalism to describe angiogenesis, hence connecting this modeling approach to the subject of Merks' work. The need for such a model is clearly stated in the discussion of Vermolen's work [9]. Thanks to the computational less heavy character in comparison with the CPM, we hope to be able to simulate larger areas to get a better glance at large scale behavior whilst still being able to benefit from the cell-based character of the model. We also improve the biochemical model for the degrading of the substrate by the cells and formulate all relevant parameters based on local properties. The challenge is to translate the advantages of Merks' CPM, like cell shape specific behavior, tracking of elongation patterns and cell-cell contact behavior, to this new formalism without compromising the computational simplicity.

To verify our simulation results with biochemical experiments, this study is performed in collaboration with the Dermatology Department of the VU Medical Center. This department does *in vitro* laboratory research on many processes that occur in the skin, for example the role of endothelial cells during skin wound healing. The first aim of this research is to mimic their *in vitro* angiogenesis sprouting assay using our computational model, simulating the response to different chemical stimuli like VEGF. Formulating a way to visually and numerically compare the laboratory work to the simulated results is key to making the model applicable in practice.

In Chapter 2.1, we explain the biochemical background of angiogenesis, we describe the *in vitro* sprouting assay as performed by the VU Medical Center and we give an overview of the processes involved in cell migration. Chapter 3 is devoted to an overview of existing models for angiogenesis and cell colonies. In Chapter 4, a new model for angiogenesis is formulated, the results of which are discussed in Chapter 5. We formulate conclusions to this study in Chapter 6.

The appendices to this thesis are used to elaborate on subjects and mathematical formulations. In Appendix A we give an overview of all biochemical processes, physiological definitions and chemical substances useful as a reference tool for readers without a biochemical background. Appendix B describes a CPM implementation we developed during the literature study. In Appendix C, we formulate the complete derivation of the Galerkin equations to our system of PDEs and formulate the mass matrices of our Finite Element Method (FEM). Appendix D gives the details of the time stepping scheme used for the cell movement. Numerical considerations like dealing with spurious oscillations, meshing and the time stepping scheme for the chemicals are formulated in Appendix E. We conclude with an overview of the different options in our computational model and explain the different methods of visualization in Appendix F.

2

ANGIOGENESIS

2.1. IN VIVO ANGIOGENESIS

Sprouting angiogenesis is the formation of new blood vessels from existing ones, usually towards hypoxic tissue to meet oxygen demand. In sprouting angiogenesis new micro-vascular structures "sprout" from existing blood vessels. Angiogenesis is present in tissue remodeling after trauma and around tumorous tissue. The present vasculature in these settings is damaged or underdeveloped to meet the oxygen demand. The process can be roughly divided in five phases depicted in Figure 2.1. First, angiogenic growth factors, like VEGF, are secreted by oxygen deprived cells. ECs in existing vessels get activated to form new vasculature and a selected number of ECs differentiate to tip cells which lead the sprouts. The tip cells release proteases, among others matrix metalloproteinases (MMP) degrading the basement membrane (BM) underneath the endothelium. For a detailed description of the interactions between ECs and the different components of the BM we refer the reader to the work by Form et al. in [10]. The selection process of tip cells is mediated through a combination of stimulation by VEGF and inhibition by Delta-like ligand 4 (DLL4), a protease secreted by the tip cells themselves. The ECs than migrate into the surroundings, forming sprouts by degrading the extracellular matrix (ECM) by proteases like the urokinase-type plasminogen activator (uPA) . In the morphogenesis phase, by the lack of VEGF, the sprouting stabilizes and new boundary membrane is formed around the formed vasculature. Sprouting occurs at a rate of several millimeters per day.

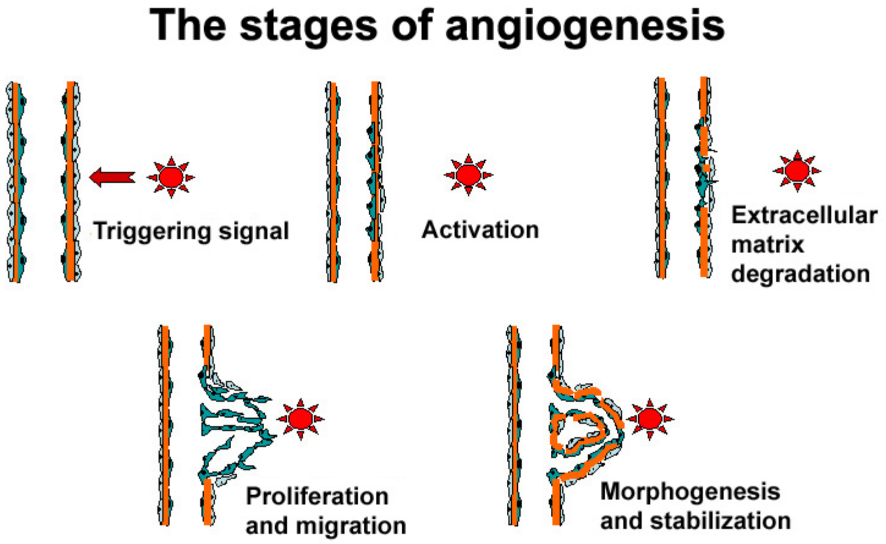

Figure 2.1: Phases of sprouting angiogenesis. (taken from Marti et al. [11])

In intussusceptive angiogenesis, also splitting angiogenesis, ECs in an existing vessel connect to form two lumen, splitting an existing vessel into two vessels. This type of angiogenesis is not considered in this study.

2.2. SETUP OF THE IN VITRO SPROUTING ASSAY

The dermatology department of the VU University Amsterdam Medical Center carries out several *in vitro* assays using either Adipose Tissue Endothelial Cells (ATECs) or Dermal Tissue Endothelial Cells (DTECs) on different substrates like fibrin. In this study, our particularly focus is on the sprouting assay on fibrin gel which is carried out in a standard 96 well plate depicted in Figure 2.2. In this assay, angiogenic responses to two different angiogenic growth factors VEGF and basic Fibroblast Growth Factor (bFGF) are measured for different concentrations.

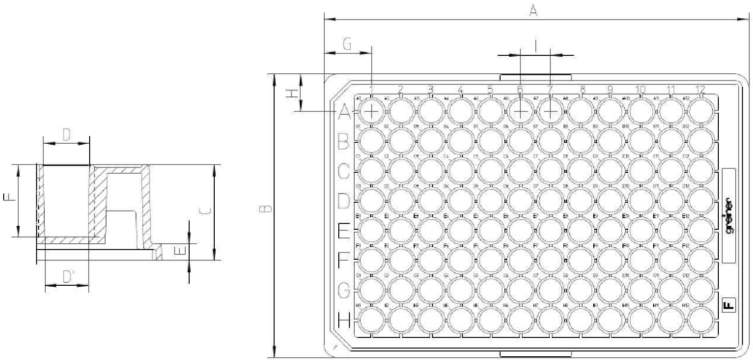

Figure 2.2: Standard 96 well plate. Wells are cylindrical with a diameter of 7 mm and a total volume of around 300 μL.

On the first day, a $v_F = 100\mu L$ fibrin gel ($3\frac{mg}{mL}$ fibrinogen with $0.5\frac{\mu g}{mL}$ thrombine IIa) is placed in a total of 39 wells on top of which a 100 μL solution is poured containing around $N = 20.000$ ECs. The total volume in the well then is $v = 200\mu L$. Experimental observations show that ECs have a typical diameter of around $45\mu m$, and hence a radius of $R = 22.5\mu m$. ECs are ellipsoidal being twice as long as wide. The ECs sink and adhere to the fibrin matrix, thus forming a confluent mono layer covering the surface of the fibrin almost completely as depicted in the microscopic images in Figure 2.3.

On the second day, different concentrations are added, with the exception of three control wells. The rest of the wells get a $2\frac{ng}{mL}$ Tumor Necrosis Factor alpha (TNF-α) solution, a cytokine that activates the ECs. Furthermore, concentrations of $25, 10, 3.3, 1.1, 0.3$ and $0.1\frac{ng}{mL}$ of either VEGF or bFGF are added. Since the recombinant bFGF used is a stronger angiogenic growth factor than VEGF for this assay, the $25\frac{ng}{mL}$ bFGF concentration is omitted since the entire matrix would degrade so fast that individual sprouts can no longer be observed. All different concentrations are replicated in threefold to compare the results and the well numbers are used to label the microscopic images. We summarize the different concentrations in Table 2.1.

	2	3	4	5	6	7	8	9
B	Control	T	VT 0.1	VT 0.3	VT 1.1	VT 3.3	VT 10	VT 25
C	Control	T	VT 0.1	VT 0.3	VT 1.1	VT 3.3	VT 10	VT 25
D	Control	T	VT 0.1	VT 0.3	VT 1.1	VT 3.3	VT 10	VT 25
E			BT 0.1	BT 0.3	BT 1.1	BT 3.3	BT 10	
F			BT 0.1	BT 0.3	BT 1.1	BT 3.3	BT 10	
G			BT 0.1	BT 0.3	BT 1.1	BT 3.3	BT 10	

Table 2.1: Control wells have nothing added to them. All wells with a “T” have a $2\frac{ng}{mL}$ TNF-α solution added. Wells with a “V” have VEGF added to them in the given concentrations. Wells with a “B” have bFGF added to them in the given concentrations.

Depending on the donor specific cell motility[1], the substrates are fixated 48 to 72 hours after stimulation. The sprouting into the fibrin gel is observed using microscopic images like those in Figure 2.4. The images have names coinciding with the well number. In this Figure, we see well “9d”. The monolayer is roughly undamaged, except for a couple of circular-like structures with dark edges. These dark edges form the premises of the newly formed sprouts and are most likely the effect the fibrous layer underneath the monolayer bending out of the focal reach of the microscope.

---

[1] We will call the specific motility β_i in subsequent chapters.

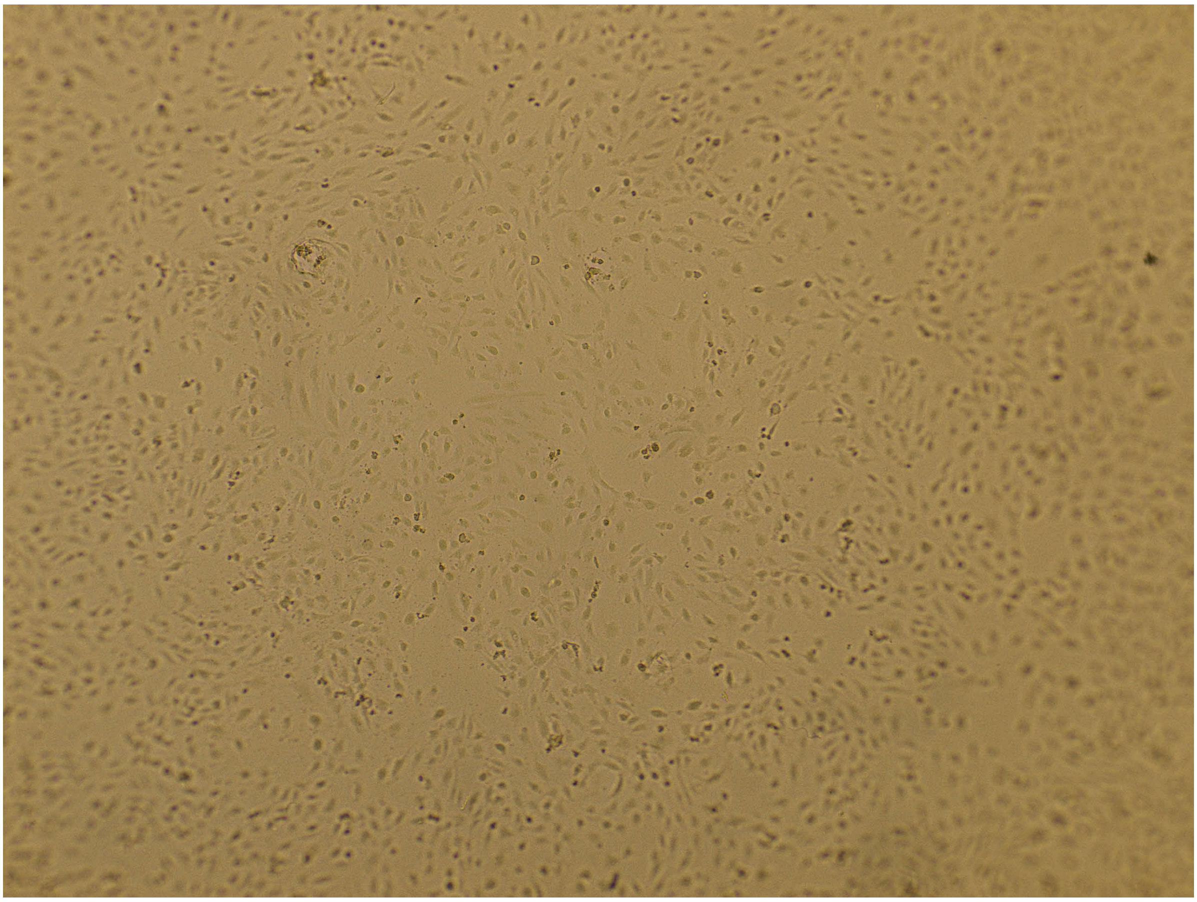

Figure 2.3: Dermal ECs in control well “2d”. No sprouting can be seen.

In Figure 2.5, we zoom in on one of the sprouts. Inside the sprout, the fibrin matrix is degraded and this shows up slightly lighter on the microscopic image. We can see that no ECs show up in the image inside the sprout. This is due to the fact that the sprouts move into the matrix and get out of focus in the microscopic image. The amount of sprouting in an assay is quantified using image processing software. The darker edges of the sprouts are colored and the cumulative area of the colored regions is calculated as a percentage of the total area of the image. When arriving at our results in Chapter 5, we will calculate this percentage over time and call it $P(t)$.

Although it can not be seen in these microscopic pictures, we know that sprouts are, as a rule of thumb, twice as deep as their diameter at the top of the fibrin matrix. One can conclude this by varying the focal depth of the microscope. Sprouts usually are in downwards direction, but slightly bending sprouts are also observed.

2.3. DRIVING FORCES ON CELLS IN SPROUTING ANGIOGENESIS

The motility of cells on the fibrin scaffold is subject to many mechanical and chemical factors. We identify several factors driving the movement of cells on the fibrin matrix. The mathematical formulation of these principles is covered in Chapter 4. For detailed cell biological descriptions of the hereafter listed phenomena, we refer the reader to the extensive work on cell movements by Bray [12].

2.3.1. CHEMOTAXIS

Gamba [13] and Serini [14] describe chemotaxis as the movement of cells in response to a chemical stimulus. One speaks of positive (negative) chemotaxis if the movement is in the (opposite) direction of the gradient and the chemical is called a chemoattractant (chemorepellent). Chemoattractants can be, following the Keller-Segel model formulated by Horstman [15], secreted by the cells themselves, leading to the formation of isolated clusters of cells. The chemotactic process takes place thanks to pseudopodia on the cell membranes

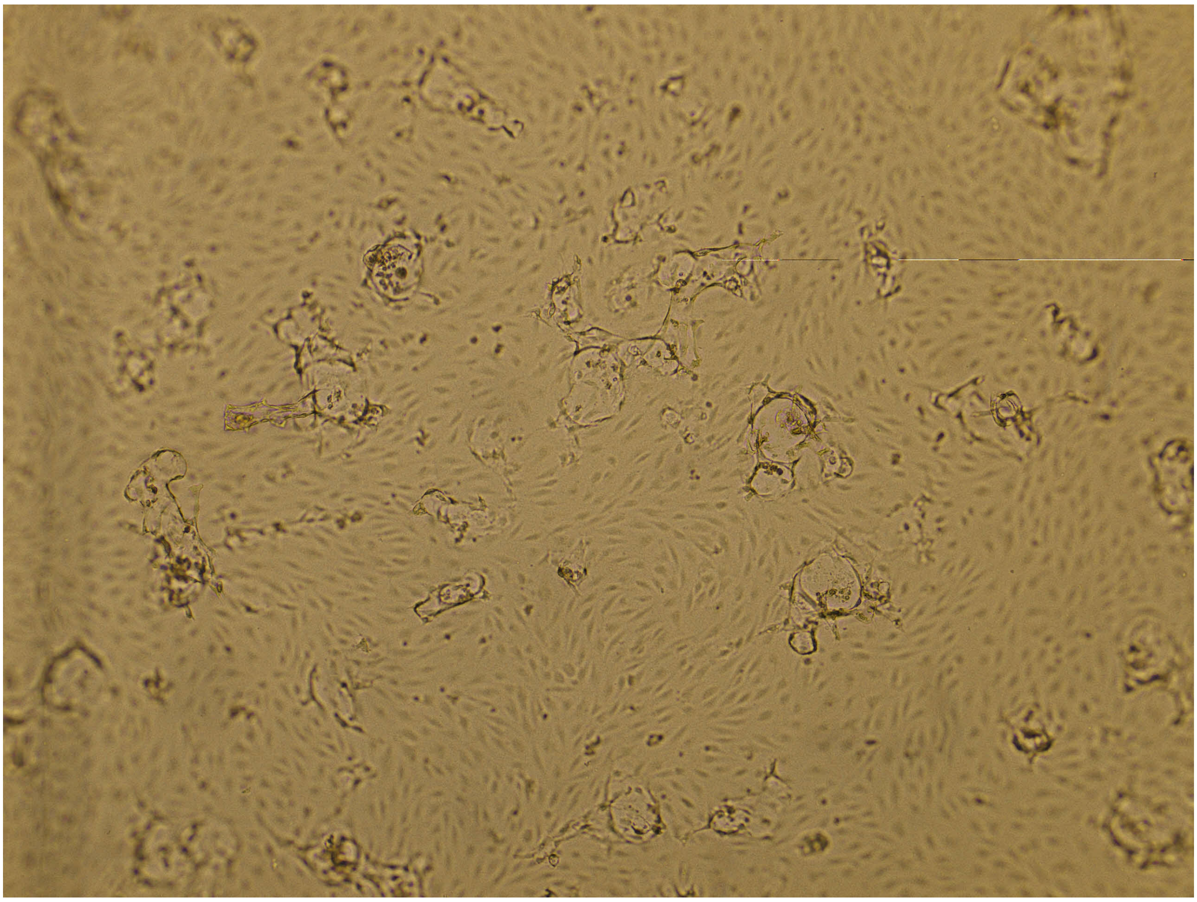

Figure 2.4: Dermal ECs in well “9d” after stimulation with $25 ng/ml$ VEGF and 2 ng/ml TNF-α. The circular structures form the boundaries of newly formed sprouts.

that are formed on the sides of the cell in high concentrations of the chemoattractant and “reach” towards higher concentrations, pulling the cell in the desired direction. Inflammatory mediators such as TNF-α may increase the motility of cells.

2.3.2. CELL-CELL FORCES

Cells can adhere to each other by physically attaching their cell membranes using surface proteins like cadherins. ECs adhere to each other using Vascular Endothelial cadherin (VE-cadherin) bonds. VE-cadherin at the same time works as in inhibitor of chemotactic movement caused by VEGF by binding to the same receptor used in the chemotaxis signaling pathway. Merks describes this contact inhibition in his CPM in [16].

ECs have a certain optimal elliptical shape induced by their cytoskeleton and will try to elastically return to this shape upon deformation. The magnitude of these forces is proportional to the elasticity of the cell and the severity of the deformation. We will denote this effect by contact mechanics in further chapters.

2.3.3. CELL-MATRIX FORCES

Trans-membrane integrin proteins on the cell membrane adhere to fibrous scaffolds such as fibrin or collagen and exert contractile forces causing cell-matrix adhesion. Since these forces are caused by physical attachment to the fibrin scaffold, the net force will be in the direction of the fibrin gradient. However, high density fibrin scaffolds may be too stiff to move into.

The same cell-matrix adhesive forces cause strain in the elastic fibrin scaffold which on its turn is sensed by other cells adhering to the matrix and they get pulled along the stress lines. This effect is called haptotaxis or mechanotaxis and as of 1995, mathematical models have been proposes by Vernon [17], Namy [18] and Manoussaki [19, 20].

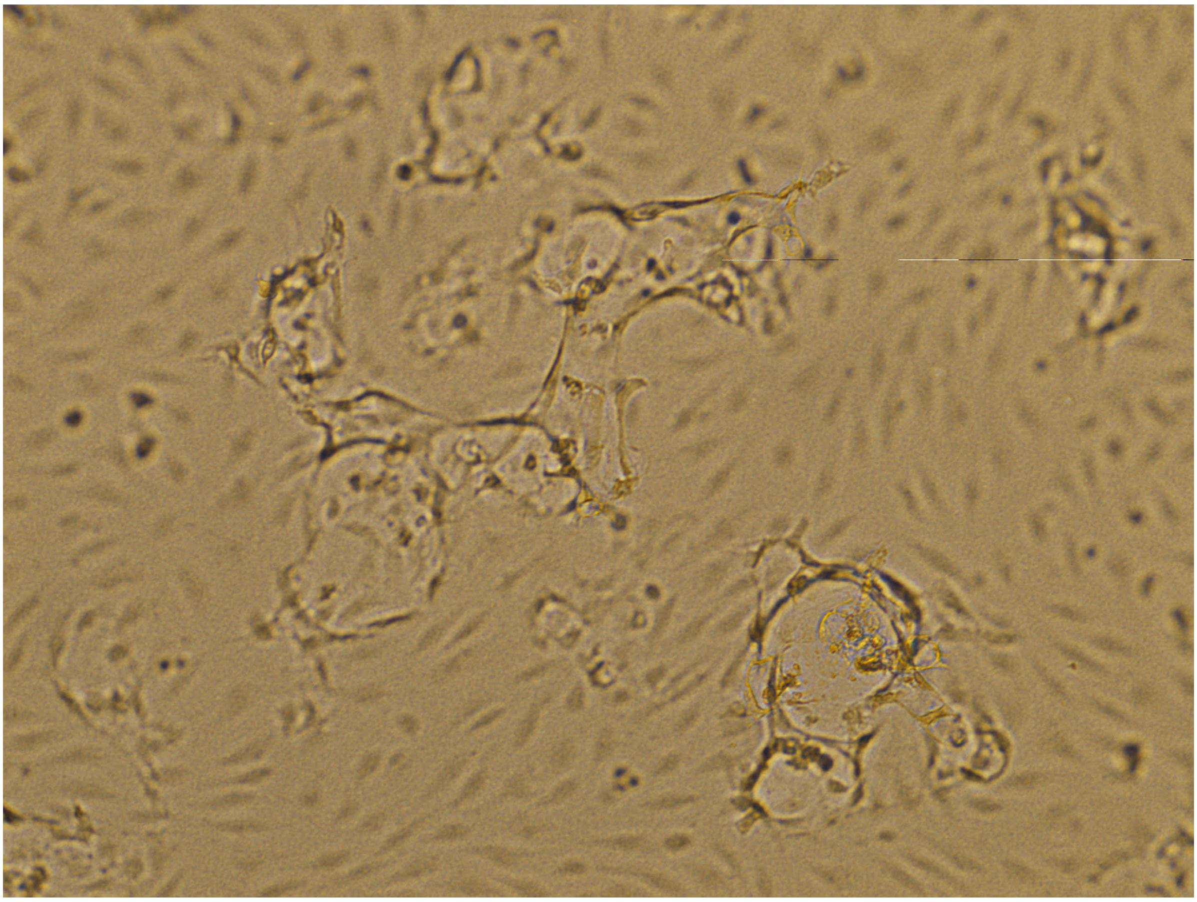

Figure 2.5: Dermal ECs in well “9d” after stimulation with 25ng/ml VEGF and 2 ng/ml TNF-α. The circular structures form the boundaries of newly formed sprouts.

Reinhart-King et al. [21] conducted a series of experiments considering the interplay between cell-cell adhesion and haptotactic forces for endothelial cells. They conclude that matrix stiffness is an important factor for the cell motility and the ability to mechanically communicate through the substrate.

2.3.4. GRAVITY

Cells do usually have a higher density than the fluid they are initially dissolved in according to Urbanchek et al. [22]. This lets gravity act a downwards directed force upon the cells causing them to “sink” onto the fibrin scaffold. We must note that gravity in the field of cellular biology is not dominant over the adhesive forces. A sprouting assay where a clump of ECs is embedded inside a fibrin scaffold will show sprouting behavior in all directions. However, in the sprouting assay setup used at the VU medical center, gravity together with contact mechanics form a reasonable explanation for the formation of the initial confluent mono-layer.

3

EXISTING MODELS FOR ANGIOGENESIS

In this chapter, we explore the different methods of modeling angiogenesis mathematically. We distinguish between CPMs, continuum models and sem-stochastic cell-based models and compare them. It is important to note that all models use PDEs to model the diffusion, reaction and production of chemoattractants and other substances. We therefore choose not to go into detail considering these PDE layers.

The distinction lies in the way the models describe cell motility and behavior. The CPM models individual cells as collections of lattice sites that can behave separately, the semi-stochastic cell-based model proposes that individual cells are spherical and continuum models describes cell as densities over a domain and therefore do not track movement of individual cells.

3.1. THE CELLULAR POTTS MODEL

The CPM for simulation of biological cells was first used by Glazier and Graner in 1992 [3] in a 2 dimensional setting. It is a lattice-based computational model derived from cellular-automaton models having stochastic evolvement. These models were firstly developed for various branches in theoretical and computational physics. The computational domain consists of a square lattice of $n_x \times m_y$ sites, denoting the lattice sites by (n,m) for $n = 1,\dots,n_x$ and $m = 1,\dots,m_y$. The model assigns a cell ID $\sigma = 1,\dots,i,\dots,j,\dots,N$ (formerly “spin”) to each lattice site $\vec{x} = (n,m)$. Lattice sites having the same ID together form one biological cell, hence creating a total of n cells. The model evolves by updating the lattice-sites one at a time according to probabilistic rules and a Hamiltonian function $\mathcal{H}(n,m,\sigma)$, assigning an effective energy to each lattice-site (n,m) for every cell ID σ.

At each time step, a lattice site (n,m) is picked randomly and its cell ID i is changed to j whenever the effective energy gain $\Delta\mathcal{H} = \mathcal{H}(n,m,j) - \mathcal{H}(n,m,i)$ is negative (i.e. more energy efficient) and it is changed with a probability whenever the gain is positive, i.e.

$$\mathbb{P}(\Delta\mathcal{H}) = \begin{cases} 1 & \text{if} \Delta\mathcal{H} < 0, \\ e^{\frac{-\Delta\mathcal{H}}{kT}} & \text{if} \Delta\mathcal{H} \geq 0. \end{cases} \tag{3.1}$$

Here, T is the temperature and k is a parameter governing the likelihood of energy inefficient changes. Cell ID changes are only allowed to cell IDs of the adjacent lattice sites.

The Hamiltonian plays a central role in the proliferation of the cells. Glazier and Graner [3] implemented a Hamiltonian incorporating cell-cell adhesion, elasticity based on an area and length constraint and chemotaxis. Connections between neighboring lattice sites $\vec{x}$ and $\vec{x}'$ of unlike spin $\sigma(\vec{x}) \neq \sigma(\vec{x}')$ represent membrane bonds, where the bond energy is $J_{\vec{x},\vec{x}'}$. Cells are given a target area $A_{target}(\sigma)$ and length $L_{target}(\sigma)$ and are given penalties for large deviations. A concentration $c(\vec{x})$ of chemoattractant is modeled over the problem domain. Chemotaxis is added using the difference in concentration between neighboring lattice sites. Altogether Merks derives the following Hamiltonian in [5–7]:

$$\begin{aligned}\mathcal{H} =& \mathcal{H}_{contact} + \mathcal{H}_{shape} + \mathcal{H}_{chemotaxis}\\ =& \sum_{\vec{x},\vec{x}'} J_{\sigma(\vec{x}),\sigma(\vec{x}')}\left(1-\delta_{\sigma(\vec{x}),\sigma(\vec{x}')}\right)\\ &+\sum_{\sigma}\lambda_{area}(\sigma)[A(\sigma)-A_{target}(\sigma)]^2+\lambda_{length}(\sigma)[L(\sigma)-L_{target}(\sigma)]^2\\ &+\ \lambda_{chemotaxis}[c(\vec{x}')-c(\vec{x})].\end{aligned}$$

The λ's are scaling parameters to give weights to the different effects and Merks finds values based on simulation observation. The chemicals in their model follows a diffusion, reaction, sourcing PDE given by

$$\frac{\partial c}{\partial t} = \alpha\delta_{\sigma(\vec{x}),0} - (1-\delta_{\sigma(\vec{x}),0})\epsilon c + \nabla^2 c,$$

assuming that there is no decay within a cell. Here, $\delta_{\sigma(\vec{x}),0}$ is 1 inside cells and 0 outside and α and ϵ are sourcing and reaction constants. The PDE is solved by a finite difference scheme on a lattice coinciding with the CPM lattice.

Although not necessarily shaped like this, CPMs mostly have a fixed square lattice. This can lead to coarse cell shapes, especially for cells containing few lattice sites. The recursive lattice updates can be computationally heavy. In older applications, the sequential modified Metropolis algorithm described by Chen [23] is used. In 2007 Chen et al. introduced a parallel algorithm using checkerboard subgrids to speed up computations. This allows for simulations with up to 10^7 lattice sites on cluster computers.

Merks claims that the CPM is more useful in describing cell phenomenology like shape, elongation and cell-cell contact interaction in comparison with continuum models. Furthermore he claims the model to be advantageous in describing how collections of cells, exhibiting a certain phenomenology, interact during biological morphogenesis [5]. The TST was used to study the effects of cell elongation on vasculogenesis [6] and Merks conclude that cell shape and cell-cell contact interaction are of crucial importance in the process of angiogenesis.

3.2. CONTINUUM MODELS

There is a large number of continuum models consisting of systems of PDE's. Alarcon and Chaplain [24] give an excellent overview of continuum models up to the year 2005 for tumor induced angiogenesis as well as a list of advantages and disadvantages of these models. Many early models, like those proposed by Gaffney [25] or Anderson [26] are based on phenomenological arguments or design principles to describe the angiogenic process. Anderson [26] came up with a continuum-discrete model including fibronectin induced haptotaxis as a governing factor. As the research into different angiogenic growth factors progressed, models following a more biochemical reasoning appeared like those by Orme [27], Levine [28] and Vermolen [29]. Schugart et al. [30] and Xue et al. [31] both propose elaborate models incorporating multiple cell types (ECs, fibroblasts, tip ECs and inflammatory cells) and different substances (oxygen, VEGF and ECM) in one coupled continuum system to describe oxidative stress and angiogenesis in wound healing. An elaborate continuum model on wound closure incorporating contraction and angiogenesis is proposed by Vermolen and Javierre [32]. We believe that these models provide the most recent developments in continuum modeling of angiogenesis.

In both types of models, cells are modeled as densities or concentrations over the computational domain. To illustrate this, we briefly consider the model by Gaffney [25] who models concentrations of tip cells n and stalk cells b incorporating behavior like capillary sprouting, branching, tips joining each other (anastomosis) and tips joining other sprouts. The coupled system derived from a conservation relation is given by

$$\begin{aligned}\frac{\partial n}{\partial t} &= - \frac{\partial J(n)}{dx} + f(n,b),\\ \frac{\partial b}{\partial t} &= -\lambda_5 \frac{\partial J(n)}{dx} + g(n,b).\end{aligned}$$

In this coupled system they set the tip cells' flux to

$$J(n) = -D_1\frac{\partial n}{\partial x} - D_2 n\frac{\partial b}{\partial x},$$

the tip cells' kinetics to

$$f(n,b) = \lambda_2 n - \lambda_3 n^2 - \lambda_4 nb,$$

and the EC's kinetics to

$$g(n,b) = \lambda_2 \nu b(b_0 - b) + \lambda_6 \chi nb(b_1 - b) + \lambda_5(\lambda_3 n^2 + \lambda_4 nb).$$

The model replaces both the haptotactic and the chemotactic movement we saw in previous models by a movement in the direction of decreasing blood vessel density. The parameter λ_2 governs tip branching, λ_3 governs the joining of tips to create a circuit and λ_4 governs tips joining the side of a capillary. The parameter λ_5 ensures the proportionality between the flux of the tips and the flux of the ECs and is given by the average number of ECs in a capillary sprout. Gaffney uses dimensionless scaling and stationary point analysis to find the dynamics of the system. The parameters are estimated using experimental results. Finally, boundary conditions and initial conditions are formulated and an analytical solution is found using perturbation theory.

Maggelakis [33] proposed a widely used continuum model for angiogenesis in a circular wound bed of radius R, in which capillary tips modeled by a density n act as the main source of the oxygen concentration c_O. Oxygen diffuses with a rate D_O, sources from the capillaries at a rate λ_n and is consumed by macrophages at a rate λ_O from some critical oxygen level c_θ at which macrophages become active at the wound site. The macrophages release chemoattractants called Macrophage Derived Growth Factors (MDGFs) denoted by concentration c_m. The MDGFs diffuse at a rate D_m, are produced at a rate λ_m, react within the capillary tips at a rate λ_c and degrade naturally at a rate λ. High concentrations of MDGFs trigger capillary logistic growth up to a certain maximal vascular density L. The system of PDEs describing this process is given by

$$\begin{aligned}
\frac{\partial c_O}{\partial t} &= D_O \nabla^2 c_O + \lambda_n n - \lambda_O \frac{c_O}{c_\theta}, \\
\frac{\partial c_m}{\partial t} &= \begin{cases} D_m \nabla^2 c_m - \lambda c_m + \lambda_m \left(1 - \frac{c_O}{c_\theta}\right)_+, & \text{for } 0 \le r \le R, \\ D_m \nabla^2 c_m - \lambda c_m - \lambda_c \frac{c_m}{c_{\max}}, & \text{for } R < r \le R_{\max}. \end{cases} \\
\frac{\partial n}{\partial t} &= \mu c_m n \left[1 - \frac{n}{L}\right].
\end{aligned}$$

Note that the secretion of the MDGFs only takes place inside of the wound bed due to the presence of macrophages.

3.3. SEMI-STOCHASTIC CELL-BASED MODEL

Vermolen and Gefen [8] formulated a semi-stochastic cell-based formalism for migration of cells in colonies. In their work on a simulated substrate $\Omega \subset \mathbb{R}^2$, a set of N hemispherical cells is modeled. The choice for (hemi)spherical cells is to speed up the analysis since cells do not have an orientation. For an overview of possibilities to include cell shape changes induced by chemotaxis or mechanical influences, we refer the reader to Vermolen and Gefen [34]. They model four different types of cell motility: haptotaxis, proliferation, random movement and elastic contact movement. Chemotaxis is not yet implemented in this model in published work. We consider these effects separately.

3.3.1. HAPTOTAXIS

The haptotactic response of cells to strain in the matrix is caused by the effect of traction forces of the cells themselves. We first encounter this concept in a continuum model by Manoussaki in 1996 [19] and 2003 in [20]. By this traction force, the substrate is distorted around the cell. This distortion is felt by other cells, which distort the substrate as well by applying their own upward pulling forces. If we denote the elasticity modulus or Young's modulus of the substrate by E_s and the strain by ϵ, we have the strain energy $M = \frac{1}{2} E_s \epsilon^2$, i.e. the energy stored in a medium undergoing the deformation caused by the strain. Individual cells sense the distortion field through the strain energy density and then move along the stress lines. Vermolen and Gefen in [8] state that the strain energy density caused by an individual cell i, following Hooke's law, is maximal at the cell center $\mathbf{r}_i$, as if the cell acts a point force upon the matrix in its center, i.e.

$$M_i^0 = \frac{F_i^2}{2\pi^2 E_s(\mathbf{r}_i)R^4}, \tag{3.2}$$

where F_i is the maximal traction force of cell i, $E_s(\mathbf{r}_i)$ is the local elasticity modulus of the substrate and R is the cell radius. Furthermore they approximate, according to the findings by Merkel in [35], that the strain energy density decays exponentially with the radius with a rate proportional to λ_i, the ratio of the elasticity modulus of the substrate and the elasticity modulus E_c of the cell itself, i.e.

$$M_i(\mathbf{r}) = M_i^0 \exp\left(-\lambda_i \frac{\|\mathbf{r}-\mathbf{r}_i\|}{R}\right) = M_i^0 \exp\left(-\frac{E_s(\mathbf{r}_i)}{E_c}\frac{\|\mathbf{r}-\mathbf{r}_i\|}{R}\right). \tag{3.3}$$

They then argue that the total strain energy density is the sum of the strain energies of the individual cells and determine the total strain energy density at a cell center $\mathbf{r}_i$ to be

$$M(\mathbf{r}_i) = M_i^0 + \sum_{j=1_{j\neq i}}^{N} M_j^0 \exp\left(-\frac{E_s(\mathbf{r}_j)}{E_c}\frac{\|\mathbf{r}_i-\mathbf{r}_j\|}{R}\right).$$

Now consider the displacement of a cell by means of the sensed mechanical stimulus. The displacement of cell i caused by cell j is proportional to the strain energy density caused by cell j at cell center $\mathbf{r}_i$, i.e. $M_j(\mathbf{r}_i)$ and in the direction of the line segment connecting cells i to j, i.e. $\mathbf{v}_{ij} = \frac{\mathbf{r}_i-\mathbf{r}_j}{\|\mathbf{r}_i-\mathbf{r}_j\|}$. Vermolen and Gefen [8] argue that the total displacement of cell i is parallel to the sum of the directional displacements z_i caused by all other cells, i.e.

$$\mathbf{z}_i = \sum_{j=1_{j\neq i}}^{N} M_j(\mathbf{r}_i)\mathbf{v}_{ij} = \sum_{j=1_{j\neq i}}^{N} M_j^0 \exp\left(-\frac{E_s(\mathbf{r}_j)}{E_c}\frac{\|\mathbf{r}_i-\mathbf{r}_j\|}{R}\right)\frac{\mathbf{r}_i-\mathbf{r}_j}{\|\mathbf{r}_i-\mathbf{r}_j\|}.$$

One can normalize the direction of the total displacement $\hat{\mathbf{z}}_i = \frac{\mathbf{z}_i}{\|\mathbf{z}_i\|}$. The displacement over time is proportional to the strength of the mechanical signal leading to

$$\begin{aligned}\frac{\mathbf{r}_i(t+\Delta t)-\mathbf{r}_i(t)}{\Delta t} &= \alpha_i M(\mathbf{r}_i(t))\hat{\mathbf{z}}_i,\\ \mathbf{r}_i(t+\Delta t) &= \mathbf{r}_i(t)+\Delta t\alpha_i M(\mathbf{r}_i(t))\hat{\mathbf{z}}_i,\end{aligned}$$

where α_i is a parameter with dimension $\left[\frac{m^3}{Ns}\right]$ in which the force is directed along the substrate, perpendicular to the upward force F_i. Finally, Gefen [36] argues that this quantity for viable cells equals

$$\alpha_i = \frac{\beta_i R^3}{\mu F_i},$$

where β_i quantifies the motility of the cell surface of a cell and μ it the cell friction coefficient quantifying the amount of friction that the cell experiences from the matrix. The latter variable is a dimensionless quantity experimentally tested to be 0.2 according to Gefen [36]. Especially for cells far away from each other, the strain energy $M_j(\mathbf{r}_i)$ can attain very small values, nullifying the contribution to $\mathbf{z}_i$. This advocates a detection threshold for the strain energy density as a minimal signal strength that a cell can detect to reduce computational complexity. For details we refer to Vermolen's work [8] and the work by Reinhardt-King et al. [37].

In an additional paper, Vermolen and Gefen [38] add inertia to the movement of the cells and a slowing parameter depending on the lactate concentration in infected wound tissue. The concentration of the lactate is modeled by a PDE where bacteria are added as point sources of lactate.

3.3.2. PROLIFERATION

Vermolen and Gefen introduce cell death and proliferation into the model using a stochastic process. At each time step, each cell has a probability of dying, making the cell stationary and not contributing to the strain energy. Proliferation is modeled by adding a daughter cell and giving both cells a displacement as the mother cell would have gotten with an extra tangent displacement ±R. Improvements upon this process can be made and suggestions are made by Vermolen and van der Meijden [39] in unpublished work.

3.3.3. RANDOM MOVEMENT

Vermolen and Gefen add random movement to the cells using a term $\Delta t(1-u_i)\mathbf{w}$ where

$$u_i = u_i(y_i) = \begin{cases} 1, \text{if } y_i \leq p_{mp} \\ 0, \text{if } y_i > p_{mp} \end{cases}$$

for $Y_i \sim U(0,1)$, p_{mp} is a parameter and $\mathbf{w}$ is a unit vector with stochastic angle. Alternatively, Dudaie et al. [40] propose to model the random movement using a Wiener process. We will follow this approach later on in deriving our new model.

3.3.4. ELASTIC CONTACT MOVEMENT

Cells impinging on each other will exercise repulsive forces. The direction of the force is along the line segment connecting the cell centers and the magnitude is, according to elastic contact mechanics described by Gefen in [36], depending on the depth h both cells have to dent due to the collision. Using arguments from contact mechanics from Johnson [41], Gefen describes the strain energy M^{ij} due to a collision between cells i and j to be

$$M^{ij} = \frac{4}{15\sqrt{2}} \frac{E_c}{\pi} \left(\frac{h}{R}\right)^{5/2}. \tag{3.4}$$

Since the contact forces are always in the opposite direction of the haptotactic forces, Vermolen [8] subtracts this strain energy from the strain energy density caused by the haptotactic cell forces in Equation 3.3, i.e. $\tilde{M}_i(\mathbf{r}_j) = M_i(\mathbf{r}_j) - M^{ij}$ and use $\tilde{M}_i(\mathbf{r}_j)$ in Equation 3.3.

3.4. COMPARISON OF THE MODEL TYPES

It can be expected that all three types of models have their advantages and disadvantages. We discuss their merits and demerits here briefly.

In the CPM, it is easy to track specific cell motility and implement cell shape and size specific behavior as well as cell contact interface specific properties such as contact inhibited chemotaxis. However, the model is computationally heavy and relies on many model choices such as the weight factors for the different terms in the Hamiltonian function. These factors do not have a physical background and they are “fitted” to reach the desired model outcome. Hence, the model has a phenomenological nature and one can question the adaptability to changing conditions, different topologies and real life applications.

Possibly the main criticism of continuum models for angiogenesis stems from their inability to track individual capillary tips and to accurately reproduce the patterns of vascular growth. Cell-cell and cell-matrix interaction is more complex to incorporate. They are however computationally scalable to a very large extent, making them useful for simulating of tissue on a large scale. Continuum models exist that are of a more physical and phenomenological nature.

The semi-stochastic cell-based model is computationally less heavy but can still follow cells on an individual level and we hypothesize that the model is able to track capillary formation in the angiogenic process. It benefits from cell-cell and cell-matrix interaction like contact mechanics, haptotaxis and adhesion. The model is however not able to incorporate very complex cell shape dependent mechanics like contact inhibition because of the simplified spherical shape of individual cells. It is a challenge for this study to overcome this limitation to such an extent that we reach reliable model outcomes. Finally, all parameters have a physical origin and the model is therefore adaptable to changing conditions and domains.

We conclude that the CPM is especially useful to model specific cell behavior on a small scale. The semi-stochastic cell-based model works on a mid-large scale and the continuum models gives the desired results on a large scale where both the CPM and the semi-stochastic cell-based models grow intractable.

4

A NEW 3-D SUBSTRATE DEPENDENT CELL-BASED MODEL (SDCBM)

In order to mimic the sprouting assay performed by the VU medical center dermatology department, we propose a new computational Substrate Dependent Cell-Based Model (SDCBM). Similar to existing models, the SDCBM also consist of two layers: a PDE layer governing the chemicals and a mechano-biological layer governing the cell movement. In this chapter we formulate both. We first propose a relational model that reflects how the different substrate components, chemicals and cells influence each other. We then come up with a system of differential equations governing the concentrations of the different chemicals and substrate components over time and we formulate the initial and the boundary conditions. We use a finite element discretization which we derive in Appendix C to approximate the solution. We choose to do so in a three dimensional setting to closely mimic the lab work carried out by the dermatology department of the VU Medical Center. Secondly, we give an overview of the mechanical and chemical effects on cells and we formulate the cell movement based on the semi-stochastic cell-based formalism as proposed by Vermolen and Gefen in [8]. We conclude by stating our choice of parameters, domain and initial cell distribution.

Two model design principles are central to our approach. First of all, we will model the substrate composition and degrading continuously. This is contrary to the discrete formulation in the CPM by Merks where lattice sites are either substrate or Extra-Cellular Fluid (ECF) . Parameters like viscosity, density, elasticity, friction and diffusion rates become continuous functions of the substrate composition over the domain. This improvement mimics the real experiments more closely and avoids unexpected discontinuous behavior of the model. Secondly, we try to use physical parameters with values that are as realistic as possible and try to refrain from using “fitting parameters” such as scale factors. This will give us a better understanding of the physical and physiological background of the angiogenesis process which makes the model adaptable to a wider range of problems and increases the predictive value of the simulation outcome.

4.1. FEEDBACK PROCESSES IN THE SDCBM

We start with a qualitative description of the components of our SDCBM. We distinguish between cells, substrate components and chemicals. ECs in our model can be of two phenotypes: tip cells and stalk cells. We model four different chemicals: Vascular endothelial growth factor (VEGF), Matrix Metalloproteinases (MMP), Urokinase-type type Plasminogen Activator (uPA) and Delta-like ligand 4 (DLL4), the biochemical functions of which are described in Section 2.1. The substrate consists of fibrin, BM and ECF.

Tip cells secrete DLL4, uPA and MMP. uPA and MMP degrade fibrin and BM into ECF and are consumed in the process. Degraded substrate has a higher permeability and cell movement increases. Tip cells move towards higher concentrations of VEGF and consume it. Stalk cells move towards higher concentrations of DLL4 and consume it. VEGF up-regulates tip cell selection whilst DLL4 inhibits it. All these factors form a feedback loop given in Figure 4.1.

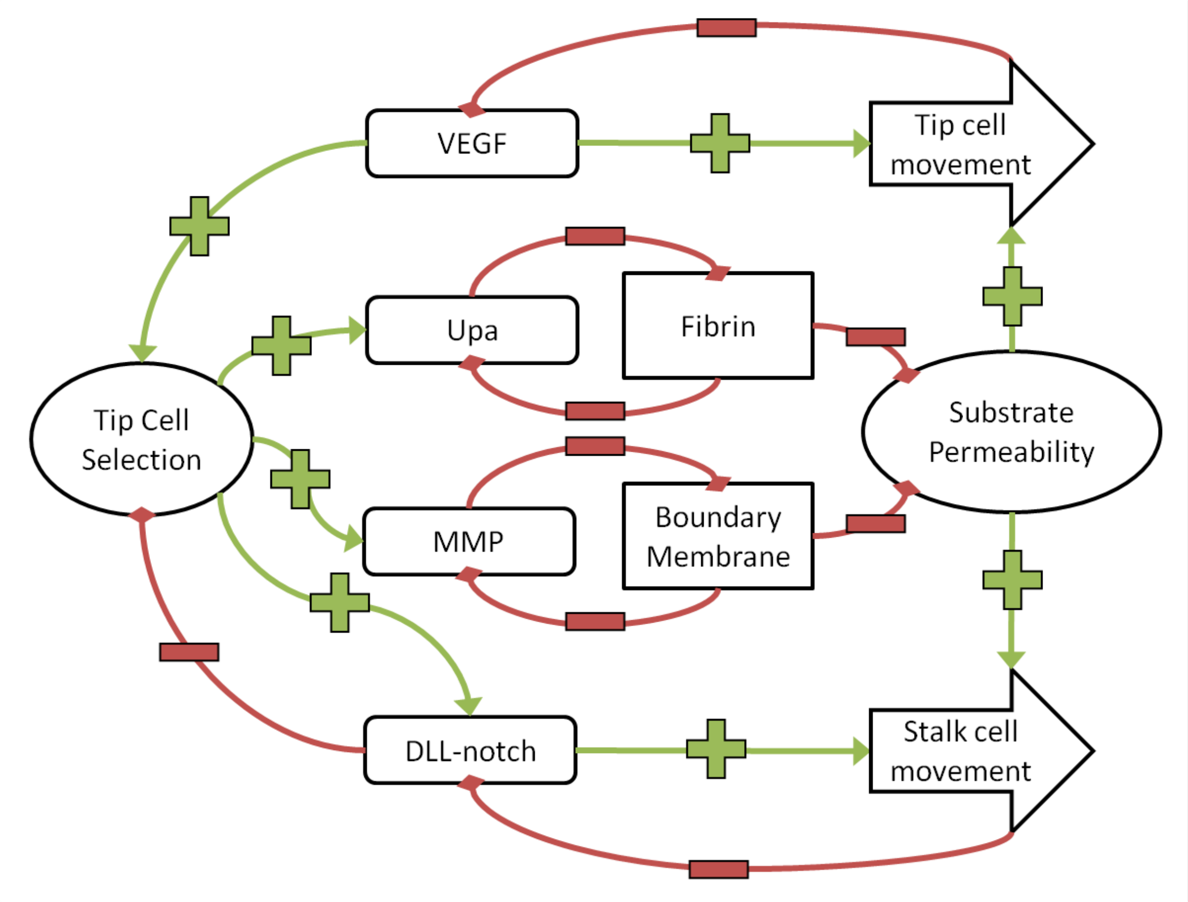

Figure 4.1: Schematic feedback loop of all processes in the model. Green arrows (with plus signs) constitute positive feedback. Red arrows (with minus signs) constitute negative feedback. Square boxes represent substrate components. Rounded boxes represent chemicals. Block arrows represent cell movement.

4.2. SYSTEM OF PDE'S GOVERNING THE CHEMICALS AND SUBSTRATE COMPONENTS

Comparable to almost every model for biochemical processes, we model the dynamics of a chemical c based on Reaction-Diffusion-Sourcing equations of the form

$$\frac{\partial c}{\partial t} = \nabla \cdot [D(\mathbf{x})\nabla c] - rc + S(\mathbf{x}),$$

where $D(\mathbf{x})$ is a (possibly location dependent) diffusion constant, r is a reactive constant and $S(\mathbf{x})$ is a source term. We will explain our adaptations to this standard formulation here.

As proposed, we model the substrate as fractions BM f_B and fibrin f_F. We consider the case where both substrate components can be degraded into Extracellular Fluid (ECF) denoted by f_E continuously. This entails describing PDEs not only for the chemoattractants, but also for the fractions f_F, f_B and f_E. Following conservation of mass, the substrate fractions must add up to 1 (100%), i.e. the amount of fibrin and BM degrading in the reactive term must be equal to the gain in mass for the ECM in the source term. There is no sourcing of fibrin and BM and we model that there is no diffusion of the substrate.

We introduce diffusive terms for the four chemicals dependent on the composition of the substrate. For instance, for the diffusive factor of the concentration VEGF c_V we write $D_V = D_V(f_F, f_B, f_E)$, making the diffusion process substrate dependent[1]. We will come back to the precise formulation of the diffusive function

---

[1] In our computational model, the option `g.chem0.nonLinearDiffusion` is used to use these non-linear diffusion functions.

after formulating the PDEs.

The rate at which the BM degrades under influence of MMP is in the continuous substrate setting proportional to both the fraction of BM and the concentration of MMP c_M. If there is no MMP, the BM will not degrade and conversely if there is no BM, there is nothing for the present MMP to degrade. This leads to a multiplicative cross term in the reactive parts of the equations for the concentration MMP and the fraction BM. The same holds for the fibrin fraction f_F and the uPA concentration c_U. Furthermore we call the concentration VEGF c_V and the concentration DLL4 c_D.

Finally, we model the reaction and sourcing to take place at the cell centers. VEGF is consumed within all cell types and DLL4 is consumed only within stalk cells. DLL4, MMP and uPA is sourced from tip cells. We model that the rate of sourcing is proportional to the concentration VEGF. This entails that cells feeling in higher stimulated with higher concentrations VEGF will degrade the substrate faster and will give a stronger chemotactic response to surrounding stalk cells.

We number our cells $q = 1,\dots,N$. Furthermore θ is the index set of all cells and $\theta_t \subset \theta$ is the index set of all tip cells and $\theta_s \subset \theta$ is the index set of all stalk cells such that $\theta_t \cap \theta_s = \emptyset$ and $\theta_t \cup \theta_s = \theta$. The Cartesian coordinates of the cell center of cell q are denoted by $\mathbf{x}_q$. We now use Dirac delta distributions $\delta(\mathbf{x}-\mathbf{x}_q)$ to locate the reaction and sourcing within cell q and sum over the reactive an sourcing terms over the appropriate set of cells.

Altogether, this leads to the following coupled, non-linear system of 7 PDEs.

Chemicals

$$\begin{array}{lllll}
\text{VEGF} & \dfrac{\partial c_V}{\partial t} = \nabla\cdot[D_V(f_F,f_B,f_E)\nabla c_V] & -\displaystyle\sum_{q\in\theta} r_V c_V \delta(\mathbf{x}-\mathbf{x}_q), & & (4.1)\\
\text{DLL4} & \dfrac{\partial c_D}{\partial t} = \nabla\cdot[D_D(f_F,f_B,f_E)\nabla c_D] & -\displaystyle\sum_{q\in\theta_s} r_D c_D \delta(\mathbf{x}-\mathbf{x}_q) & +\displaystyle\sum_{q\in\theta_t} s_D c_V \delta(\mathbf{x}-\mathbf{x}_q), & (4.2)\\
\text{uPA} & \dfrac{\partial c_U}{\partial t} = \nabla\cdot[D_U(f_F,f_B,f_E)\nabla c_U] & -r_U c_U f_F & +\displaystyle\sum_{q\in\theta_t} s_U c_V \delta(\mathbf{x}-\mathbf{x}_q), & (4.3)\\
\text{MMP} & \dfrac{\partial c_M}{\partial t} = \nabla\cdot[D_M(f_F,f_B,f_E)\nabla c_M] & -r_M c_M f_B & +\displaystyle\sum_{q\in\theta_t} s_M c_V \delta(\mathbf{x}-\mathbf{x}_q), & (4.4)
\end{array}$$

Substrates

$$\begin{array}{lllll}
\text{Fibrin} & \dfrac{\partial f_F}{\partial t} = & -r_F c_U f_F, & & (4.5)\\
\text{BM} & \dfrac{\partial f_B}{\partial t} = & -r_B c_M f_B, & & (4.6)\\
\text{ECF} & \dfrac{\partial f_E}{\partial t} = & & +r_F c_U f_F + r_B c_M f_B. & (4.7)\\
 & \underbrace{\hphantom{\nabla\cdot[D_V(f_F,f_B,f_E)\nabla c_V]}}_{Diffusion} & \underbrace{\hphantom{\sum r_D c_D \delta(\mathbf{x}-\mathbf{x}_q)}}_{Reaction} & \underbrace{\hphantom{\sum s_D c_V \delta(\mathbf{x}-\mathbf{x}_q)}}_{Sourcing} &
\end{array}$$

Note that the left hand side of the equations for the chemicals have dimension $\frac{ng}{\mu m^3 s}$. We then see that for the diffusive functions we must have $[D] = \frac{\mu m^2}{s}$. The Dirac delta distributions have dimension $\frac{1}{\mu m^3}$ and hence $[r_V] = [r_D] = \frac{\mu m^3}{s}$. However, $[r_U] = [r_M] = \frac{1}{s}$ and $[r_F] = [r_B] = \frac{\mu m^3}{ngs}$. The sourcing rates have dimension $[s_D] = [s_U] = [s_M] = \frac{\mu m^3}{s}$.

The four chemicals VEGF, DLL4, uPA and MMP also have different diffusion constants D_V, D_D, D_U and D_M measured in $\frac{\mu m^2}{s}$. The three different substrate components Fibrin, BM and ECF all have different permeabilities to let chemicals diffuse through them. We model this using the dimensionless constants D_F, D_B and D_E. The combined diffusive factor is given by the diffusive constant of the given chemical multiplied by a linear combination of the permeabilities of the substrate. We set $D_F = 1$ and scale D_B and D_E accordingly. Together we see four functions that make the diffusive process dependent on the composition of the substrate and the diffusive properties of the respective chemicals:

$$\begin{aligned}
D_V(f_F, f_B, f_E) &= D_V[f_F D_F + f_B D_B + f_E D_B],\\
D_D(f_F, f_B, f_E) &= D_D[f_F D_F + f_B D_B + f_E D_B],\\
D_U(f_F, f_B, f_E) &= D_U[f_F D_F + f_B D_B + f_E D_B],\\
D_M(f_F, f_B, f_E) &= D_M[f_F D_F + f_B D_B + f_E D_B].
\end{aligned}$$

Notes on the stationary points and stability of the PDEs are presented in Appendix E.5.

4.2.1. BOUNDARY VALUES AND INITIAL CONDITIONS

The sprouting assay takes place in a closed 96 well plate. No transport of chemicals can take place through the walls or bottom. Imposing a no-flux boundary condition

$$D_V \frac{\partial c_V}{\partial \mathbf{n}} = D_D \frac{\partial c_D}{\partial \mathbf{n}} = D_U \frac{\partial c_U}{\partial \mathbf{n}} = D_M \frac{\partial c_M}{\partial \mathbf{n}} = 0,$$

over the entire boundary Γ of our problem domain forms a natural boundary condition. We will use this boundary condition in the derivation of our Galerkin equations used in the FEM that we use to numerically solve the system of PDEs in Equation C.1.

The initial conditions for the substrate components is formulated by the dimensions of the sprouting assay. We know that in the sprouting assay, a well has a diameter of $d_{top} = 7mm$ and we fill the wells with $vol_F = 100\mu L = 1mm^3$ of fibrinogen and thrombin. We have the relation $\pi r^2 h = 100$ and the height of the fibrin in the well is $h_{\text{sub}} = \frac{100}{\pi 3.5^2} mm$. The top layer consists of boundary membrane and we assume this layer has a thickness equal to the diameter of the ECs, i.e. $2R$. For a point $\mathbf{x} = (x, y, z)$ we impose

$$f_F(\mathbf{x}) = \begin{cases} 1 \text{ if } z < h_{\text{sub}} - 2R \\ 0 \text{ otherwise} \end{cases}, \quad f_B(\mathbf{x}) = \begin{cases} 1 \text{ if } h_{\text{sub}} - 2R \leq z < h_{\text{sub}} \\ 0 \text{ otherwise} \end{cases}, \quad f_E(\mathbf{x}) = \begin{cases} 1 \text{ if } z \geq h_{\text{sub}} \\ 0 \text{ otherwise} \end{cases},$$

Since in our FEM we only impose initial conditions on the nodal point, we see that for a nodal point n with z-coordinate z_n this translates to

$$f_F(n) = \begin{cases} 1 \text{ if } z_n < h_{\text{sub}} - 2R \\ 0 \text{ otherwise} \end{cases}, \quad f_B(n) = \begin{cases} 1 \text{ if } h_{\text{sub}} - 2R \leq z_n < h_{\text{sub}} \\ 0 \text{ otherwise} \end{cases}, \quad f_E(n) = \begin{cases} 1 \text{ if } z_n \geq h_{\text{sub}} \\ 0 \text{ otherwise} \end{cases}, \tag{4.8}$$

Note that since our FEM mesh is unstructured and the concentrations inside the elements is linearly interpolated, we do not start with a perfectly flat substrate surface. For a fine discretization however, this effect is smaller.

ECs are not activated by the lack of a VEGF gradient and are all assumed stalk cells at the beginning of the sprouting assay. This entails that none of the three chemicals that source from tip cells is present initially. At the start of the experiment, a VEGF concentration of concentration c_V^0 is added and we model that this concentration is only present within the fibrin scaffold. The initial conditions are then given by

$$c_V(\mathbf{x}) = \begin{cases} c_V^0 \text{ if } z < h_{\text{sub}} - 2R \\ 0 \text{ otherwise} \end{cases}, \quad c_D(\mathbf{x}) = 0, \quad c_U(\mathbf{x}) = 0, \quad c_M(\mathbf{x}) = 0.$$

4.2.2. SOLVING THE SYSTEM OF PDES AND TIME STEPPING

The PDEs can be solved in different ways and we choose to to implement a finite element scheme with linear basis functions as fully described in Appendix C. We perform the time stepping using a variable time step IMEX scheme described in Appendix E. In this Appendix we will also make some notes on spurious oscillations occurring caused by the FEM scheme and how to account for this.

4.3. SUBSTRATE DEPENDENT CELL MOVEMENT

We introduced the dynamics of the chemicals and the substrate components and subsequently we propose equations for the cell dynamics. The haptotactic mechanics are based on the 3-D counterpart of the work by Vermolen and Gefen [8] as was introduced in Section 3.3. We come up with new formalisms for chemotaxis and cell-matrix adhesion and we implement gravity in a straightforward physical sense.

An overview of the cells on the substrate with the given forces acting upon them is given in Figure 4.2. Note that this is a simplified impression of the model since it is two dimensional and the substrate components are displayed as discrete layers whilst in the model we have a continuous mixture.

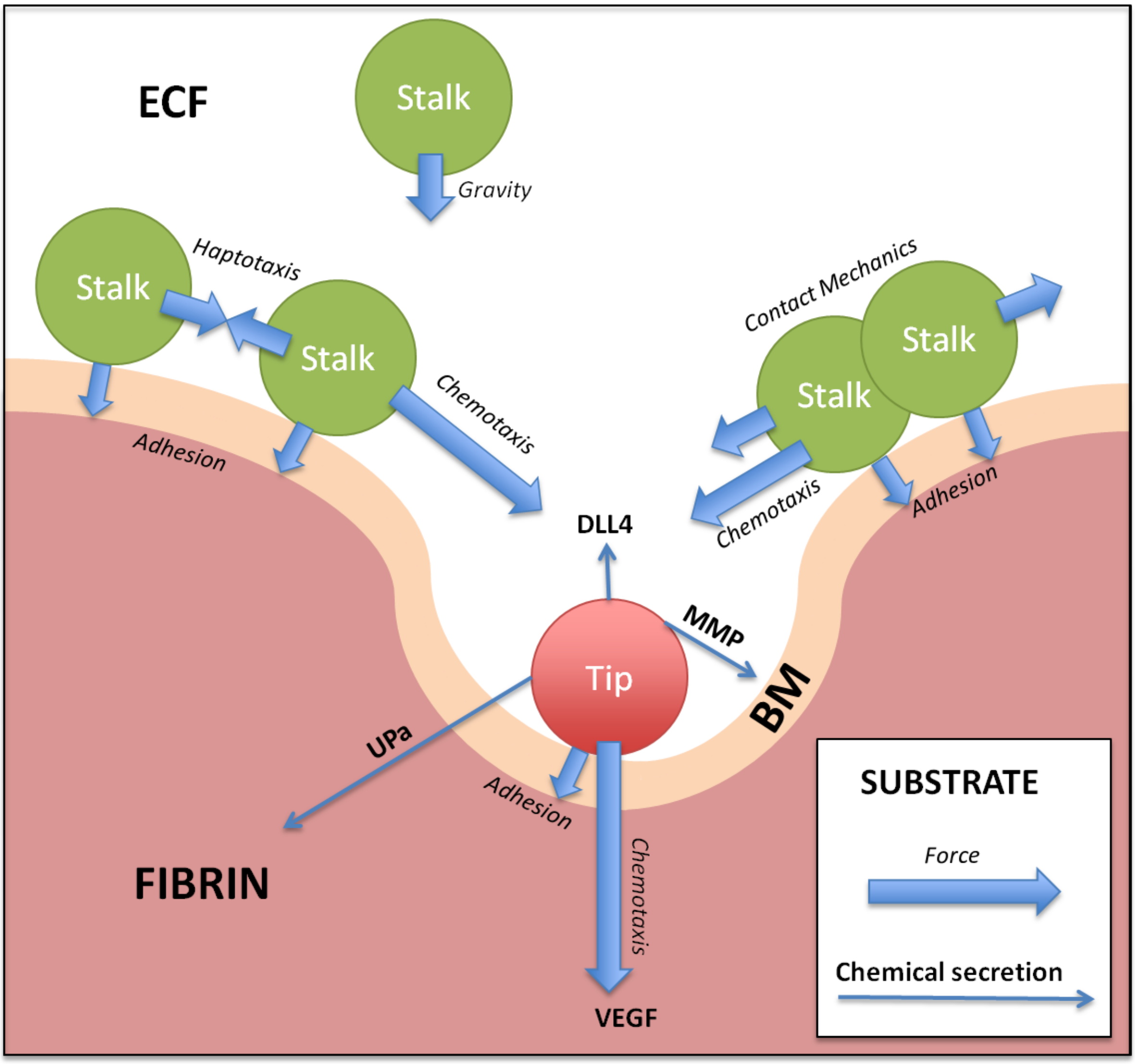

Figure 4.2: Schematic overview of the different forces acting upon cells based on their position with respect to other cells, the substrate and chemical gradients. Thick arrows represent forces. Thin arrows represent secretion of chemicals.

The dynamics of a cell i at location $\mathbf{r}_i$ are of the form

$$d\mathbf{r}_i = dt\left[\underbrace{\alpha M(\mathbf{r}_i)\hat{z}}_{Haptotaxis} + \underbrace{\gamma(\delta_{i\in\theta_s}\nabla c_D + \delta_{i\in\theta_t}\nabla c_V)}_{Chemotaxis} + \underbrace{\lambda\nabla f_S}_{Adhesion} + \underbrace{v_g}_{Gravity}\right] + \underbrace{\sigma_W dW_t}_{Diffusion}. \tag{4.9}$$

Here, α is a parameter governing the haptotactic response as was formulated before by Vermolen and Gefen [8]. Further, γ is a parameter governing the chemotactic response, λ is a parameter governing the adhesive strength, v_g is the velocity due to gravitation and W_t is a stochastic Wiener process with corresponding standard deviation $\sigma_W\sqrt{dt}$. Tip cells (stalk cells) chemotact towards the VEGF gradient (DLL4 gradient) only and this is monitored by $\delta_{i\in\theta_t}$ ($\delta_{i\in\theta_s}$) being 1 if cell i is a tip cell (stalk cell) and 0 otherwise. Cells adhere to the substrate and since the substrate consists of both fibrin and BM, cells adhere to the combined substrate denoted by $f_S := f_F + f_B$. The adhesive movement is in the direction of the combined substrate gradient $\nabla f_S = \nabla(f_F + f_B)$.

We will hereafter show that all parameters α, γ, λ and v_g are substrate dependent and we may write $\alpha = \alpha(\mathbf{r}_i), \gamma = \gamma(\mathbf{r}_i), \lambda = \lambda(\mathbf{r}_i)$ and $v_g = v_g(\mathbf{r}_i)$. We will formulate in subsequent sections how all parameters are formulated and how they depend on the substrate composition. The variable time step predictor-corrector scheme we propose to use can be found in Appendix D.

4.3.1. HAPTOTAXIS AND CONTACT MECHANICS IN A 3D SETTING

In the 3 dimensional setting, spherical cells act a force along their entire cell surface, opposed to their circular perimeter in the 2 dimensional model by Vermolen and Gefen [8]. We account for this by substituting the perimeter in Equation 3.2 by the cell surface $\mathrm{Surf}_i = 4\pi R^2$ and see

$$M_i^0 = \frac{1}{2}E_s\epsilon^2 = \frac{1}{2}E_s\left(\frac{1}{E_s}\frac{F_i}{\mathrm{Surf}_i}\right)^2 = \frac{1}{2}E_s\left(\frac{1}{E_s}\frac{F_i}{4\pi R^2}\right)^2 = \frac{F_i^2}{32E_s\pi^2R^4}.$$

In the setting where the substrate continuously degrades from fibrin and BM into ECM, we model the elasticity of the substrate as

$$E_s = E_s(\mathbf{r}_i) = \frac{f_F}{f_F + f_B}E_F + \frac{f_B}{f_F + f_B}E_B,$$

where E_F and E_B are the elastic moduli of fibrin and BM. The new local elastic modulus of the substrate is a linear combination of the elastic moduli of fibrin and BM weighted by their fractions. If the environment is completely ECF, cells have no fibrous matter to exert any pulling forces on and there will not be any generated strain energy. We reduce the force for increasing f_E linearly using a term $(1 - f_E)$ and we conclude that

$$M_i^0 = \frac{F_i^2(1 - f_E)}{32E_s(\mathbf{r}_i)\pi^2R^4}.$$

The strain energy decays exponentially by increasing radius as modeled by Vermolen and Gefen [8] with a factor $\frac{E_s}{E_c}$. The elastic modulus acts as a "spring constant" of the elastic medium in between the cells i and j and hence it makes sense to use the mean value of $E_s(\mathbf{r}_i)$ and $E_s(\mathbf{r}_j)$, i.e. $E_s(\mathbf{r}_i, \mathbf{r}_j) = \frac{E_s(\mathbf{r}_i)+E_s(\mathbf{r}_j)}{2}$ and we see

$$M_i(\mathbf{r}) = \frac{F_i^2(1 - f_E)}{2\pi^2E_s(\mathbf{r}_i)R^4}\exp\left(-\frac{E_s(\mathbf{r}_i, \mathbf{r}_j)}{E_c}\frac{\|\mathbf{r} - \mathbf{r}_i\|}{R}\right). \tag{4.10}$$

The strain caused by contact mechanics between cells also differs in the 3 dimensional setting. A relation between the produced strain M_{ij} as a function of the depth h cells have to dent due to collision in 3 dimensions has already been derived by Dudaie et al. in [40]. A schematic representation of the distance h (in 2 dimensions) is given in Figure 4.3. They conclude that the 3 dimensional counterpart of Equation 3.4 reads

$$M_{ij} = \frac{\sqrt{2}}{5\pi}E_c\left(\frac{h}{R}\right)^{\frac{5}{2}},$$

where $h = \max\left\{\frac{2R-\|\mathbf{r}_i-\mathbf{r}_j\|}{2}, 0\right\}$ and thus we see

$$M_{ij} = \begin{cases} \frac{\sqrt{2}}{5\pi}E_c\left(1 - \frac{\|\mathbf{r}_i-\mathbf{r}_j\|}{2R}\right)^{\frac{5}{2}}, & \text{for } \|\mathbf{r}_i - \mathbf{r}_j\| < 2R, \\ 0 & \text{for } \|\mathbf{r}_i - \mathbf{r}_j\| \geq 2R, \end{cases}$$

for cells i and j in contact and $M_{ij} = 0$ otherwise. Now given a cell i we subtract the contact mechanical strain M_{ij} caused by cell j from the haptotactic strain $M_j(\mathbf{r}_i))$ caused by j and we end up with the total strain felt by cell i

$$M(\mathbf{r}_i) = M_i^0 + \sum_{j=1_{j\neq i}}^{N} \left[M_j(\mathbf{r}_i) - M_{ij}\right].$$

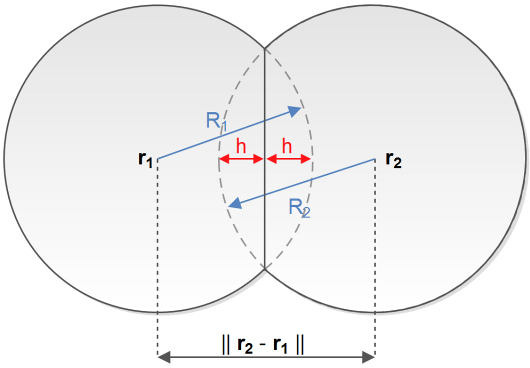

Figure 4.3: Given a cells with centers $\mathbf{r}_1$ and $\mathbf{r}_2$, the dent distance h is given in this figure. The graphics are taken from unpublished work by Vermolen and van der Meijden [39].

When calculating the value for $\alpha_i = \frac{\beta_i R^3}{\mu(\mathbf{r}_i)F_i}$, we have to take the composition of the substrate into account too. The parameters β_i, R and F_i are cell-specific and will not change. The friction constant μ however will be higher within fibrin and on the BM. We model the frictions caused by the different substrate fractions to be proportional to their elastic moduli. Noting that in the original model by Vermolen and Gefen [8] the friction caused by the fibrin was equal to $\hat{\mu}$, we set

$$\mu_i = \mu(\mathbf{r}_i) = \hat{\mu}\left(f_F(\mathbf{r}_i)\frac{E_F}{E_F} + f_B(\mathbf{r}_i)\frac{E_B}{E_F} + f_E(\mathbf{r}_i\frac{E_E}{E_F}\right).$$

The derivation of $\hat{z}_i$ remains unchanged. This concludes the derivation of all terms in the haptotactic part of the cell dynamics in Equation 4.9.

4.3.2. CHEMOTAXIS

We distinguish between tip cells and stalk cells for the chemotactic movement. Tip cells chemotact towards the VEGF gradient ∇c_V present in the substrate. Stalk cells chemotact towards the DLL4 gradient ∇c_D secreted by the tip cells.

Dimensional analysis dictates that $[\gamma\nabla c_V] = \frac{\mu m}{s}$. Since $[\nabla c_V] = \frac{ng}{\mu m^4}$ we must have $[\gamma] = \frac{\mu m^5}{ngs}$. We take into account four factors: the cell motility ($[\beta] = \frac{1}{s}$), the maximal exerted force ($[F_i] = nN$), the elastic modulus of the substrate ($[E_S] = \frac{nN}{\mu m^2}$) and the density of the substrate denoted by ρ_S. The local density is dependent on the substrate composition and we argue that it must be equal to the weighted average of the densities of the different components:

$$\rho_S = \rho_S(\mathbf{r}_i) = f_F(\mathbf{r}_i)\rho_F + f_B(\mathbf{r}_i)\rho_B + f_E(\mathbf{r}_i)\rho_E. \tag{4.11}$$

We see $[\rho_S] = \frac{ng}{\mu m^3}$. It is reasonable to assume that the chemotactic cell velocity increases when the motility and the exerted force increase and decreases when the density or elastic modulus of the matrix increases. Furthermore, whenever f_S tends to 1, the matrix is so dense that we have almost no movement. Whenever f_E tends to 1, the cells have nothing substantial to "pull" on and we also have almost no movement. We correct for these two effects using a term $f_S f_E$ and conclude

$$\gamma = \gamma(\mathbf{r}_i) = \frac{\beta F_i}{E_S(\mathbf{r}_i)\rho_S(\mathbf{r}_i)}[f_F(\mathbf{r}_i) + f_B(\mathbf{r}_i)]f_E(\mathbf{r}_i). \tag{4.12}$$

We indeed have $[\gamma] = \frac{\mu m^5}{ngs}$.

4.3.3. CELL-MATRIX ADHESION

We model cell-matrix adhesion by assuming that cells move towards locations with a combined substrate density $f_S := f_F + f_B = 0.5$. The direction of the movement is towards increasing substrate density ∇f_S for substrate densities $f_S < 0.5$ and towards decreasing substrate density for substrate densities $f_S > 0.5$. The strength of the cell's response to adhesion is monitored by a parameter λ.

Dimensional analysis dictates that $[\lambda \nabla f_S] = \frac{\mu m}{s}$. Since $[\nabla f_S] = \frac{1}{\mu m}$, we must have $[\lambda] = \frac{\mu m^2}{s}$. As with the chemotactic parameter γ, we take into account the cell motility ($[\beta] = \frac{1}{s}$), the maximal exerted force ($[F_i] = nN$) and the elasticity of the substrate ($[E_S] = \frac{nN}{\mu m^2}$) and follow the same reasoning as in the derivation of the chemotaxis parameter γ. Furthermore, in order to make cells adhere to substrate densities $f_S = 0.5$, we multiply by a dimensionless polynomial $Q(f_S)$. We see

$$\lambda = \lambda(\mathbf{r}_i) = \frac{\beta_i F_i}{E_S(\mathbf{r}_i)} Q(f_S(\mathbf{r}_i)), \tag{4.13}$$

and check that indeed $[\lambda] = \frac{\mu m^2}{s}$. We try to find a suitable polynomial by reasoning from a biochemical point of view. Cells completely dissolved in ECF have no substrate to adhere to and we must have $\lambda = 0$ for $f_S = 0$. Cells that are completely surrounded by substrate are not able to move because of the matrix stiffness and we must have $\lambda = 0$ for $f_S = 1$. Finally, cells that are already at a 50% substrate density must not move and we must have $\lambda = 0$ for $f_S = 0.5$. λ must be positive for substrate densities below 50 % and and negative for substrate densities above 50 %. Polynomial $Q(f_S(\mathbf{r}_i)$ that has all these properties and is normalized to have a maximum value of 1:

$$Q(f_S(\mathbf{r}_i)) = 12\sqrt{3} f_S(\mathbf{r}_i)[f_S(\mathbf{r}_i) - \tfrac{1}{2}][f_S(\mathbf{r}_i) - 1]. \tag{4.14}$$

Implementing this $\lambda(\mathbf{r}_i)$ leads to a very low response to adhesion. Apparently there is some factor of importance that we do not take into account. We use a factor $\hat{\lambda} = 15$ to scale the adhesive movement to the haptotactic and chemotactic movements. Improvements upon equation 4.13 or 4.14 can be introduced to make this factor obsolete. In Chapter 5, we will perform a sensitivity analysis on this parameter to find out what the effect of a faulty estimate of the parameter $\hat{\lambda}$ is on the model outcome. Furthermore we refer to Chapter 6 with recommendations for future research into this topic.

4.3.4. GRAVITY

We incorporate gravity using the Newton's first law $\sum F = ma$. Assuming $a = 0$ to make computations easy does not work in practice since cells then "fall" at terminal velocity which requires a very small time step to obtain stable results. This however does entail storing the previous gravitational speed v_i^{k-1} for a cell i in order to approximate $a_i^k \approx \frac{v_i^k - v_i^{k-1}}{\Delta t}$ using a finite difference scheme. In our force balance we incorporate gravitational force F_g, buoyant force F_b and drag force F_d. Gravitational force is in the downward direction and of magnitude $m_c * g$ where the subscript c stands for "cell". We know that $m_c = \rho_c V_c$, where ρ_c is the density of the cell and $V_c = \frac{4}{3}\pi R^3$ is the volume of the cell. The buoyant force is in the upward direction and of magnitude $F_b = m_S g = \rho_S V_c g$ where the s stands for "substrate", ρ_S is the local substrate density as defined in Equation 4.11. The drag force is defined by Stokes law for frictional force as $F_d = 6\pi\mu_S R v$, where μ_S is the viscosity of the substrate and R is the radius of the spherical cell and $v = \frac{d\mathbf{r}}{dt}$. The drag force is slowing down movement and is in the opposite direction of the initial velocity v^{k-1}. We set $v^0 = 0$ as initial condition for the recursive relation for the acceleration. We sum all forces and isolate the speed at time step k to derive a recursive relation for the gravitational speed for cell i.

$$
\begin{array}{rrrcl}
-F_g & +F_b & -\mathrm{Sign}(v_i^{k-1})F_d & = & ma\\
-\rho_c V_c g & +\rho_S V_c g & -\mathrm{Sign}(v_i^{k-1})6\pi\mu_S R v_i^{k-1} & = & \rho_c V_c \dfrac{v_i^k - v_i^{k-1}}{\Delta t}\\
 & (\rho_S-\rho_c)V_c g & -\mathrm{Sign}(v_i^{k-1})6\pi\mu_S R v_i^{k-1} & = & \rho_c V_c \dfrac{v_i^k - v_i^{k-1}}{\Delta t}\\
 & & \dfrac{\Delta t}{\rho_c}\left[(\rho_S-\rho_c)g - \mathrm{Sign}(v_i^{k-1})\dfrac{9\mu_S}{2R^2}v_i^{k-1}\right] & = & v_i^k - v_i^{k-1}\\
 & v_i^{k-1} & +\dfrac{\Delta t}{\rho_c}\left[(\rho_S-\rho_c)g - \mathrm{Sign}(v_i^{k-1})\dfrac{9\mu_S}{2R^2}v_i^{k-1}\right] & = & v_i^k
\end{array}
$$

The viscosity μ_S is again dependent on the substrate composition and we take a linear combination of the viscosities of the different substrate components:

$$\mu_S = \mu_S(\mathbf{r}_i) = f_F(\mathbf{r}_i)\mu_F + f_B(\mathbf{r}_i)\mu_B + f_E(\mathbf{r}_i)\mu_E.$$

4.3.5. DIFFUSION

We model the diffusion of cells by adding stochastic movement to the cells. We will use a different approach than Vermolen and Gefen [8] by adding a 3 dimensional Wiener process $\sigma_W \mathbf{W}_t = \sigma_W [W_t^1, W_t^2, W_t^3]^T$ having $\mathbf{W}_0 = 0$ with for $0 \leq s \leq t$ having $W_t^i - W_s^i \sim N(0, t-s)$ for $i = 1,2,3$. It follows that $t \to \mathbf{W}_t$ continuous a.e.. Discretized, this entails drawing random numbers $N \sim \mathcal{N}(0,1)$ and adding $\sigma_W \sqrt{\Delta t} N$ to the displacement.

4.4. TIP CELL SELECTION AND CONTROLLING MOTILITY

The fact that ECs can change from stalk cells to tips cells based on local chemical conditions is of essential importance to the sprout formation. Higher VEGF concentrations will stimulate tip cell selection while higher concentrations of DLL4, secreted by tip cells themselves, will inhibit the selection process. We propose a probabilistic model for the selection process and we consider options for differentiation in cell-type behavior.

4.4.1. CELL DIFFERENTIATION

EC's can change from stalk cells into tip cells (and reversibly) based on the local chemical properties[2]. Higher concentrations of VEGF will increase the chance of a stalk cell to become a tip cell. However, a nearby tip cell that sources DLL4 inhibits a stalk cells from becoming tip cells.

We model the changing time of a stalk cell to become a tip cell using an exponential distribution with a rate $\tilde{\lambda}_{ST}$. We also model the changing time of a tip cell to change back into a stalk cell using an exponential distribution with rate $\tilde{\lambda}_{TS}$. The probability density function (PDF) of the exponential distribution is given by

$$f(t,\lambda) = \begin{cases} \lambda e^{-\lambda t} & \text{for } t \geq 0, \\ 0 & \text{for } t < 0. \end{cases}$$

The changing times are then distributed as

$$\mathbb{P}(T|S) \sim \mathrm{Exp}(\tilde{\lambda}_{ST}) \quad \text{and} \quad \mathbb{P}(S|T) \sim \mathrm{Exp}(\tilde{\lambda}_{TS}).$$

The rates $\tilde{\lambda}_{ST}$ and $\tilde{\lambda}_{TS}$ are dependent on cell specific factors and local chemical conditions. Since the concentration VEGF c_V only decreases over time, we know that we have $c_V^{max} = c_V^0$ and we normalize using $\frac{c_V}{c_V^{max}}$. The concentration DLL4 c_D can take arbitrary positive values but in practice almost never exceeds the concentrations VEGF so again we "normalize" by setting $\frac{c_D}{c_V^{max}}$. For ideal circumstances, i.e. $c_V = c_V^{max}$ and $c_D = 0$, we define the maximal rate of changing from stalk to tip per second to be p_{ST}. The rate $\tilde{\lambda}_{ST}$ increases for increasing c_V and decreases for increasing c_D. We model

---

[2] In our computational model, this option can be used by setting the `g.cell0.cellDifferentiation` = 1. Otherwise tip cells are selected randomly in the initial distribution.

$$\tilde{\lambda}_{ST}(c_V, c_D) = p_{ST} e^{-p_s\left(1-\frac{c_V}{c_V^{max}}\right)} e^{-p_i \frac{c_D}{c_V^{max}}}. \tag{4.15}$$

The strength of the DLL4 induced inhibition is governed by the parameter p_i (i for inhibition) and higher values of p_i constitute stronger inhibition. The strength of the stimulation by VEGF is governed by the parameter p_s (s for stimulation) and lower values of p_s constitute stronger stimulation even for low values of c_V. We plot the rate function $\tilde{\lambda}_{ST}(c_V, c_D)$ with parameters $p_s = 4$, $p_i = 10$ and $p_m = 0.0001$ for different values of the chemical concentrations in Figure 4.4.

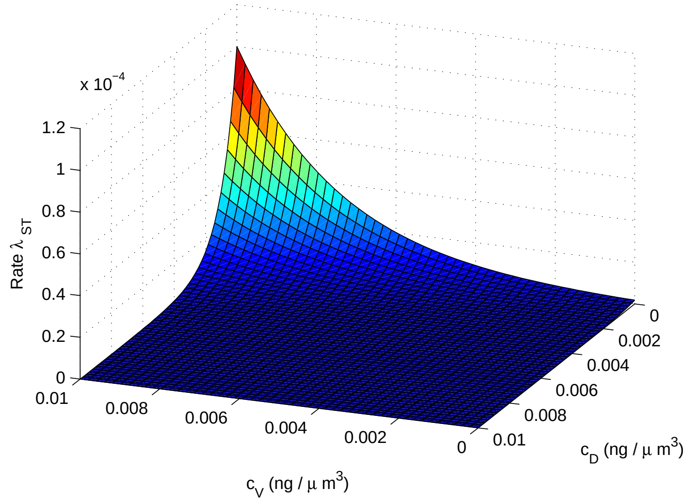

Figure 4.4: The rate $\tilde{\lambda}_{ST}(c_V, c_D)$ of stalk cells changing into a tip cells for different values of $0 \leq c_V \leq 0.01$ and $0 \leq c_D \leq 0.01$. The maximum value is p_m is attained for $c_V = 0.01$ and $c_D = 0$, i.e. maximal stimulation without inhibition. The inhibiting effect is stronger than the stimulating effect because $p_i = 10 > p_s = 4$.

Tip cells can change back into stalk cells at a rate governed by the decreasing of a VEGF gradient. We model

$$\tilde{\lambda}_{TS}(c_V) = p_{TS} e^{-p_s \frac{c_V}{c_V^{max}}}, \tag{4.16}$$

and set $p_{TS} = 1 \cdot 10^{-6}$. The rates in Equations 4.15 and 4.16 are per second. During a time step of length Δt, we see that we have the following probability of a cell type change, where we approximate the exponential with its first order Taylor expansion around $t = 0$.

$$\int_0^{\Delta t} \tilde{\lambda} e^{-\tilde{\lambda} t} dt = \left[1 - e^{-\tilde{\lambda} t}\right]_0^{\Delta t} = 1 - e^{\tilde{\lambda}\Delta t} \approx 1 - (1 - \tilde{\lambda}\Delta t) = \tilde{\lambda}\Delta t.$$

This approximation is suitable for small enough time steps Δt, and we have to specifically ensure that $\tilde{\lambda}_{TS}\Delta t \leq p_{TS}\Delta t \leq 1$. Bayes theorem now dictates that $\frac{P(S|T)}{P(T|S)} = \frac{P(S)}{P(T)}$ and we end up with an equilibrium ratio between tip cells and stalk cells given the local chemical conditions.

The values for p_m, p_s and p_i should be found based on experimental data. Microscopic images show us that for large concentrations of VEGF ($25\frac{ng}{mL}$), we see around one sprout for every fifty ECs after two days. We assume that every sprout is led by one tip cell. Furthermore we assume that all tip cells are selected at 12 hours after stimulation with VEGF and that no additional tip cells are formed due to inhibition by the existing ones afterwards. This means that a cell has a probability of 0.02 per 12 hours of becoming a tip cell not changing back again. This is equivalent to $\frac{0.02}{12 \cdot 3600} = 4.6 \cdot 10^{-7}$ per second. The VEGF concentration is not maximal over the entire domain, so we choose $p_m = 4 \cdot 10^{-6}$. We know that the inhibiting effect of DLL4 is stronger than the stimulating effect by VEGF, so we model $p_i = 10$ and $p_s = 4$ and conclude that these values are suitable for our modeling purposes. Better estimations for these values might be obtained by fitting model results to experimental observations, but this is cumbersome due to the long execution time of the model. An investigation of the magnitude of these parameters reasoning from a more biochemical point of view is a useful recommendation.

4.4.2. DIFFERENT MOTILITY TIPS AND STALKS

This model could be easily extended to give tip cells and stalk cells different parameters. A possibility is to give tip cells a higher motility constant β_i to make them more motile. After consulting the dermatology department on this matter, we found that no biochemical or biological reason exists that makes such an assumption reasonable. Therefore we take the value of β_i equal for all cells $i = 1, \dots, N$.

Dudaie et al., in unpublished work [40], use a model that is in many ways similar to our model. They do differ the value of β_i for different cells and approximating the motility with a Gamma distribution function.

4.5. PARAMETERS AND DOMAIN

Our model uses a number of parameters, most of a physical or chemical nature. We try to find accurate values for these parameters in literature as much as possible although some values are hard to estimate. We list all our parameters with description, symbol, programming code name, value, dimension and where possible a source in Tables 4.1, 4.2, 4.3 and 4.4.

The elastic modulus of endothelial cells E_c is approximately 10 kPa according to Kuznetsova et al. [42]. They found this value in a study using atomic force microscopy probing. This is higher than the value used in the model by Vermolen and Gefen [8].

According to the work of Ganz et al. [43], traction forces F_i are also higher than the $1nN$ used by Vermolen and Gefen [8]. Reinhart-King et al. [37] conducted *in vitro* studies measuring the forces exerted by ECs on polyacrylamide substrates. On page 1578 we see see the relation between cell area and exerted force of ECs. Since we model our cell radius as $R = 22.5\mu m$, we have an area of $22.5^2\pi = 1590\mu m^2 = 1.59 \cdot 10^{-5} cm^2$. The graph gives a force of $0.1 dyne = 10^{-6} N = 1000 nN$ and we choose to use this value in our model. Using this value gives more realistic movements in our simulations than copying the 1 nN used by Vermolen and Gefen [8].

Elasticity of fibrin E_F is approximately 10 kPa according to Rowe et al. [44]. Zhu et al. [45] propose values for the elastic modulus of collagen-chitosan scaffolds in the order of 10 kPa. Since BM consist of collagen and more stiff components, we use an estimate $E_B = 20kPa$.

Plank et al.[46] set the diffusion coefficient for VEGF $D_V = 3.6 \times 10^{-3} \frac{mm^2}{h} = 1 \frac{\mu m^2}{s}$ (in matrigel). We have found no references on the diffusion coefficients of the concentrations DLL4, uPA and MMP so we estimate them using their molecular weights. We assume that substances diffuse more slowly for larger molecular weights. All four substances are sold commercially and molecular weights m are specified very accurately. We see that $m_V \approx 38.2kDa$[3], $m_D \approx 75kDa$[4], $m_U \approx 31kDa$[5] and $m_M \approx 72kDa$[6]. We estimate

$$D_D = \frac{m_V}{m_D} D_V = 0.51, \qquad D_U = \frac{m_V}{m_U} D_V = 1.23, \qquad D_M = \frac{m_V}{m_M} D_V = 0.53,$$

all measured in $\frac{\mu m^2}{s}$. Contradictorily, Bauer et al. [47] sets the diffusion coefficient for VEGF to 1698 $\frac{\mu m^2}{s}$ and Miura et al. [48] measured in an *in vitro* experiments that the VEGF diffusion constant in matrigel (similar to fibrin gel) is equal to $278 \frac{\mu m^2}{s}$. The coefficient used by Plank et al. [46] seems to make the most physical sense and produces reasonable results in our computational model. Further research into the difference between these values might be useful.

Plank et al. [46] furthermore set the VEGF uptake rate r_V within cells to $8.66 \cdot 10^{-5} \frac{mm^2}{h} = 0.024 \frac{\mu m^2}{s}$. Note that Plank et al. work in a 2D setting and that in the 3D setting, the dimension would be $\frac{mm^3}{s}$. We set the uptake rates r_D, r_U and r_M equal to this value since we could not find any references concerning these quantities.

The degrading rate r_F of the fibrin fraction by uPA is, according to Lutolf et al. [49] of magnitude 1.21 s^{-1} and we use this value in our model. We estimate that the degrading rate r_B of the BM by MMP is of the same

---

[3] `http://www.shenandoah-bt.com/Human_Vascular_Endothelial_Growth_Factor-165.html`

[4] `http://www.phosphosite.org/proteinAction.do?id=24218`

[5] `http://www.oxfordbiomed.com/active-mouse-upa-functional-assay-kit`

[6] `http://www.rndsystems.com/mini_review_detail_objectname_MR99_MMPs.aspx`

magnitude.

Viscosity of water is $0.6531 \cdot 10^{-3} \frac{Ns}{m^2}$ at 40 degrees centigrade and $0.7978 \cdot 10^{-3} \frac{Ns}{m^2}$ at 30 degrees centigrade according to Streeter [50]. Our experiment is conducted in an incubator at 37 degrees and we therefore take $\mu_E = 0.6965 \cdot 10^{-3} \frac{Ns}{m^2}$. Viscosity fibrin is approximately $7.000 \cdot 10^{-3} \frac{Ns}{m^2}$ according to Ehrlich [51].

According to Urbanchek et al. [22] the density of myocytic cells is $1.060^1 0^{-3} \frac{kg}{cm^3}$. Water at 37 degrees centigrade has a density of $0.9933 \cdot 10^{-3} \frac{g}{cm^3}$.

We model one well in a 96 well plate. We take the same dimensions of diameter 7 mm (i.e. $d_{top} = 7000 \mu m$) and a height determined by filling the well with $v_F = 100 \mu L$ fibrin and 100 μL fluid to a total of $v = 200 \mu L$ with $N = 20.000$ suspended EC's. This mimics the laboratory setting one-to-one. To decrease computational time and load on memory, we introduce a linear scaling factor ξ and we have scaled domain parameters $\tilde{v} = \frac{v}{\xi^3}$, $\tilde{v}_F = \frac{v_F}{\xi^3}$, $\tilde{d}_{top} = \frac{d_{top}}{\xi^2}$ and $\tilde{N} = \frac{N}{\xi^2}$ to keep an equal aspect ratio of the domain and a monolayer of cells that is constant in density (cells per μm^2).

Table 4.1: Domain parameters

Parameter	**Symbol**	**Code name**	**Value**	**Dimension**	**Source**
Domain scaling factor	ξ	`g.dom.scaling`	[1 - 10]	-	-
Diameter well	d_{top}	`g.dom.dTop`	7000	μm	experiment
Volume well	v	`g.dom.vol`	200	μL	experiment
Volume fibrin	v_F	`g.dom.volFibrin`	100	μL	experiment

Table 4.2: Chemical simulation parameters

Parameter	**Symbol**	**Code name**	**Value**	**Dimension**	**Source**
Substrate threshold	f_0	`g.chemP.minThres`	boolean	-	-
Diffusion coef. VEGF	D_V	`g.chemP.dV`	1.00	$\mu m^2 s^{-1}$	[46]
Diffusion coef. DLL4	D_D	`g.chemP.dD`	0.51	$\mu m^2 s^{-1}$	Est. on [46]
Diffusion coef. uPA	D_U	`g.chemP.dU`	1.23	$\mu m^2 s^{-1}$	Est. on [46]
Diffusion coef. MMP	D_M	`g.chemP.dM`	0.53	$\mu m^2 s^{-1}$	Est. on [46]
Diffusion factor Fibrin	D_F	`g.chemP.dF`	1.00	-	-
Diffusion factor BM	D_B	`g.chemP.dB`	2.00	-	-
Diffusion factor ECF	D_E	`g.chemP.dE`	0.10	-	-
Reactive rate VEGF	r_V	`g.chemP.rV`	0.024	$\mu m^3 s^{-1}$	[46]
Reactive rate DLL4	r_D	`g.chemP.rD`	0.024	$\mu m^3 s^{-1}$	Est. on [46]
Reactive rate. uPA	r_U	`g.chemP.rU`	0.024	s^{-1}	Est. on [46]
Reactive rate MMP	r_M	`g.chemP.rM`	0.024	s^{-1}	Est. on [46]
Reactive rate Fibrin	r_F	`g.chemP.rU`	1.210	$\mu m^3 ng^{-1} s^{-1}$	[49]
Reactive rate BM	r_B	`g.chemP.rM`	1.210	$\mu m^3 ng^{-1} s^{-1}$	Est. on [49]
Sourcing rate DLL4	s_D	`g.chemP.sD`	10.00	$\mu m^3 s^{-1}$	-
Sourcing rate uPA	s_U	`g.chemP.sU`	10.00	$\mu m^3 s^{-1}$	-
Sourcing rate MMP	s_M	`g.chemP.sM`	10.00	$\mu m^3 s^{-1}$	-
Initial density VEGF	c_V^0	`g.chemP.iV`	0.01	$ng \mu m^{-3}$	-

Table 4.3: Cell parameters

Parameter	**Symbol**	**Code name**	**Value**	**Dimension**	**Source**
The number of cells in the well	N	`g.cell.nCells`	20.000	-	experiment
Radius of an EC	R	`g.cell.rCell`	22.5	μm	-
Elastic modulus of an EC	E_c	`g.cell.Ec`	10	$nN\mu m^{-2}$	[42]
Maximal exerted force of an EC	F_i	`g.cell.Fi`	1000	nN	[37, 43]
Motility of the cell surface	β_i	`g.cell.beta`	0.02	s^{-1}	[8]
Friction coefficient	$\hat{\mu}$	`g.cell.muHat`	0.2	-	[8]
Adhesive scaling factor	$\hat{\lambda}$	`g.cell.lambda`	15	-	-
Density of an EC	P_c	`g.cell.densityC`	$1.030 \cdot 10^{-3}$	$ng\mu m^{-3}$	[22]
St. dev. of stoch. movement	σ_W	`g.cell.sigmaW`	[0 - 0.1]	μm	-
Gravitational constant	g	`g.cell.gravitation`	$9.810 \cdot 10^{+6}$	$\mu m s^{-2}$	-
Max. prob. stalk becoming tip	p_{ST}	`g.cell.pMaximumS2T`	$4.000 \cdot 10^{-6}$	s^{-1}	-
Governs tip cell stimulation	p_s	`g.cell.pStimulation`	4	-	-
Governs tip cell inhibition	p_i	`g.cell.pInhibition`	10	-	-
Max. prob. tip becoming stalk	p_{TS}	`g.cell.pMaximumT2S`	$1.000 \cdot 10^{-6}$	s^{-1}	-

Table 4.4: Substrate Parameters

Parameter	**Symbol**	**Code name**	**Value**	**Dimension**	**Source**
Elastic modulus fibrin	E_F	`g.sub.Ef`	10	$kPa = nN\mu m^{-2}$	[44]
Elastic modulus BM	E_B	`g.sub.Eb`	20	$kPa = nN\mu m^{-2}$	[45]
Elastic modulus ECF	E_E	`g.sub.Ee`	1	$kPa = nN\mu m^{-2}$	-
Viscosity fibrin	μ_F	`g.sub.viscosityF`	$0.007 \cdot 10^{+6}$	$ng\mu m^{-1}s^{-1}$	[51]
Viscosity BM	μ_B	`g.sub.viscosityB`	$0.007 \cdot 10^{+6}$	$ng\mu m^{-1}s^{-1}$	Est. based on [51]
Viscosity ECF	μ_E	`g.sub.viscosityE`	$0.001 \cdot 10^{+6}$	$ng\mu m^{-1}s^{-1}$	[50]
Density fibrin	ρ_F	`g.sub.densityF`	$1.060 \cdot 10^{-3}$	$ng\mu m^{-3}$	-
Density BM	ρ_B	`g.sub.densityB`	$1.060 \cdot 10^{-3}$	$ng\mu m^{-3}$	-
Density ECF	ρ_E	`g.sub.densityE`	$0.9933 \cdot 10^{-3}$	μm	[50]

4.6. DATA VISUALIZATION

We developed a series of methods to visualize the data acquired by the time stepping scheme. We explain four types of plots in this section.

4.6.1. CHEMICAL SLICES PLOT

To visualize the chemical concentrations over our domain, we choose to plot the concentrations on slices[7].We fixate a point $P = \left(\frac{d_{top}}{2\xi}, \frac{d_{top}}{2\xi}, \frac{h_F}{\xi}\right)$. This point then lies in the middle of the disk of the initial cell distribution. We plot the chemical concentrations on three surfaces through this point P, each with one coordinate fixed. Underneath each slice plot, we plot a histogram of the concentrations of the given chemical on the nodes. The result for plotting the substrate fractions in the beginning of a simulation can be seen in Figure 4.5. Although this method of data visualization only gives information about the chemical concentrations on specific planes, it is insightful since it gives a view on the chemical process inside the problem domain.

4.6.2. CELLS PLOT

To visualize cell positions in 3D[8], we plot cells as spheres with radius R. We choose a camera angle from slightly below the horizontal $x-y$-plane so that we view the initial cell distribution from the bottom, as if we were looking through the fibrin scaffold. This allows us to see sprout formation since they move in a downward direction. We plot the edges of the computational domain as thick lines to help the viewer orient from the point of view we have. Optional, we can plot red and blue arrows from each cell in the direction of the haptotactic and chemotactic movement[9]. Stalk cells are plotted in green and stalk cells in red. Next to this plot, we plot smaller $x-y$, $z-y$ and $x-z$. The result is given in Figure 4.6.

---

[7] Setting `g.plot.plotType` = 4 plots the substrate components on slices. Setting `g.plot.plotType` = 5 plots the four chemical concentrations on slices.

[8] Setting `g.plot.plotType` = 3 plots the cells as spheres in 3D.

[9] The movement direction arrows can be plotted by setting `g.plot.quiverOn` = 1.

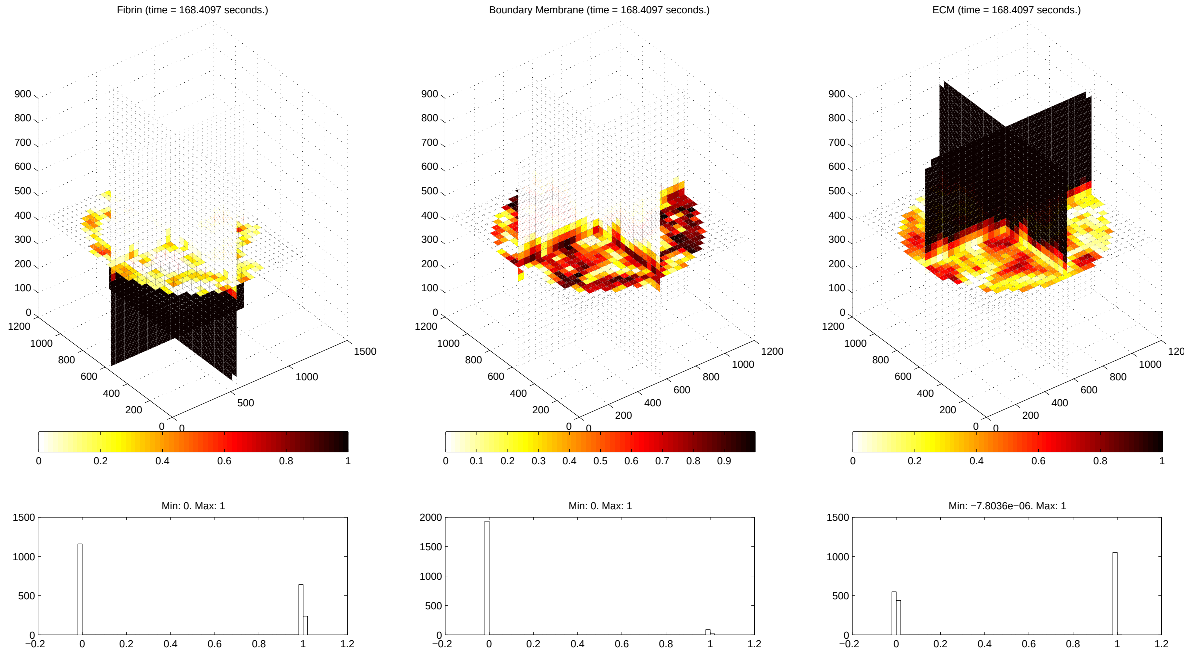

Figure 4.5: (almost) Initial condition plot for the substrate components using the slice plot.

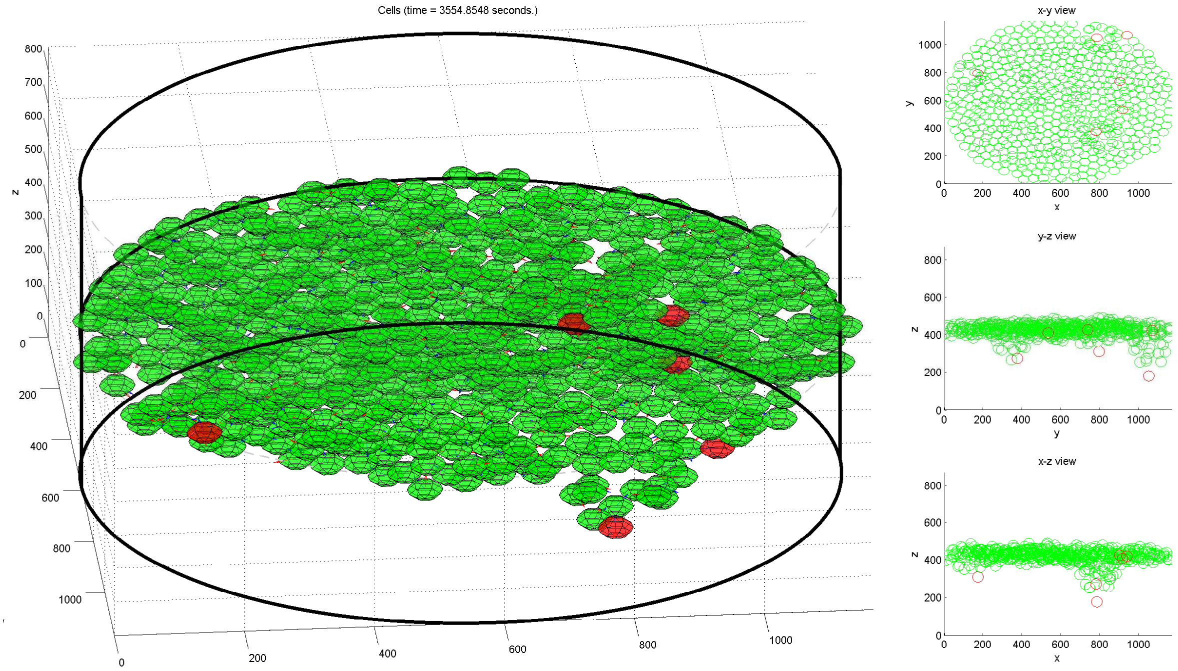

Figure 4.6: Cells plot. Tip cells are colored red. The thick black lines form the outline of the computational domain and aid the viewer in orienting the plot. The camera is in an angle slightly lower than the $x-y$-plane.

4.6.3. ISO-SURFACE PLOT

We are interested in the morphology of the $f_S = 0.5$ iso-surface because we model cells to adhere to this surface[10]. The 50 % substrate surface can be seen as the boundary between blood vessel and the ECM. For

---

[10] Setting `g.plot.plotType` = 11 plots the 50 % substrate iso-surface.

the same reasoning as in the cells plot, we choose a camera angle from slightly below the $x-y$-plane to be able to see sprout formation and we again plot the domain edges in thick lines to aid the viewer in orienting the plot. Also the smaller $x-y$, $z-y$ and $x-z$ views are plotted so we can keep track of the position of the tip cells. The result is given in Figure 4.8.

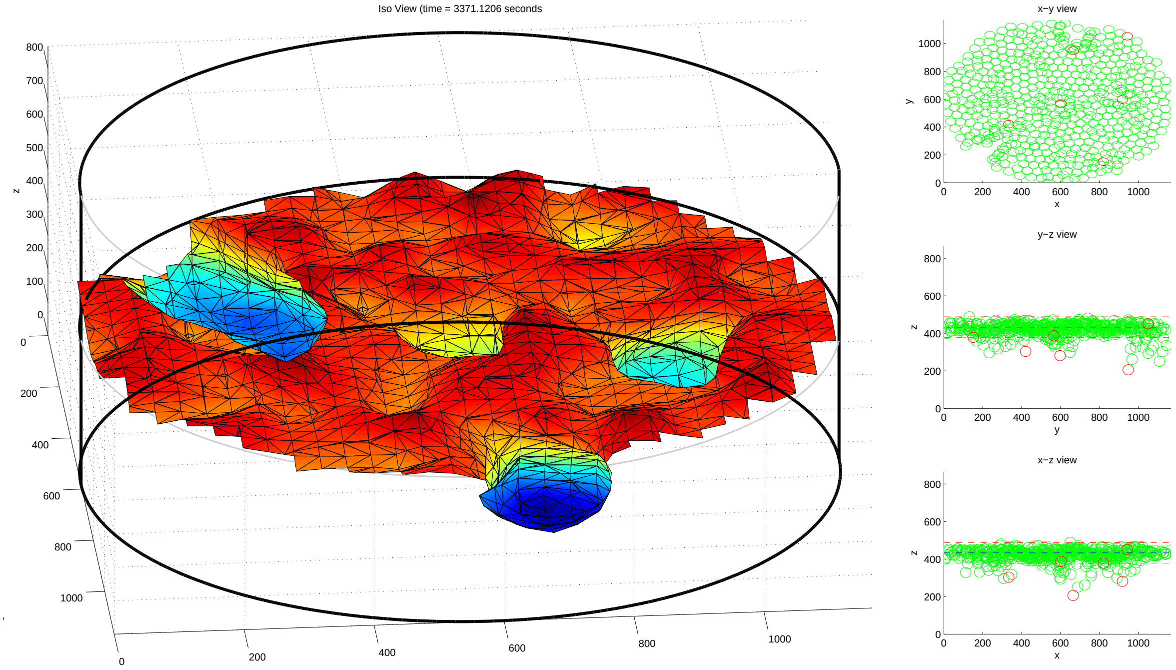

Figure 4.7: $f_S = 0.5$ Iso-surface plot. The thick black lines form the outline of the computational domain and aid the viewer in orienting the plot. The camera is in an angle slightly lower than the $x-y$-plane.

4.6.4. MICROSCOPIC PLOT

Finally, we are interested in comparing the microscopic photographs of the sprouting assay, like those in Figure 2.5 taken by the VU medical center dermatology department, to our simulation result[11]. We therefore plot our cells in the $x-y$ plane fixated at $z = h_F$. However, the microscopes used have a focal range of around $80\mu m$. We plot all cells q that have a z-coordinate $h_F - R \leq z_q \leq h_F + R$ in blue and denote these as *"mid level cells"*. Cells that are one layer higher, i.e. $h_F + R \leq z_q \leq h_F + 3R$, are denoted as the *"high level cells"* and are plotted in red. The layer beneath the mid level cells, i.e. $h_F - 3R \leq z_q \leq h_F - R$ are denoted as *"low level cells"* and are plotted in green. The radius of the plotted cells is given by the radius of the coupe of the cells at the three focal heights $h_F + 2R$ for the high level cells, h_F for the mid level cells and $h_F - 2R$ for the low level cells. High level cells that move downwards will then first decrease in radius before turning blue. Cells out of range of these three focal heights are not plotted in the main window since they are "out of focus". This leads to empty spaces at the locations of the sprouts. Note that cells with different colors are on different levels and can overlap in the $x-y$ view. Cells of the same color however are on the same height and will not overlap much thanks to the contact mechanics in the model.

In the microscopic photos we see the sprout perimeters as dark edges. We model our cells to adhere to the $f_S = 0.5$ iso-surface. We calculate the $f_S = 0.5$ iso-lines in the $x-y$ plane fixated at the height of the low level cells, i.e. $z = h_F - 2R$, and plot these. In practice, these lines positions agree with the sprout edges as seen on the photos. Tip cells are plotted as red crosses. A thick circle is drawn on the edges of the computational domain. Note that we have not modeled repulsive forces from the boundary and cells can move through this boundary. Alongside this main plot, we again plot the $x-y$, $z-y$ and $x-z$ views. in the $y-z$ and $x-z$ plots, we draw a red, a blue and a green line at the three different focal heights $z_F + 2R$, z_F and $z_F - 2R$.

---

[11] Setting `g.plot.plotType` = 10 plots the cells in the microscopic view.

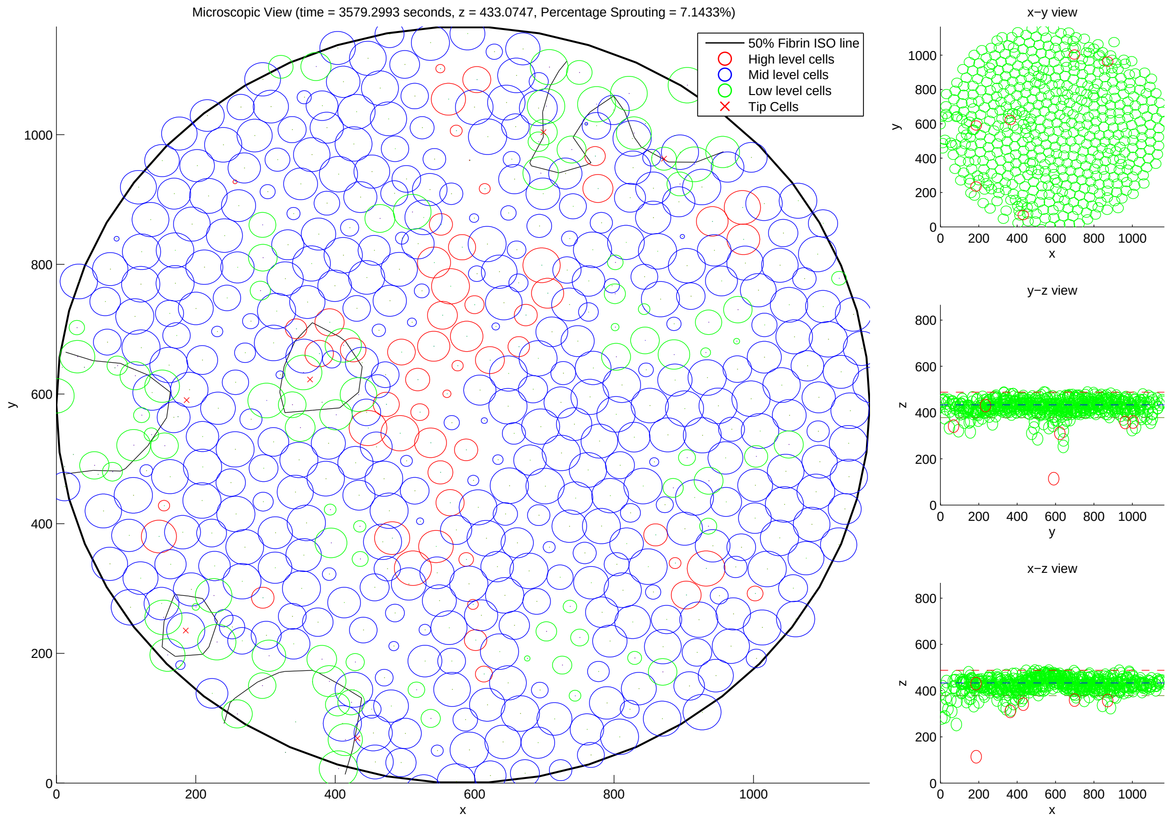

Figure 4.8: Microscopic plot.

4.7. INITIAL DISTRIBUTION CELLS

We need to impose an initial condition on the distribution of the cells. We propose a total of three different initial conditions and three test cases.

We know that the petri dish has diameter $\tilde{d}_{top}$ and we denote the radius by $\tilde{r}_{top}$. The fibrin scaffold has area $\tilde{A}_{top} = \pi \tilde{r}_{top}^2$. Therefore, the height of the top of the fibrin scaffold is equal to $\tilde{h}_F = \frac{\tilde{v}_F}{\tilde{A}_{top}} = 2598\mu m$. The height of the entire domain is $\tilde{h} = \frac{\tilde{v}}{\tilde{A}_{top}}$. We denote the cell radius by R. Since we describe a distribution over a cylindrical domain, we will use cylindrical coordinates $\mathbf{r}_i = (r, \theta, z)$ and we use the transformation to Cartesian coordinates $x = r\cos\theta, y = r\sin\theta, z = z$.

RANDOM MONOLAYER

The first option is placing the cell centers randomly[12] on the disc of radius $(\tilde{r}_{top} - R)$. We have to account for the fact that we have to place more cells at larger values of r to get an even distribution. We add a small perturbation with a standard deviation of magnitude $\frac{R}{5}$ to the height z. Let u_θ^i, u_r^i and u_z^i be random numbers drawn from a distribution $U(0,1)$ for each cell $i = 1, \ldots, N$. Then we define the initial location $\mathbf{r}_i$ of cell i by

$$\theta^i = 2\pi u_\theta^i, \qquad r^i = \sqrt{u_r^i (\tilde{r}_{top} - R)^2}, \qquad z^i = \tilde{h}_F + \frac{R}{5} u_z^i.$$

The advantage of this distribution is that it is stochastic, as can be expected from the physical process. However, cells can by chance overlap heavily, making the initial contact mechanical forces big in magnitude. This can produce erratic behavior in the first time step. An initial distribution formed using this mechanism is depicted in Figure 4.9.

---

[12] In our computational model, this option can be used by setting `g.cell0.randomLayer` = 1

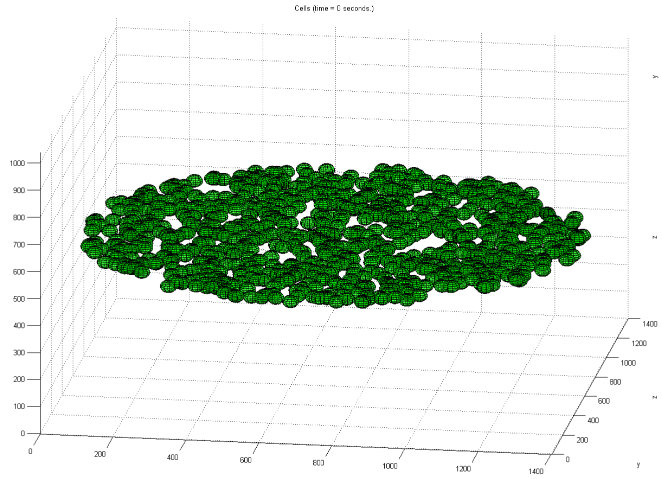

Figure 4.9: Random initial distribution of cells as produces using the option `g.cell0.randomLayer` = 1.

STRUCTURED MONOLAYER

To prevent the initial distribution of cells from having heavily overlapping cells, we implemented the option of placing cells in a monolayer in a structured way[13]. Consider cell numbers $i = 1, \ldots, N$. At each cell number, we both increment the radius r_i and the angle θ using

$$\theta^i = \pi\sqrt{2}i, \qquad r^i = (\tilde{r}_{top} - R)\sqrt{\frac{i}{N}}, \qquad z^i = \tilde{h}_F.$$

We do not add a perturbation to the height. Note that this produces a non-repetitive grid in angular symmetric sense thanks to the irrationality of the factor $\sqrt{2}$ in the increments of θ. The advantage of this distribution is that is does not have the erratic behavior that may occur in the random initial distribution. However, this pattern is not likely to immerse in biochemical applications. A structured initial condition produced by this mechanism is depicted in Figure 4.10.

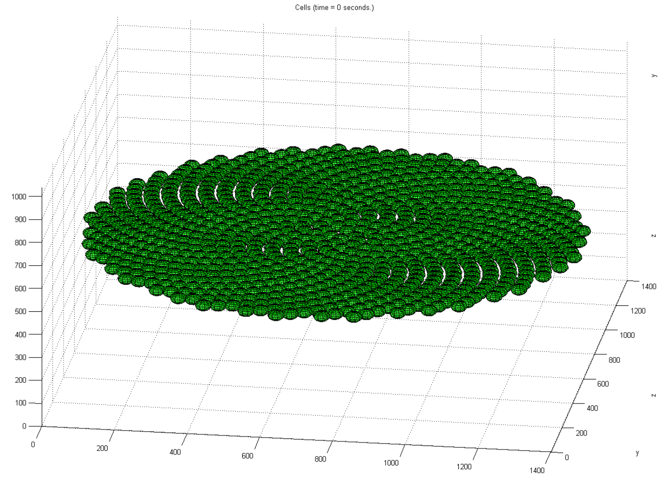

Figure 4.10: Structured initial monolayer distribution of cells as produced using the option `g.cell0.monoLayer` = 1.

DISPERSED CELLS

We know that in the sprouting assay, ECs are dispersed within the ECF that is poured on top of the fibrin scaffold. We assume that cells sink to the fibrin scaffold under the influence of gravity and that contact mechanics play a role in the formation of the monolayer like marbles poured out over a table top. Since we have both

---

[13] In our computational model, this option can be used by setting `g.cell0.monoLayer` = 1

implemented gravity and contact mechanics in our model, we can initially suspend cells in the ECF and see if a monolayer is formed[14]. We set r^i and θ^i in the same way as in the random layer. For the heights z^i, we pick a random value between the top of the domain $\tilde{h}$ and the top of the fibrin scaffold $\tilde{h}_F$, i.e.

$$\theta^i = 2\pi u_\theta^i, \qquad r^i = \sqrt{u_r^i (\tilde{r}_{top} - R)^2}, \qquad z^i = \tilde{h}_F + (\tilde{h} - \tilde{h}_F) u_z^i.$$

This initial condition seems to mimic the biochemical setting as close as possible and a generated distribution is depicted in Figure 4.11. Right after 5 minutes (300 seconds), we see the formation of a monolayer as depicted in Figure 4.12. We clearly see that cells do not all adhere to the fibrin scaffold at the same hight. This is to be expected since the top of the fibrin scaffold is somewhat uneven due to the fact that that the FEM mesh is unstructured.

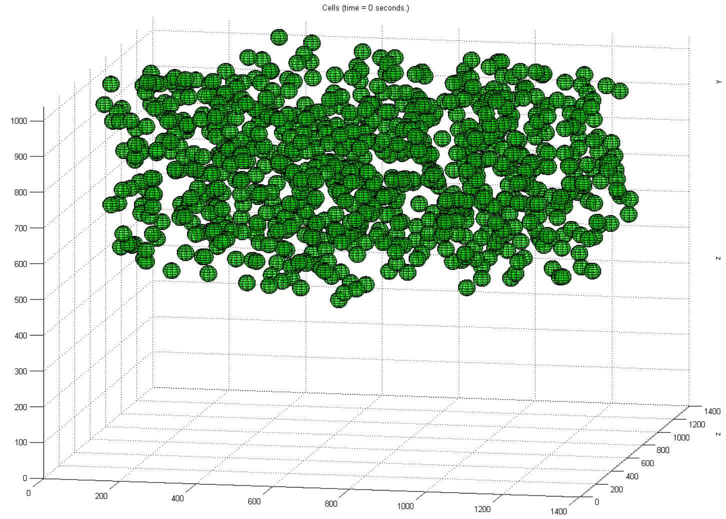

Figure 4.11: Suspended initial distribution of cells as produced using the option `g.cell0.suspended` = 1.

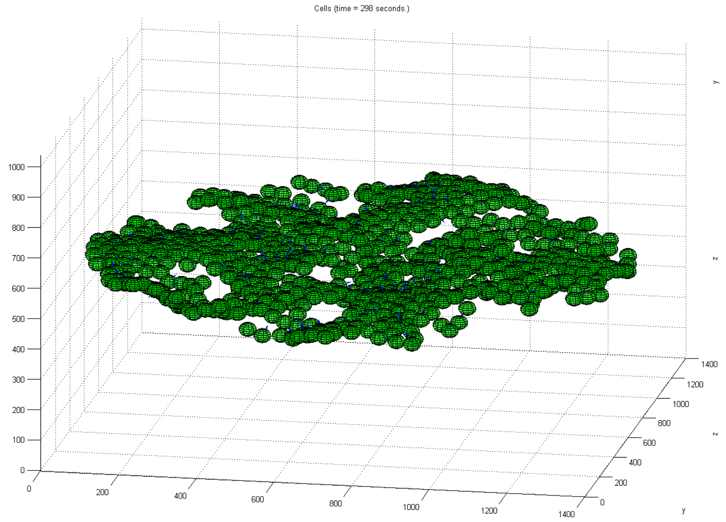

Figure 4.12: Formed monolayer after 598 seconds using a suspended initial cell distribution.

TEST CASES

For testing and development purposes, we have implemented initial conditions with only two, four or eight cells. These distributions can be used by setting the parameters `g.cell0.twoCells`, `g.cell0.fourCells` or `g.cell0.eightCells` to 1. We chose to leave these options in the model for future developers.

---

[14] In our computational model, this option can be used by setting `g.cell0.suspended` = 1

5

RESULTS

In this chapter, we present the results of the model simulations. We start with a brief summary of the mechanics of our model, for both the chemicals and the cell movement. We then introduce metrics to monitor the "amount of sprouting" and analyze the variance of the metrics for the model outcome. A sensitivity analysis is performed to quantify the response of the model in terms of the introduced metrics to variation in the model parameters as formulated in the previous chapter. We conclude by comparing our model outcomes to the work done by the VU medical center dermatology department and by mentioning the relation between matrix elasticity and vasculogenesis-like pattern formation.

For every model simulation, we produced a video file containing a combination of the cells plot, the microscopic plot, the iso-surface plot and the $x-y$, $y-z$ and $x-z$ plots. These video files are submitted digitally together with this thesis. Along with the video files, we store data files containing all the time series of the proposed metrics and a file containing the parameters used in each specific simulation.

5.1. MODEL MECHANICS

We model our chemicals using reaction-diffusion-sourcing equations and we numerically solve the solutions using the FEM scheme as derived in Appendix C. Concentrations DLL4, uPA and MMP source at the locations of the tip cell centers and then diffuse into their surroundings. uPA and MMP react with the substrate components and their concentrations will decrease. The initial VEGF distribution will diffuse from the substrate into the ECF. We show all these effects after one hour of simulated time using a slice plots in Figure 5.1. We tested diffusion, reaction and sourcing separately[1] and the results are as one would expect.

We model the cell movement using haptotaxis, contact mechanics, chemotaxis, adhesion and diffusion. We expect from the contact mechanics that cells will not overlap to a large extent. The haptotactic movement will cluster cells together. Chemotaxis will cause stalk cells to move towards the tip cells sourcing the chemoattractant DLL4. Finally, adhesion will cause cells to adhere to the $f_S = 0.5$ iso-surface. Since our initial substrate is not perfectly flat due to the initial condition for the substrate components on the nodes as described in Equation 4.8, we expect to see cells taking higher or lower positions locally based on the substrate conditions. We put all these expectations for the cell movement to the test using a simulation with an initial random layer of cells, allowing cells to overlap initially. We plot the microscopic view for the fixed moments $t = 47s$, $t = 106s$, $t = 286s$, $t = 446s$, $t = 1066s$ and $t = 2206s$. The results are given in Figures 5.2 to 5.7.

We see that initially all cells are on the "mid level" (i.e. blue) and they do overlap and leave some space empty. Initially, the contact mechanics are predominant and we see large cell overlaps disappear quickly. With smaller cell overlaps, contact mechanical forces decrease and the adhesive forces become dominant. Cells are pushed or pulled towards the $f_S = 0.5$ iso-surface and we witness height differences appear in the form of cells moving to different levels (colors). As each cell is at the level of the 50 % substrate density, adhesive forces decrease and finally haptotactic forces grow relatively dominant. We see that holes in the

---

[1] Diffusion can be turned off by setting `g.chem0.diffusionOn` = 0. Reaction can be turned off by setting `g.chem0.reactionOn` = 0. Sourcing can be turned off by setting `g.chem0.sourcingOn` = 0.

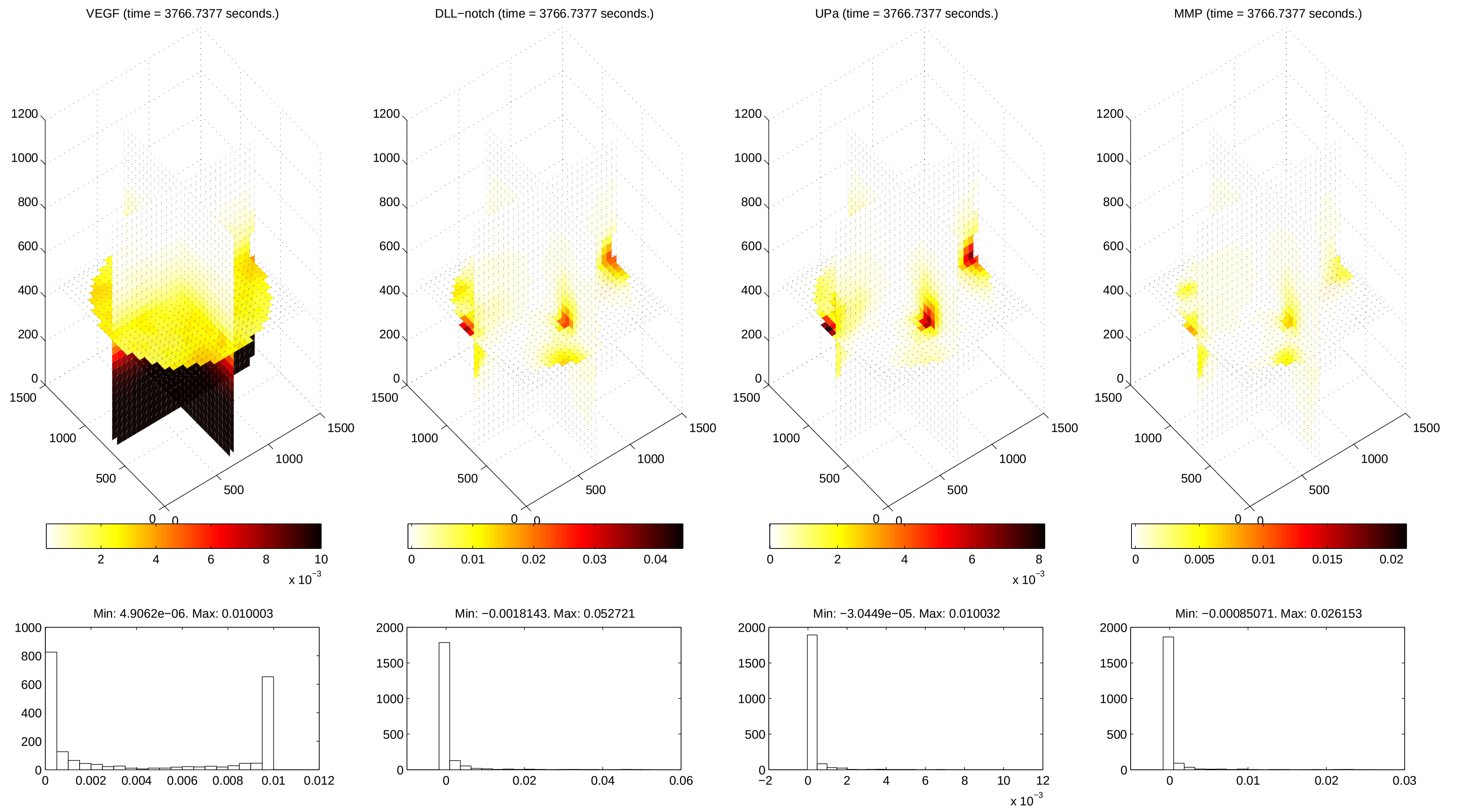

Figure 5.1: The chemicals over time in slice plots following the time dependent reaction-diffusion-sourcing equations. We see diffusion of the initial VEGF distribution. We see sourcing of the other three chemicals at the locations of tip cells and diffusion into the surroundings. MMP and uPA react at a faster rate than DLL4 due to the abundant presence of the substrate components. This figure is taken after approximately one hour of simulated time.

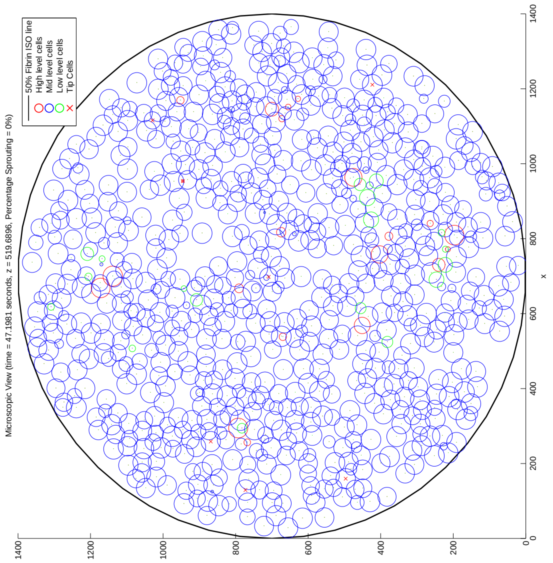

Figure 5.2: Cell locations at $t = 47s$.

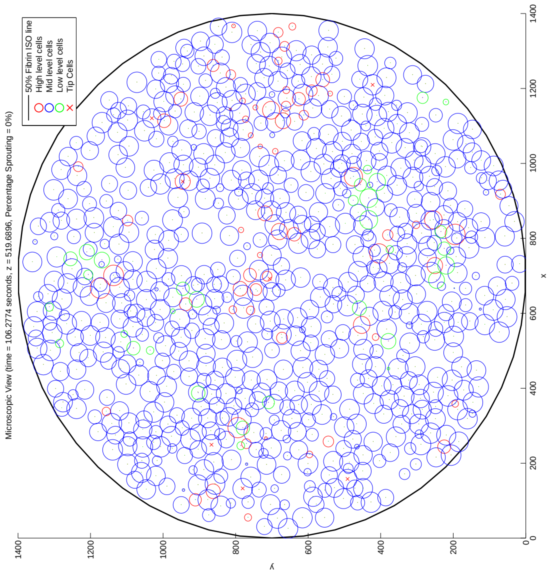

Figure 5.3: Cell locations at $t = 106s$.

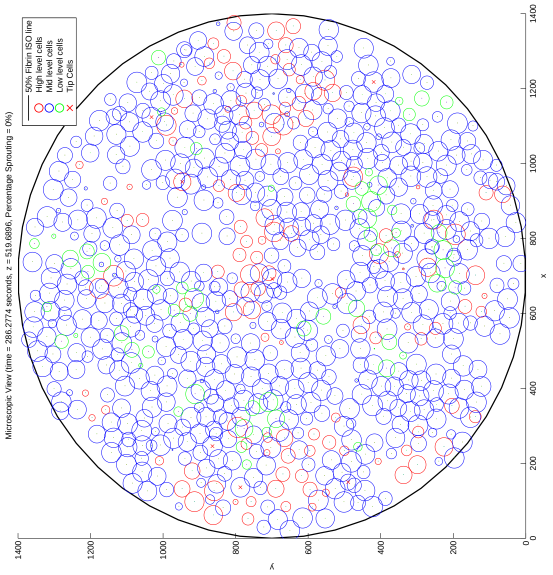

Figure 5.4: Cell locations at $t = 286s$.

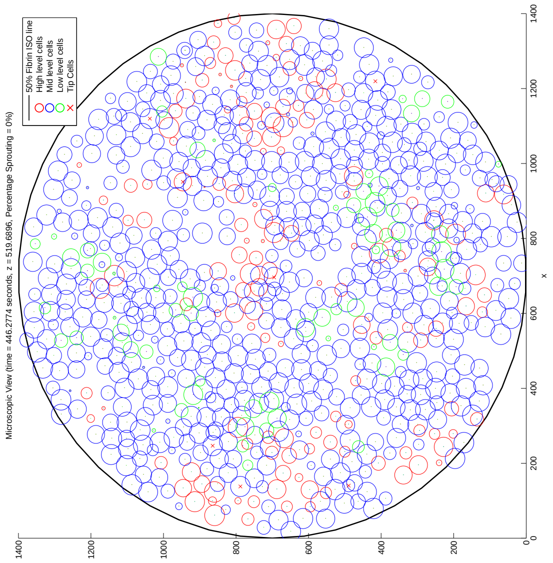

Figure 5.5: Cell locations at $t = 446s$.

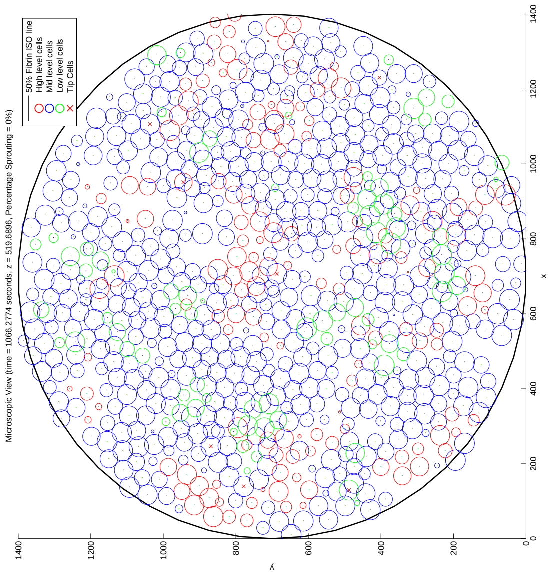

Figure 5.6: Cell locations at $t = 1066s$.

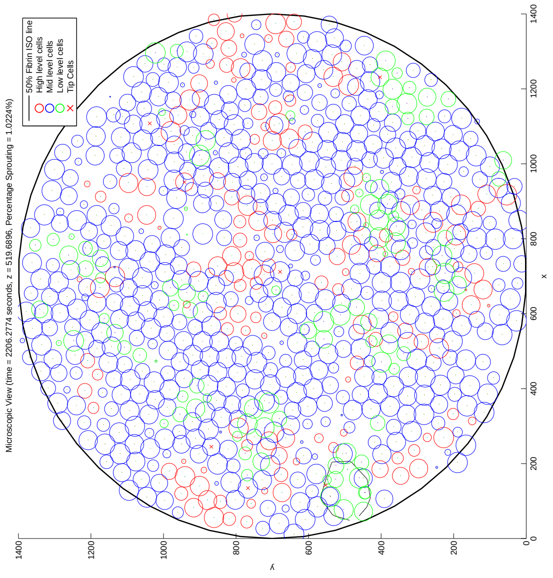

Figure 5.7: Cell locations at $t = 2206s$.

monolayer are filled up with cells to reach the final distribution of cells. We even see a newly formed sprout appear in Figure 5.7. All moments in time in the plots in Figures 5.2 to 5.7 are in a too early stage to really witness the chemotactic movement. Gravity does not play a role since the cells already lie on the matrix. We have tested all the cell movement effect separately[2] and the results are as one would expect.

5.2. METRICS FOR THE AMOUNT OF SPROUTING

In order to compare the model outcomes for different sets of parameters, we propose eight metrics that give an indication of the “amount of sprouting”. During a simulation, we keep track of the number of tip cells $n_t(t)$ over time and we denote individual tip cells by $q \in \theta_t$. For each tip cell q we keep track of its z-coordinate over time $z_q(t)$ as a measure of sprout depth. The time derivative of this metric $\frac{dz_q}{dt}$ for each tip cell q gives the speed at which sprouts are moving downwards. It is insightful to calculate the average sprout depth $\bar{z}(t)$ and the average sprout speed $\frac{d\bar{z}}{dt}(t)$ given all sprouts in one simulation.

Some tip cells will not form a sprout and some sprouts are led by more than one tip cell and we keep track of the number of sprouts $n_s(t)$ in the domain separately. The ratio $\frac{n_s}{n_t}(t)$ gives the percentage of tip cells that succeeded in forming a sprout. We say that we have an isolated sprout whenever we have a closed $f_S = 0.5$ iso-line directly beneath the surface of the initial cell distribution at $z = h_F - 2R$ with outwards directed gradient. Figure 5.8 shows a situation with a total of 8 sprouts delineated by the black $f_S = 0.5$ iso-lines. We denote the total area within the iso-lines as a percentage of the total area $A(t)$. The perimeters of the sprouts on the microscopic photos in Figure 2.5 have an approximate width of one cell radius. We multiply the combined length of the iso-lines by the cell radius R and calculate this as a percentage of the total area to get metric $P(t)$. This metric closely resembles the measured value in the sprouting assay. Finally, we keep track of the total mass-percentage of the initial substrate that has degraded into ECF using the metric $V(t)$ (V for “vasculature”).

We choose to plot the metrics $n_t(t)$, $n_s(t)$ and $\frac{n_s}{n_t}(t)$ together since they provide insight in how many cells sense the chemical stimulus to start forming new vasculature and how successful they are in this process. The three metrics $A(t)$, $P(t)$ and $V(t)$ are comparable since they all give insight in the magnitude of the total formed vascularization and we choose to plot these together. We plot the two metrics $\bar{z}(t)$ and $\frac{d\bar{z}}{dt}(t)$ together since they give insight in the dynamics of the sprout fronts. An overview of the metrics and their dimensions is given in Table 5.1. The metrics $n_t(t)$, $V(t)$, $\bar{z}(t)$ and $\frac{d\bar{z}}{dt}(t)$ are known at each time step. The values for $n_s(t)$, $\frac{n_s}{n_t}(t)$, $A(t)$ and $P(t)$ however are calculated only whenever we plot a frame to reduce computational load. In order to compute the value of these metrics, we have to calculate the iso-lines in the cells plot, which is computationally expensive. We choose to produce movie files with a duration of 45 seconds at 24 frames per second. For four hours of simulated time, this entails one frame every 13.3 seconds of simulated time whereas the variable time stepping scheme can choose to do much smaller time steps.

5.3. ESTIMATORS FOR THE MEAN OF THE METRICS

Now we have defined metrics to measure the “amount of sprouting”, we can analyze the model outcome. Since we know that there is a stochastic factor in both the cell movement and in the tip cell selection, we expect slightly different outcomes for different simulations. Using the parameters given in Tables 4.2, 4.3 and 4.4 we simulated 12 sprouting assays. Since the total time for one simulation can exceed 24 hours for a very fine grid with small time steps, we simulate multiple runs simultaneously. The Department of Precision and Microsystems Engineering of the Delft University of Technology was so kind to give us computational time on their cluster computer. Figures 5.10, 5.11 and 5.12 give the sprouting metrics over time for each simulation. Figures 5.13, 5.14 and 5.15 give the estimator for the mean of all metrics and a 95% confidence interval based on the average over these simulations under the normality assumption. We conclude that using the standard parameters, we see that after 4 hours of simulated time (i.e. 14400 seconds), the 95% confidence intervals for the mean of the metrics are as given in Table 5.1.

It should be noted that we calculated the speed of the sprouts $\frac{d\bar{z}}{dt}(t)$ using a first order approximation $\frac{d\bar{z}}{dt}(t) \approx$

---

[2] Haptotaxis and contact mechanics together can be turned off by setting `g.cell0.haptotaxisOn` = 0. Chemotaxis can be turned off by setting `g.cell0.chemotaxisOn` = 0. Adhesion can be turned off by setting `g.cell0.adhesionOn` = 0. Gravity can be turned off by setting `g.cell0.gravityOn` = 0.

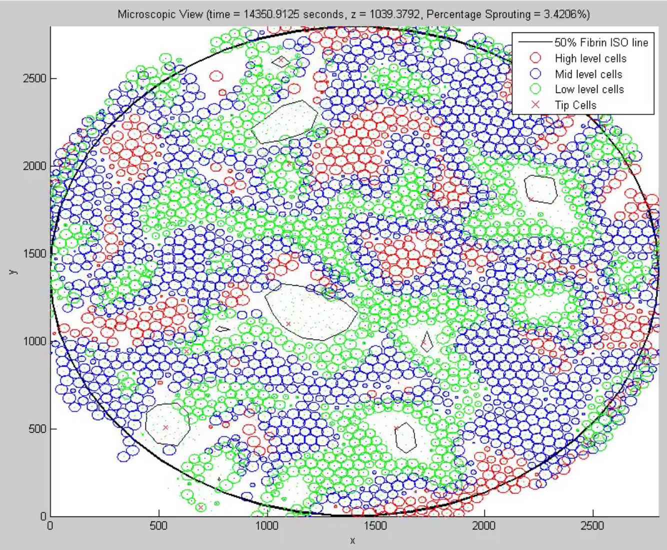

Figure 5.8: We see a total of $n_s = 8$ sprouts of different sizes in order of decreasing area at locations approximately $(x, y) = (1250, 1200), (1100, 2200), (550, 550), (2200, 1900), (1700, 500), (1800, 1000), (1000, 2500)$ and $(1300, 1100)$. We also see tip cells (denoted by red x-marking) that have not formed a sprout. The iso-lines are calculated in the surface at $z = 1039.4$ directly beneath the initial placement of the cells. The total number of tip cells is $n_t = 9$.

$\frac{\bar{z}^{d+1}-\bar{z}^{k}}{\Delta t^{k}}$. Since we use a predictor-corrector scheme for the cell movement, the numerical error on $\bar{z}$ is of order $\mathcal{O}(\Delta t^2)$. The first order approximation of $\frac{d\bar{z}}{dt}(t)$ makes the estimation of order $\mathcal{O}(\Delta t)$. The accuracy of the sprout speed should therefore be treated with a certain caution.

We witness a jump in the value of $A(t)$ and $P(t)$ for a certain simulation (light green line in Figure 5.11) at $t = 14000$. Looking in the video file of this specific simulation, we see that two sprout perimeters merge, but their surfaces do not connect. Apparently both the these perimeters ands areas are counted twice. The "half merged sprouts" are depicted in Figure 5.9. We have not encountered this problem anywhere else.

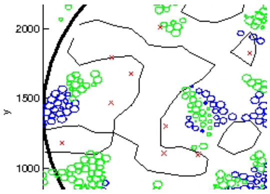

Figure 5.9: Only half merged sprouts, leading to an overshoot in the values of $A(t)$ and $P(t)$.

Metric	**Metric for**	**Symbol**	**Dimension**	**95% confidence int. for the mean**
Number of tip cells	Sensed angiogenic urge	$n_t(t)$	-	22 ± 2.6
Number of sprouts	Sensed angiogenic urge	$n_s(t)$	-	12.8 ± 1.7
Successfulness of tip cells	Sensed angiogenic urge	$\frac{n_s}{n_t}(t)$	-	0.58 ± 0.054
Sprouted area at $z = h_F$	Vascular construction	$A(t)$	-	0.145 ± 0.027
Sprouted perimeter at $z = h_F$	Vascular construction	$P(t)$	-	0.051 ± 0.0067
Degraded substrate	Vascular construction	$V(t)$	-	0.066 ± 0.011
Average depth tip cells (sprouts)	Sprout dynamics	$\bar{z}(t)$	μm	593 ± 46
Average speed tip cells (sprouts)	Sprout dynamics	$\frac{d\bar{z}}{dt}$	$\mu m s^{-1}$	0.053 ± 0.0098

Table 5.1: Overview of the eight metrics for the "amount of sprouting" together with the 95% confidence intervals of the estimators for their mean values.

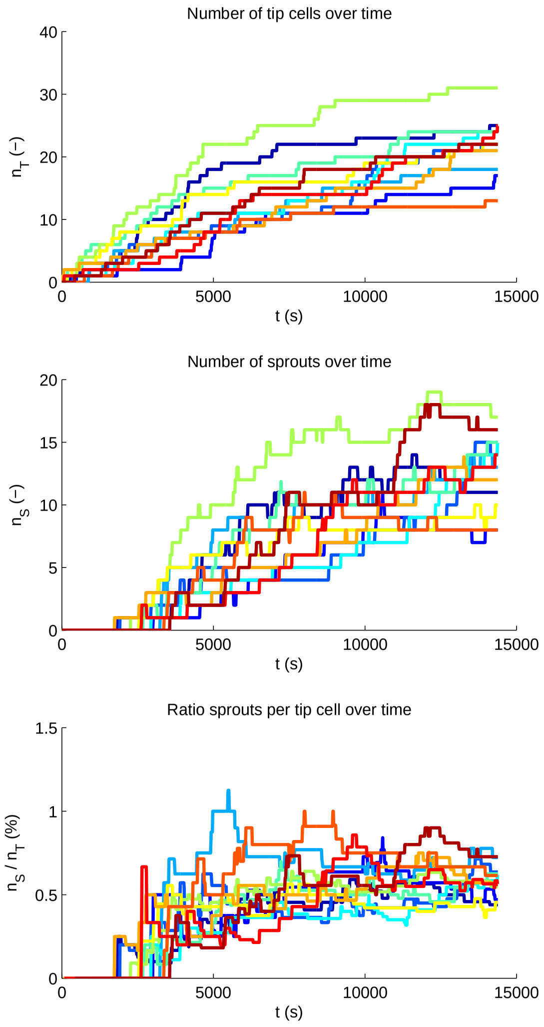

Figure 5.10: The number of tip cells n_t, the number of sprouts n_s and the ratio of sprouting success $\frac{n_s}{n_t}$ for 12 identical parameter model simulations.

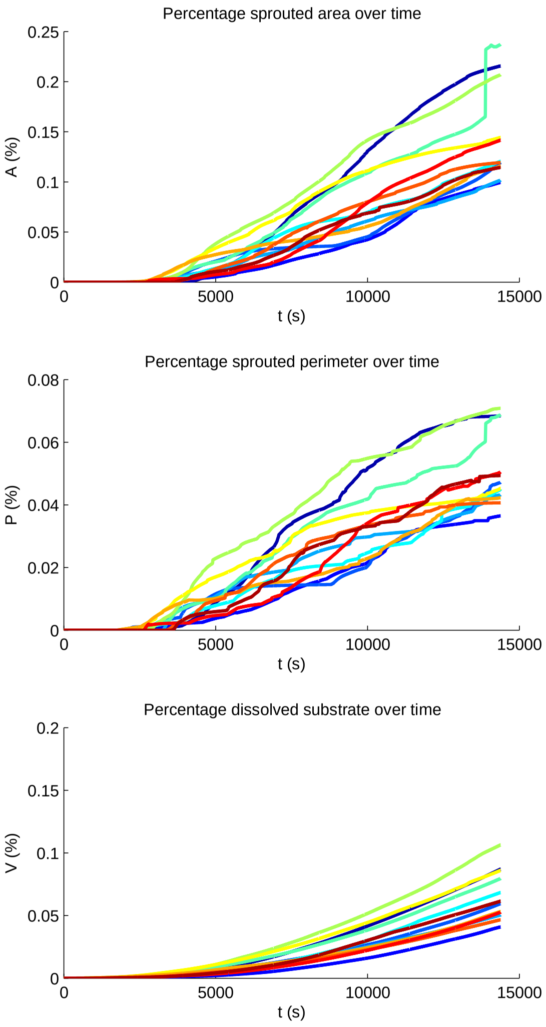

Figure 5.11: The area A and perimeter P of all sprouts at h_F as a percentage of the total area and the percentage degraded substrate V for 12 identical parameter model simulations.

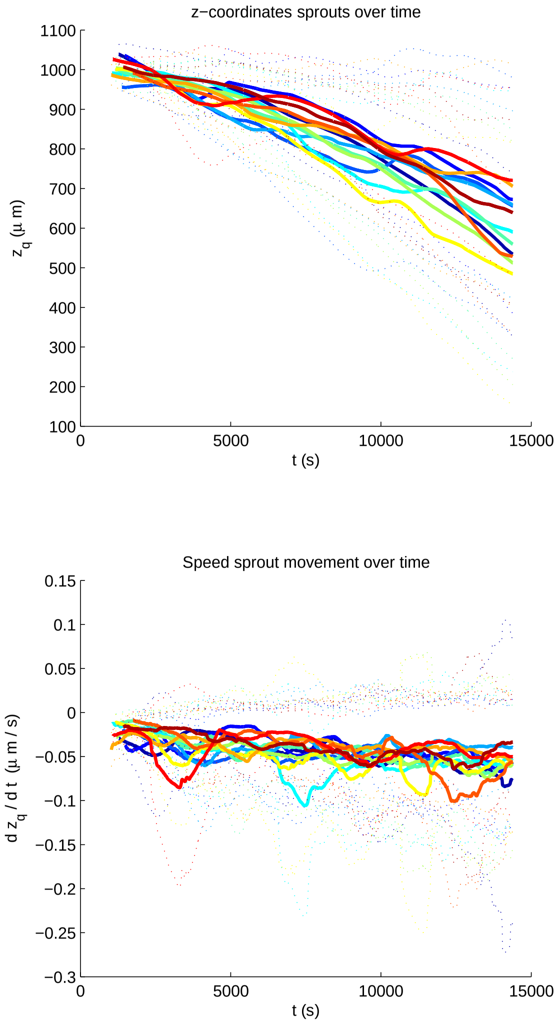

Figure 5.12: The average z-coordinate $\bar{z}$ and the average speed $\frac{d\bar{z}}{dt}$ of all cells in a simulation for 12 identical parameter model simulations.

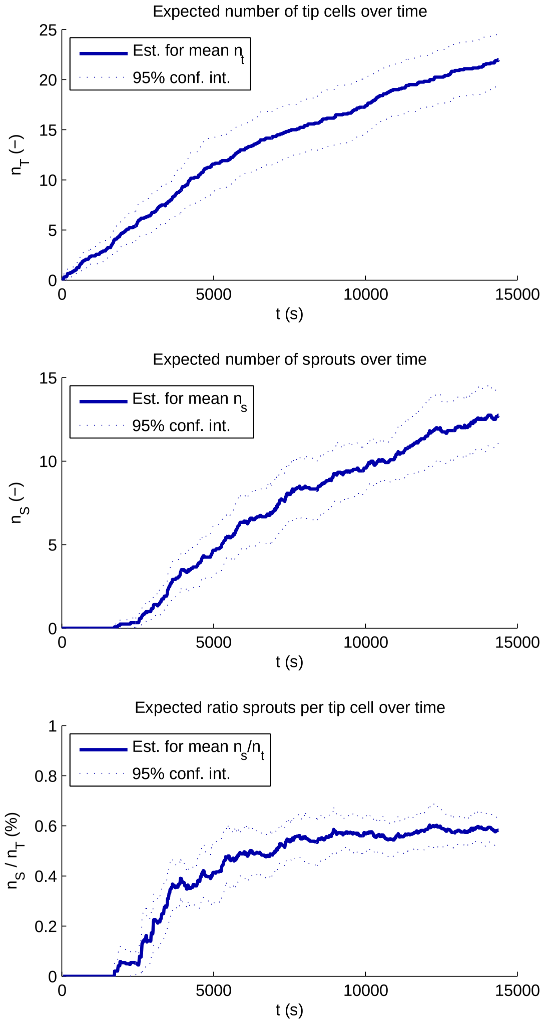

Figure 5.13: The estimators for the mean number of tip cells n_t, sprouts n_s and ratio of sprouting success $\frac{n_s}{n_t}$ and 95% confidence intervals based on 12 simulations.

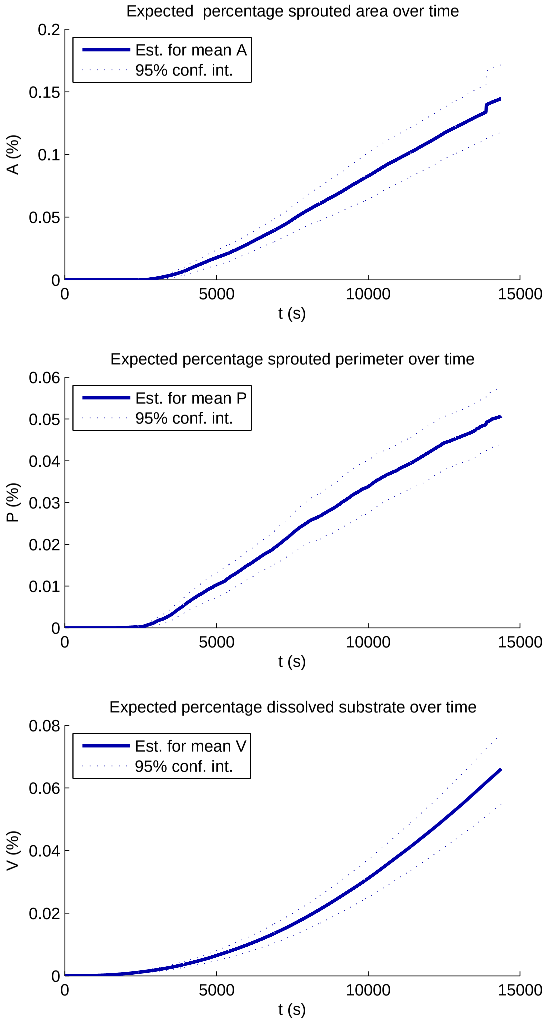

Figure 5.14: The estimators for the mean area A and perimeter P of all sprouts at h_F as a percentage of the total area and the percentage degraded substrate V and 95% confidence intervals based on 12 simulations.

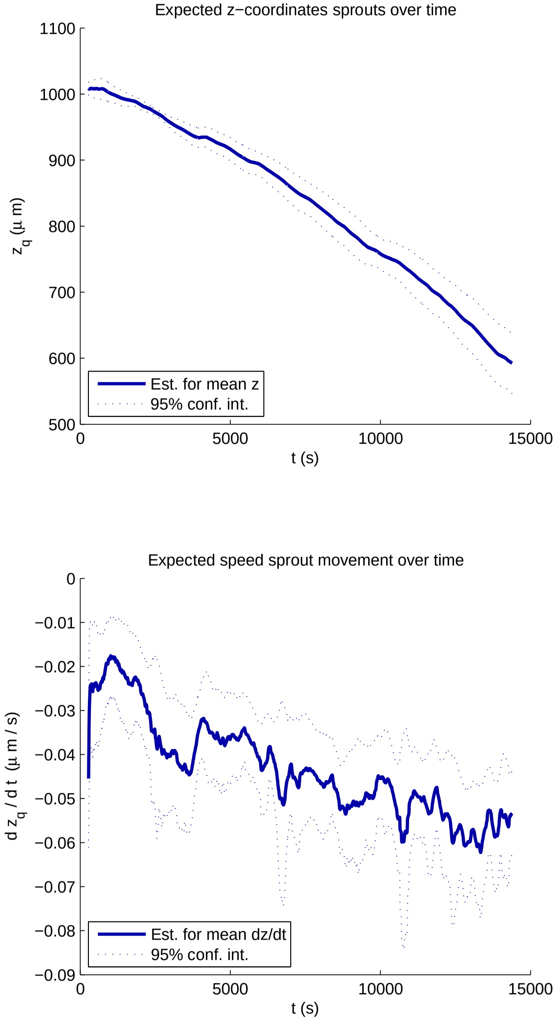

Figure 5.15: The estimators for the mean average z-coordinate $\bar{z}$ and average speed $\frac{d\bar{z}}{dt}$ and 95% confidence intervals based on 12 simulations.

5.4. SENSITIVITY ANALYSIS

We want to test the response of the model to variation of the parameters listed in Tables 4.2, 4.3 and 4.4. We choose a total of five parameters to vary, which are the initial concentration VEGF c_V^0, the sourcing rates of the substrate degrading proteases s_U and s_M, the maximal rate of tip cell selection per second p_{ST}, the scaling factor for the adhesive force $\hat{\lambda}$ and the elasticity of the substrate E_F.

For each sensitivity analysis, we do five model simulations with different values of one of these specific parameters, keeping all other parameters constant at the values given in Tables 4.2, 4.3 and 4.4. For the varying parameter, we choose the standard value, a half and a quarter the standard value and twice and four times the standard value. We formulate a prediction based on the influence diagram we based our model on in Figure 4.1 and discuss the results for each parameter variation.

5.4.1. VARYING THE INITIAL CONCENTRATION VEGF c_V^0

We are interested in the model response to varying initial conditions VEGF c_V^0 because we model this substance as the driver of the chemotactic movement, the tip cell selection and the protease secretion. In our influence diagram, the amount of secreted proteases is dependent on both the VEGF concentration itself as well as on the number of tip cells $n_t(t)$, which on its turn is up-regulated by VEGF. We therefore expect a rapid increase in the substrate degrading, measured by the metrics $A(t)$, $P(t)$ and $V(t)$. The increased chemotactic movement should increase both the sprout depth $\bar{z}(t)$ and the sprout speed $\frac{d\bar{z}}{dt}(t)$.

Figures 5.16, 5.17 and 5.18 give the results of the variation of the initial VEGF concentration c_V^0. We indeed see large differences in the values of $A(t)$, $P(t)$, $V(t)$, $\bar{z}(t)$ and $\frac{d\bar{z}}{dt}(t)$ that exceed the random fluctuations given in Table 5.1. However, tip cell selection is not influenced by the variation of the VEGF concentration. This is due to the fact that in the probabilistic rate of tip cell selection in Equation 4.15, we scale the VEGF concentration by it's initial value. This assumption in the probabilistic model may be reconsidered to improve the model.

It is notable that for both metrics $A(t)$ and $P(t)$ we see that the high concentration produces larger values than the very high concentration. In the video files we see that for the very high concentration, the tip cells move downwards so quickly that they degrade the matrix at the top level for a smaller length of time, decreasing the values of $A(t)$ and $P(t)$. Very high values of c_V^0 will indeed induce more secretion of proteases and hence over all cause more substrate degrading $V(t)$. Sprout morphology for the very high concentration is more tube shaped, whereas for other concentrations, we see more conical shaped sprouts with larger perimeters at the top level. It is interesting to note that for the *in vitro* experiment by the VU medical center dermatology department, we see the same pattern in the assay with bFGF.

5.4.2. VARYING THE PROTEASE SOURCING RATES s_U AND s_M

We are interested in the model response to varying sourcing rates s_U and s_M because we expect protease induced degrading of the substrate to drive sprout morphology. From the influence diagram we expect that increased protease secretion will increase substrate degrading and increase all parameters $A(t)$, $P(t)$ and $V(t)$. This on its turn could increase sprout movement metrics $\bar{z}(t)$ and $\frac{d\bar{z}}{dt}(t)$ since cells are more free to move. Since we have seen that increasing the VEGF concentration does not increase the number of tip cells, we expect similar results.

Figures 5.19, 5.20 and 5.21 give the results to the variation of the secretion parameters. We indeed see a similar result as the variation of the VEGF concentration. All metrics $A(t)$, $P(t)$, $V(t)$, $\bar{z}(t)$ and $\frac{d\bar{z}}{dt}(t)$ increase with increasing protease secretion.

It is interesting to note that we also see an increased success rate $\frac{n_s}{n_t}(t)$. We postulate that it is the tip cell's ability to degrade the substrate that drives its probability of producing a viable sprout over the chemotactic response to a higher concentration VEGF. Sprouts are even faster and reach deeper for increasing protease secretion then for increasing VEGF concentration. Apparently, the increased chemotactic forces induces by higher concentrations VEGF do not translate into more sprout movement whenever a tip cell does not have the ability to degrade the substrate underneath itself sufficiently.

5.4.3. VARYING THE MAXIMAL RATE OF TIP CELL SELECTION p_{ST}

We are interested in the model response to varying maximal rates p_{ST} in the probabilistic process of tip cell selection. Tip cells lead the sprout formation and we are interested to see if more tip cells will produce more sprouts or if a growing number of tip cells will be at the expense of the success rate. We have seen that it is the protease secretion that mediates the sprout speed and we therefore do not expect raised values for $\frac{d\bar{z}}{dt}(t)$. An larger number of tip cells does increase the total secretion of proteases and we therefore expect to see increased values for $A(t), P(t)$ and $V(t)$.

Figures 5.22, 5.23 and 5.24 give the results for the variation of the maximal tip cell selection rate. We indeed see a larger number of tip cells appear for higher values of p_{ST}. More tip cells do produce more sprouts n_s, but we have to note that the success rates $\frac{n_s}{n_t}(t)$ do not seem to be influenced by the maximal probability. As expected, we witness increased values for $A(t), P(t)$ and $V(t)$.

We see that the speed of sprout movement is not influenced as much as when we varied the VEGF concentration and the protease secretion rates. We do see that more tip cells are selected early in the process for higher selection rates p_{ST} and this gives formed sprouts more time to reach further, resulting in higher values of $\bar{z}(t)$. This observation backs our conjecture that sprout speed is dominantly mediated through protease secretion. It is interesting to see that for very high values of p_{ST}, tip cell selection stagnates after 10.000 seconds to a total of 50 tip cells. This entails that 1.6 % of the ECs are tip cells. The stagnation can be explained by the inhibition of the selection process due to the raised DLL4 concentration. For low values of P_{ST} we do not witness this stagnation.

5.4.4. VARYING THE ADHESIVE SCALING CONSTANT $\hat{\lambda}$

We are interested in the model variations for varying values of the adhesive strength scaling parameter $\hat{\lambda}$ because this parameter has a non-physical nature and must therefore be specifically tested for model influence. We expect that stronger adhesion will influence the contiguity of the monolayer but not directly influence one of the measured metrics.

Figures 5.25, 5.26 and 5.27 give the results for variation of $\hat{\lambda}$. We indeed see that variations do not influence any of the metrics in a coherent manner. Variations between the simulations are not ordered according to the size of the variations and they are within the range of the variance we expect from the stochastic nature of the model itself. This observation is beneficial for the validation of our model since the uncertain parameter $\hat{\lambda}$ apparently does not have a big influence on the process that we try to model.

However, we do see in the video files that for high adhesive values, the cells adhere to the substrate more strongly in comparison to the other forces involved and we witness the confluent monolayer of cells breaking apart. We therefore hold on to the value for $\hat{\lambda}$ as chosen in Table 4.3.

5.4.5. VARYING THE ELASTICITY OF THE SUBSTRATE E_F

We are interested in the model variations for varying substrate elasticities. We have previously modeled that $E_B = 2E_F$, so when we increase E_F, we will increase E_B accordingly. We know that Namy et al. [18] find that substrate elasticity is an important factor in EC pattern formation on *in vitro* substrates. We are interested to see if our model verifies this result.

Figures 5.28, 5.29 and 5.30 give the results for variation of E_F. We directly conclude that none of the metrics for angiogenesis as proposed are influenced by this variation. However, looking at the video files, we see very interesting differences in pattern formation on the substrate surface and we devote the subsequent chapter to this phenomenon.

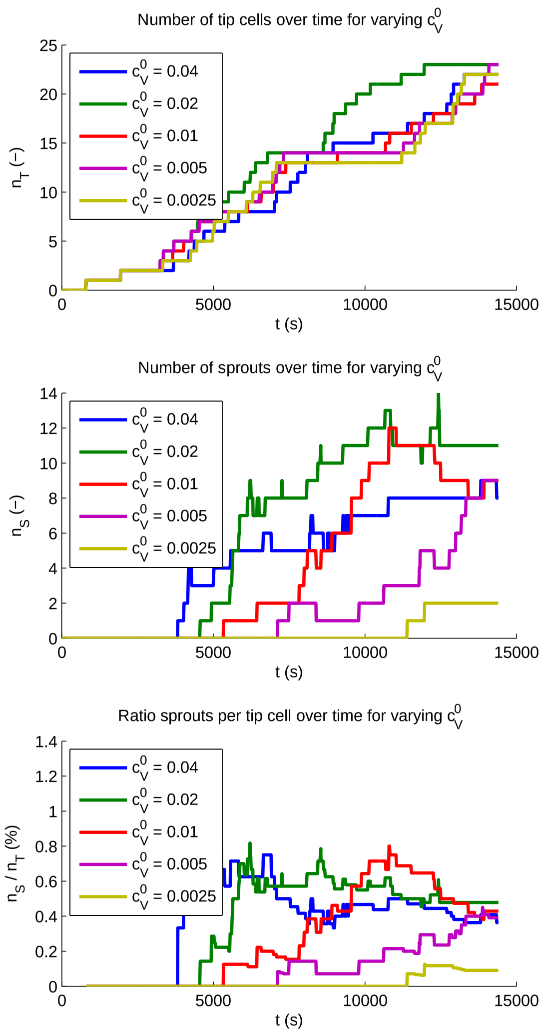

Figure 5.16: The number of tip cells n_t, the number of sprouts n_s and the ratio of sprouting success $\frac{n_s}{n_t}$ for varying initial concentrations VEGF.

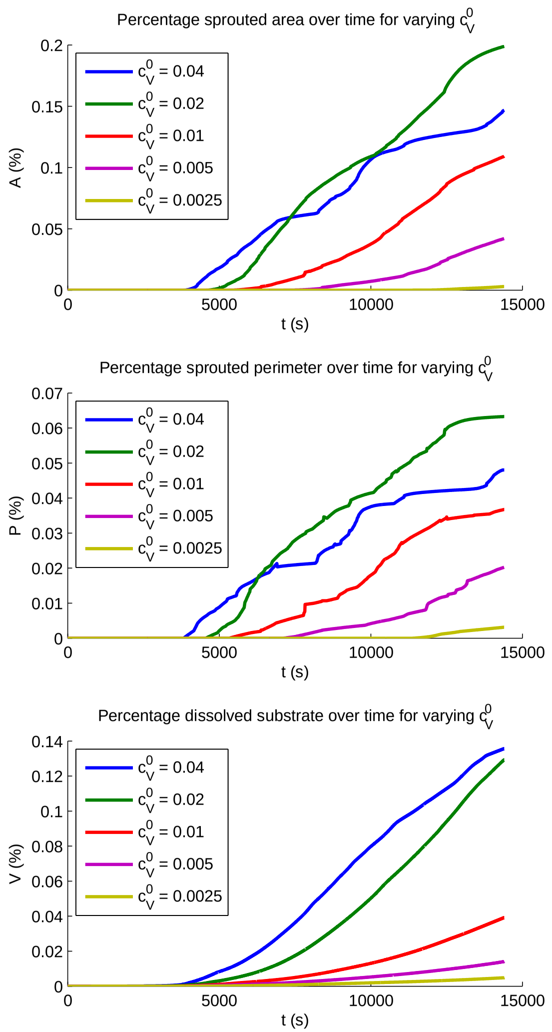

Figure 5.17: The area A and perimeter P of all sprouts at h_F as a percentage of the total area and the percentage degraded substrate V for varying initial concentrations VEGF.

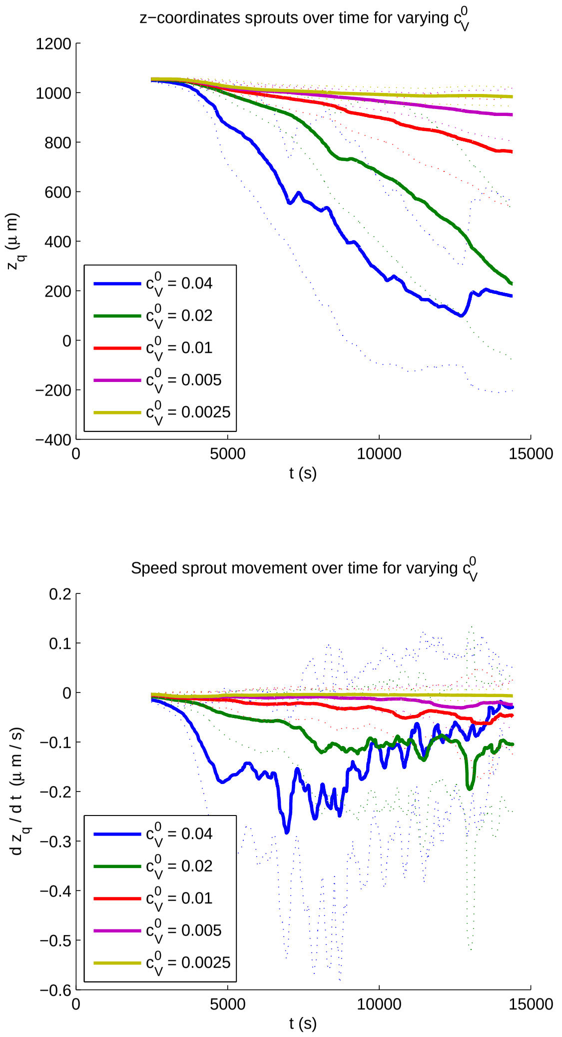

Figure 5.18: The average z-coordinate $\bar{z}$ and the average speed $\frac{d\bar{z}}{dt}$ of all cells in a simulation for varying initial concentrations VEGF.

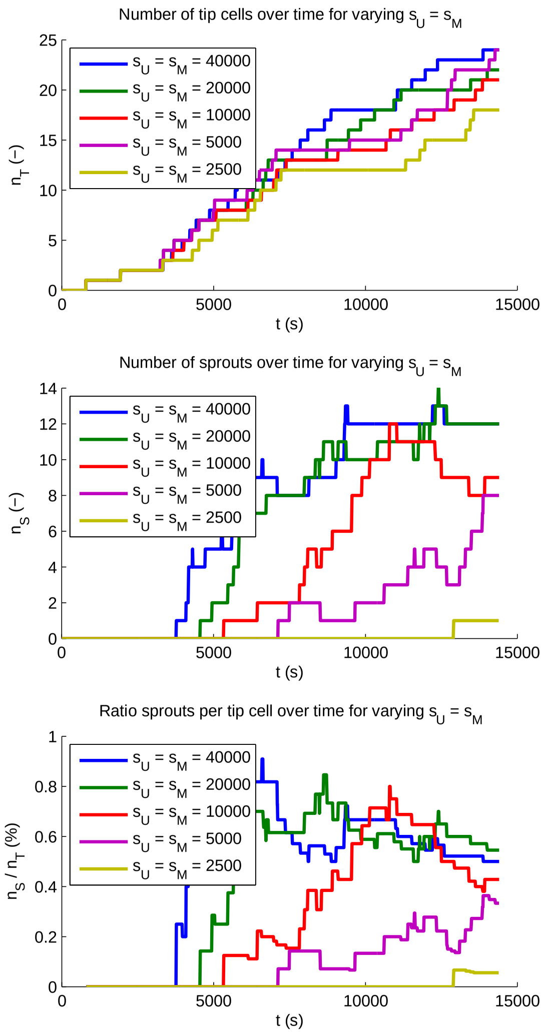

Figure 5.19: The number of tip cells n_t, the number of sprouts n_s and the ratio of sprouting success $\frac{n_s}{n_t}$ for varying MMP and uPA sourcing rates.

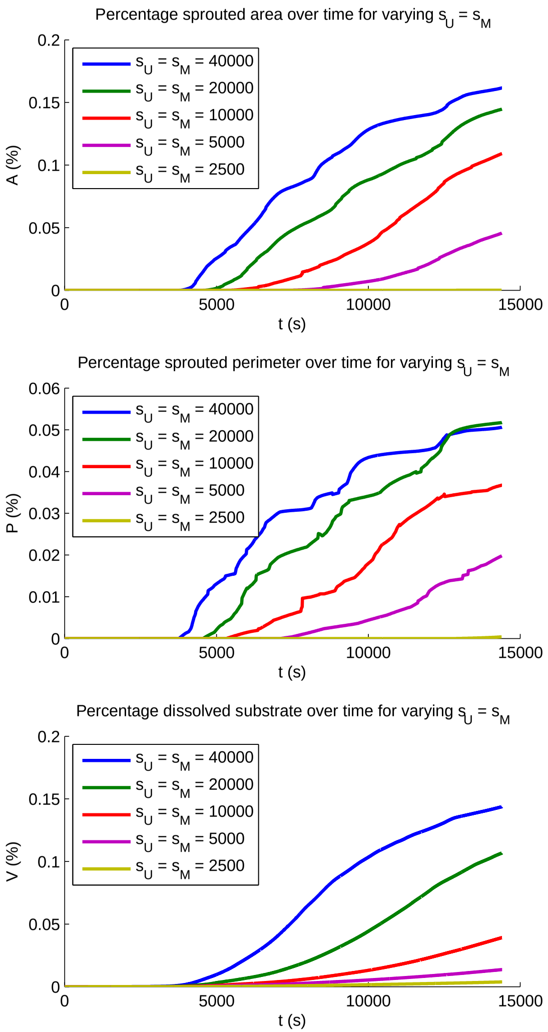

Figure 5.20: The area A and perimeter P of all sprouts at h_F as a percentage of the total area and the percentage degraded substrate V for varying MMP and uPA sourcing rates.

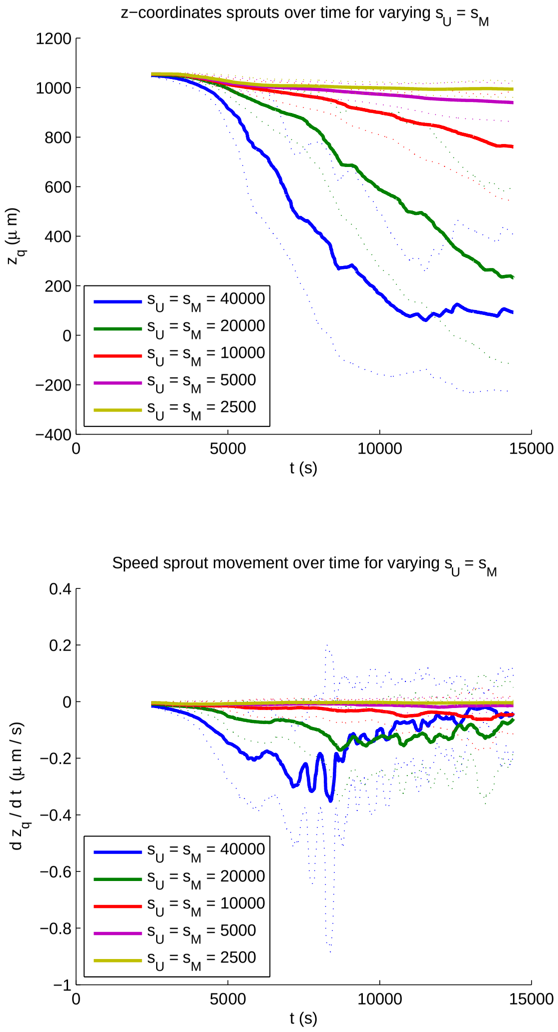

Figure 5.21: The average z-coordinate $\bar{z}$ and the average speed $\frac{d\bar{z}}{dt}$ of all cells in a simulation for varying MMP and uPA sourcing rates.

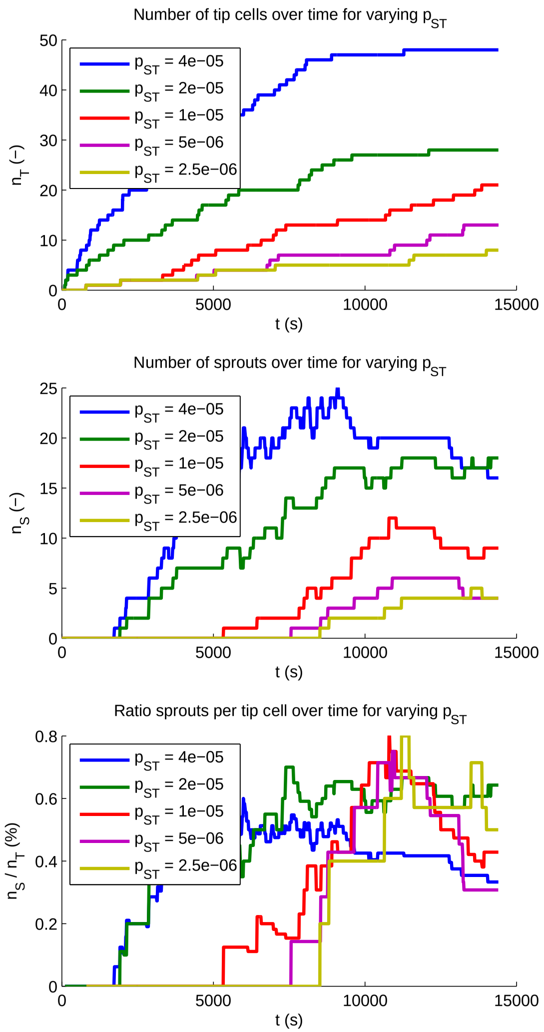

Figure 5.22: The number of tip cells n_t, the number of sprouts n_s and the ratio of sprouting success $\frac{n_s}{n_t}$ for varying maximal sprout to tip probability p_{ST}.

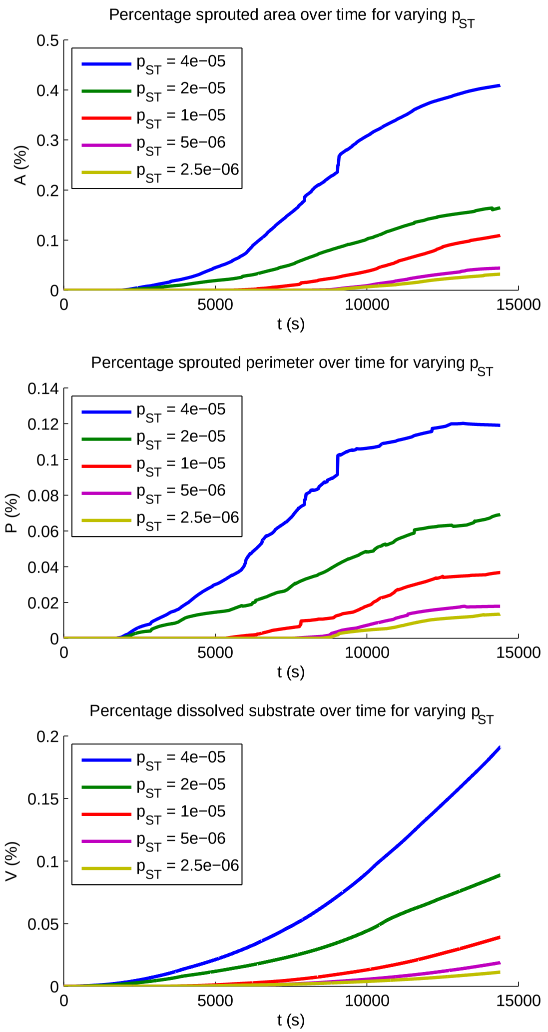

Figure 5.23: The area A and perimeter P of all sprouts at h_F as a percentage of the total area and the percentage degraded substrate V for varying maximal sprout to tip probability p_{ST}.

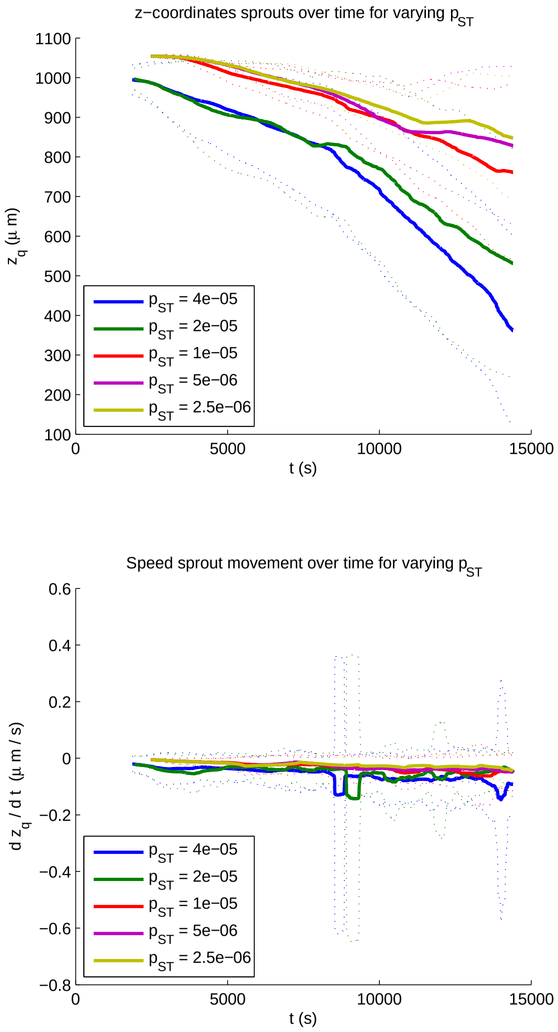

Figure 5.24: The average z-coordinate $\bar{z}$ and the average speed $\frac{d\bar{z}}{dt}$ of all cells in a simulation for varying maximal sprout to tip probability p_{ST}.

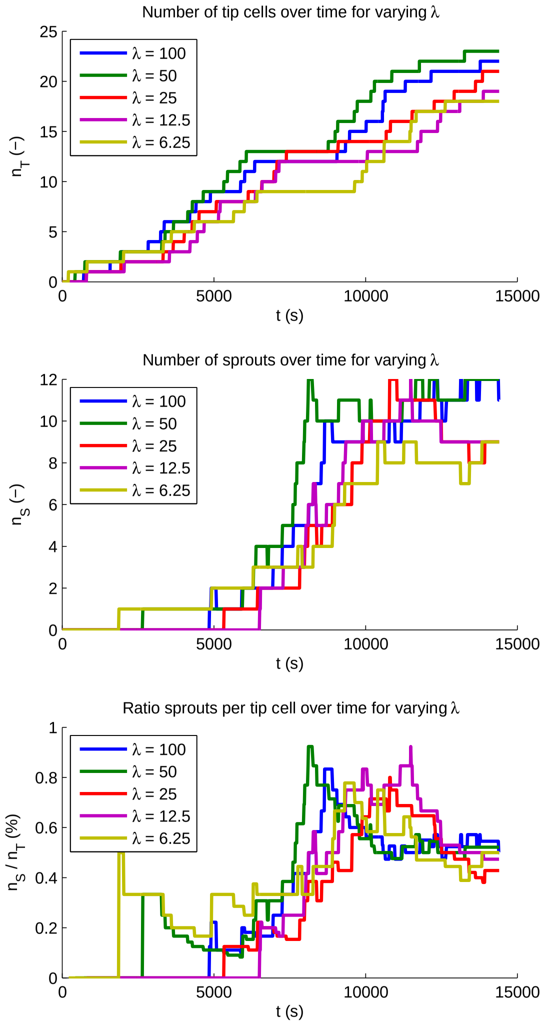

Figure 5.25: The number of tip cells n_t, the number of sprouts n_s and the ratio of sprouting success $\frac{n_s}{n_t}$ for varying adhesive constants $\hat{\lambda}$.

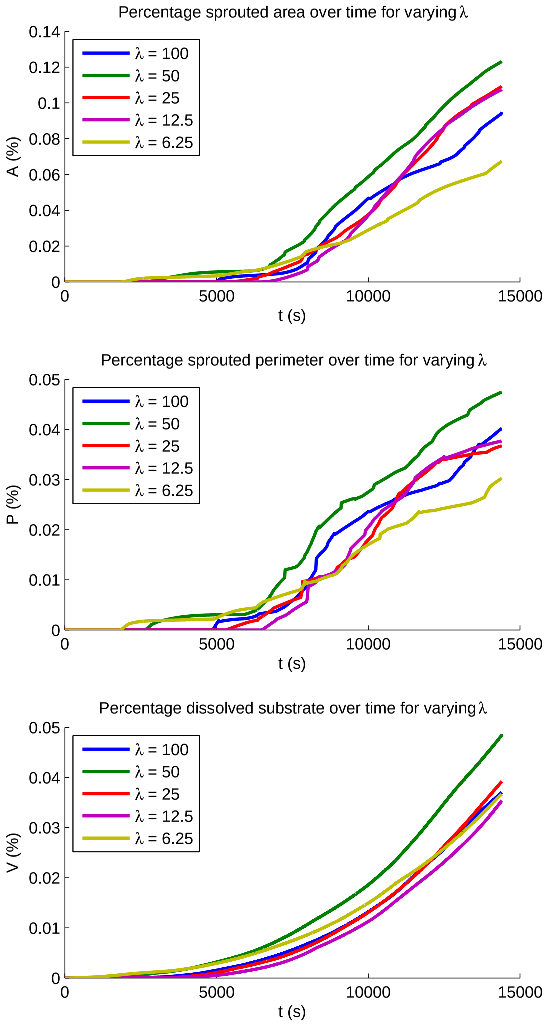

Figure 5.26: The area A and perimeter P of all sprouts at h_F as a percentage of the total area and the percentage degraded substrate V for varying adhesive constants $\hat{\lambda}$.

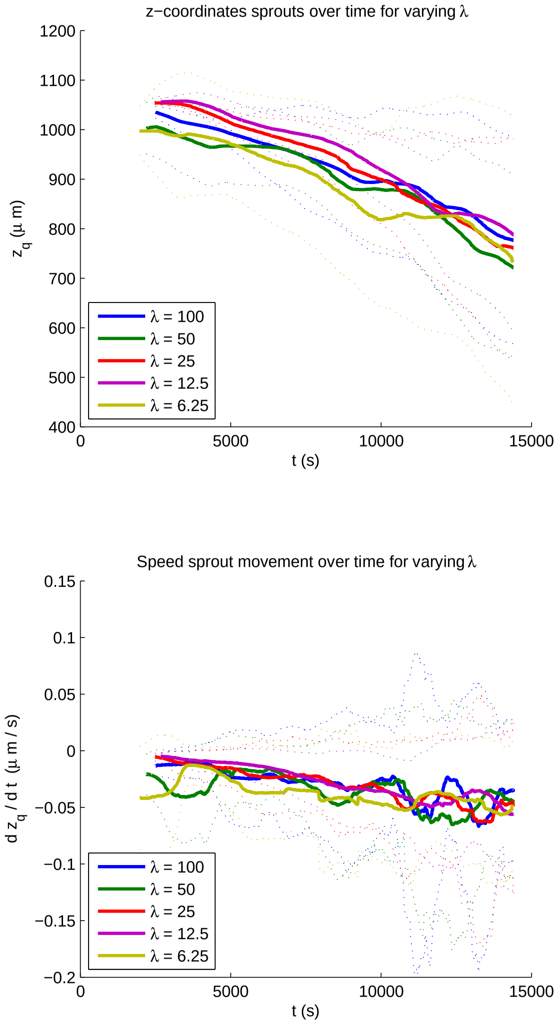

Figure 5.27: The average z-coordinate $\bar{z}$ and the average speed $\frac{d\bar{z}}{dt}$ of all cells in a simulation for varying adhesive constants $\hat{\lambda}$.

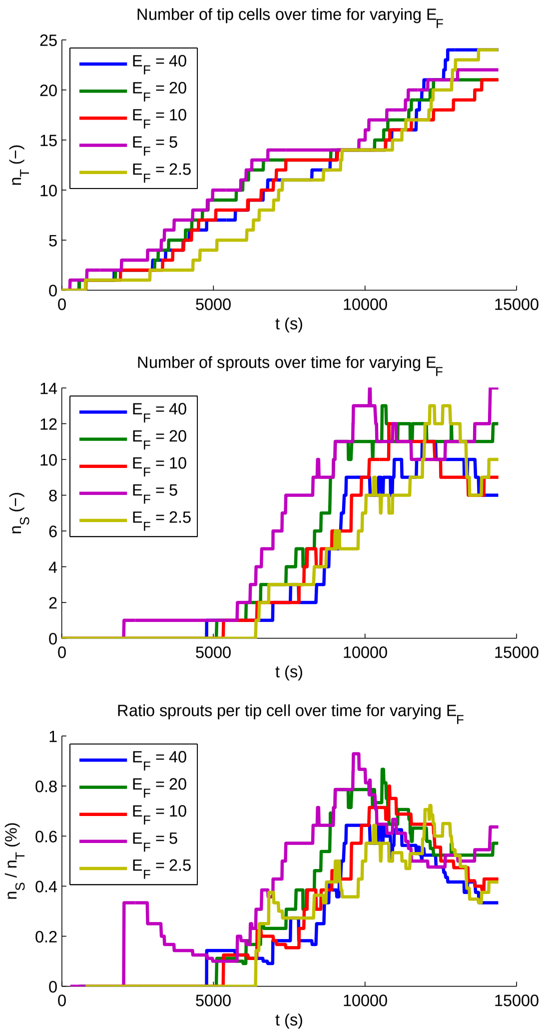

Figure 5.28: The number of tip cells n_t, the number of sprouts n_s and the ratio of sprouting success $\frac{n_s}{n_t}$ for varying substrate elasticities E_F.

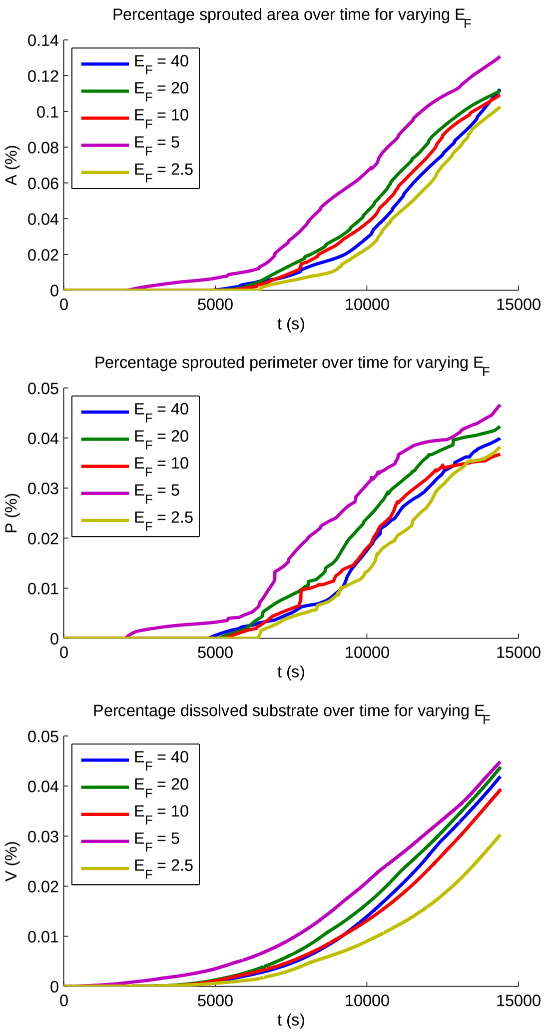

Figure 5.29: The area A and perimeter P of all sprouts at h_F as a percentage of the total area and the percentage degraded substrate V for varying substrate elasticities E_F.

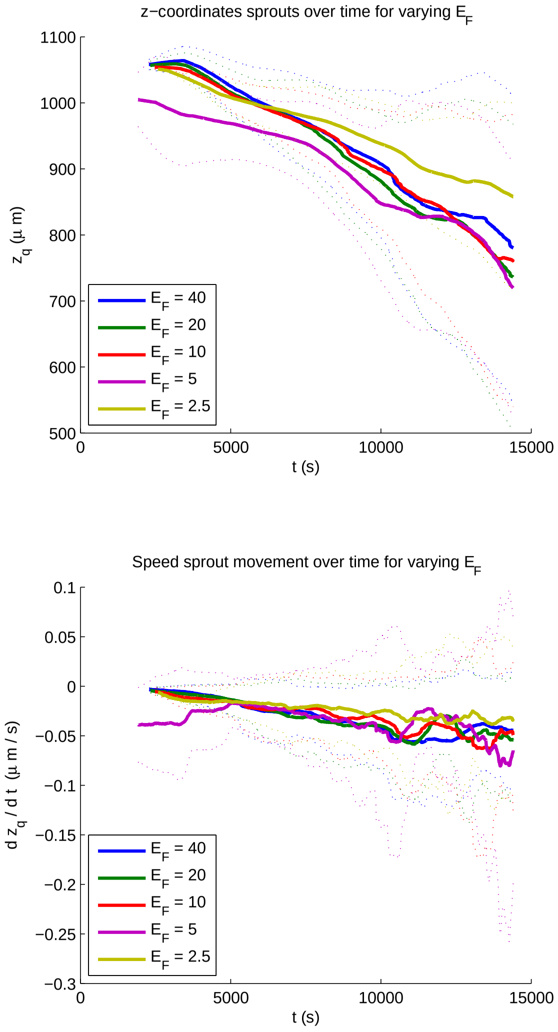

Figure 5.30: The average value $\bar{z}$ for all z_q and the average speed $\frac{d\bar{z}}{dt}$ for all z_q of all cells q in a simulation for varying substrate elasticities E_F.

5.5. COMPARISON TO THE IN VITRO WORK

Let us start by stating that the time scale of our simulation is clearly not consistent with the *in vitro* results. For our sensitivity and variance analysis, we consistently used a total simulated time of 4 hours. In these simulations however, we witness a comparable amount of sprouting activity we see *in vitro* after two or three days, meaning that our simulation is a factor 12 up to 18 times as fast. Since we saw in the sensitivity analysis that protease-substrate interactions are the main driver for sprout formation, we formulate the hypothesis that our chosen values for the sourcing rates s_U and s_M and reaction rates r_F and r_B are to high. It can be a starting point for future studies to see if lowering these values by a factor 12 to 18 sets our simulated process to the right time scale.

We would like to compare our simulation results for varying concentrations VEGF to the results obtained by the VU medical center dermatology department. As mentioned in Section 2.2, the metric used at the end of their sprouting assay is comparable to our simulated metric P. For the above mentioned reason we use the data $P(14400)$ (i.e. 4 hours of simulated time) in this comparison. In calculating the metric $P(t)$ from our simulations, we assumed that the thickness of the dark sprout perimeter is equal to R. This assumption is, based on inspection of the microscopic photographs, reasonable not free of error. The sensitivity of the image processing software used by the dermatology department and the focus of the microscopic images are another source of uncertainty. This makes quantitative comparison of our results hard, although our data seems to align well. Figure 5.31a shows the data of the *in vitro* assays for concentrations VEGF ranging from 0.1 to 25 $\frac{ng}{mL}$. The simulated metric values $P(14400)$ for varying VEGF as given in Figure 5.17 are repeated in Figure 5.31b to allow for easy comparison.

For both the *in vitro* results and the simulated results, we witness an increase in the metric P for increased values of VEGF. The response is however not completely equal, e.g. the *in vitro* increment in P is slightly more gradual. For the simulated results we have an increase of 2 % in P every time we double the concentration VEGF. In the simulated results we see a drop in the sprouting percentage for the very high concentration that we do not see in the *in vitro* results. We already mentioned that this drop does occur in the bFGF *in vitro* assay. It is therefore to quick to conclude that this is a flaw in the model. Both metrics are in the same range between 0 % and 6%.We conclude that the response of the metric P to increasing concentrations VEGF is qualitatively comparable to the *in vitro* results, but they do not align quantitatively.

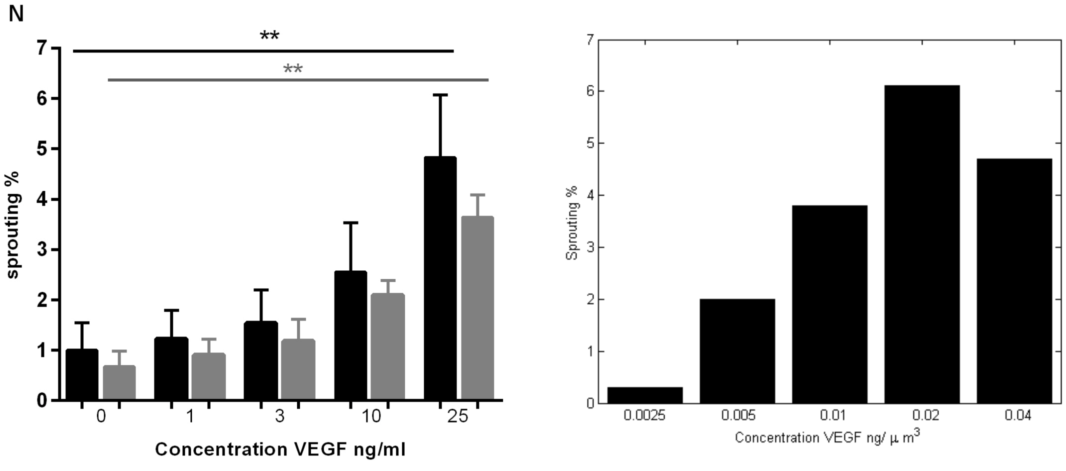

(a) The metric P in % as measured by the VU Medical Center Dermatology Department after the third day. The black bars are DTECs and the gray bars are ATECs.

(b) The metric P at $t = 14400$. We do not make a distinction between the two EC types.

Figure 5.31: Metric P (% area sprout perimeter at the top level), both from experiments our simulations for varying values of VEGF.

From laboratory observations, we witness sprouting speeds of several millimeters per day. In comparison, our sprouting speed under normal parameters is $0.053\frac{\mu m}{s} = 4.6\frac{mm}{day}$. We conclude that this is in the right order of magnitude. We also see in the *in vitro* assays that sprouts have a roughly conical shape, being twice as long as their diameter on the top level. Our simulations for normal parameters generates sprouts that are of this morphology as can be seen for example in Figure 5.32. This figure is the last frame from the video file of a normal parameter simulation.

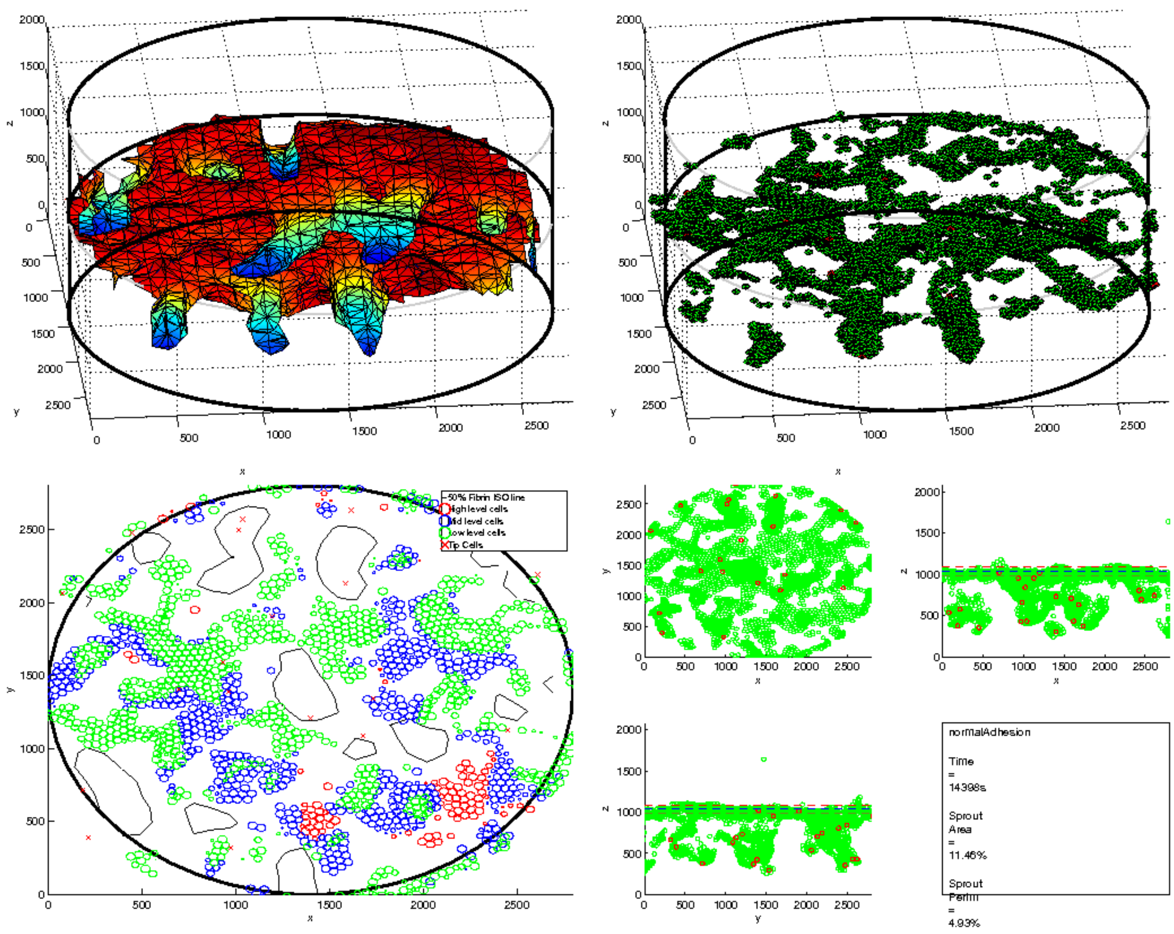

Figure 5.32: The metric P in % as measured by the VU Medical Center Dermatology Department for varying concentrations VEGF. The black bars are for DTECs and the gray bars are for ATECs.

We can conclude that qualitatively we have simulation results that mimic the *in vitro* angiogenesis assay closely. A comparison of a quantitative nature is hard to give by the lack of quantitative data from the *in vitro* assay and the methods of measurement used. We do know that the model responds in the way one would expect to the variation of all important parameters.

5.6. VASCULOGENESIS-LIKE STRUCTURE FORMATION

Namy et al. [18] conclude that substrate elasticity is important when studying vasculogenesis on substrates. When varying the elastic modulus E_F in the sensitivity analysis, we witnessed pattern formation by cells on the initial cell layer. This gave us the idea to see if we could produce vasculogenesis-like patterns using our computational model. Setting the rate parameter $p_{ST} = 0$ allowed us to do multiple model simulations for different values of E_F without the involvement of tip cells and the chemical influences from their sourcing. We start each simulation with a random initial distribution of cells. The results for values $E_F = 10, E_F = 2$ and $E_F = 1$ are given in Figures 5.33 to 5.38.

For $E_F = 10$ we see the formation of an almost perfect monolayer. For $E_F = 2$ we see that cells cluster together but parts of the monolayer are still intact. Setting $E_F = 1$, we see cells cluster together along lines and the monolayer has completely disintegrated. It would be highly interesting to investigate the possibility of simulating vasculogenesis using this model in future studies.

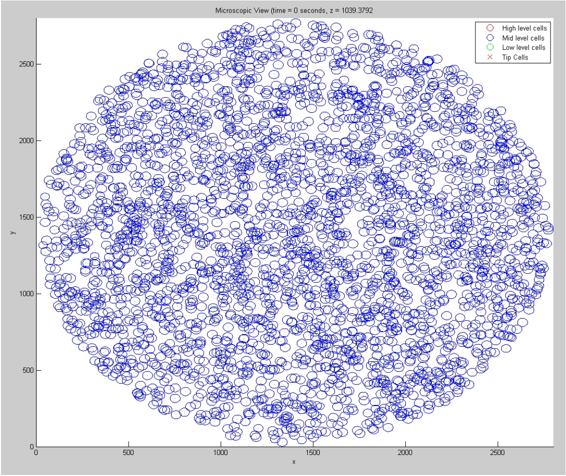

Figure 5.33: $E_F = 10, t = 0$

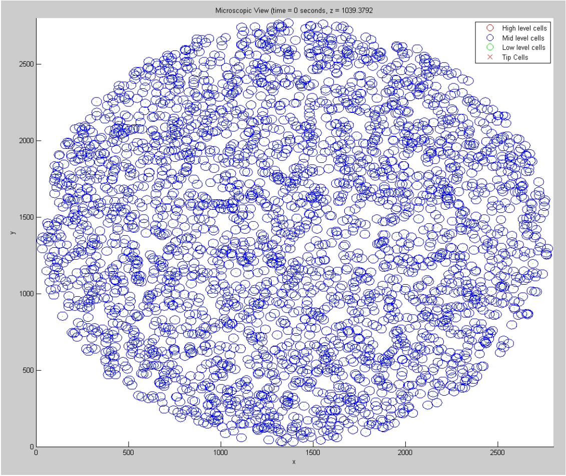

Figure 5.34: $E_F = 2, t = 0$

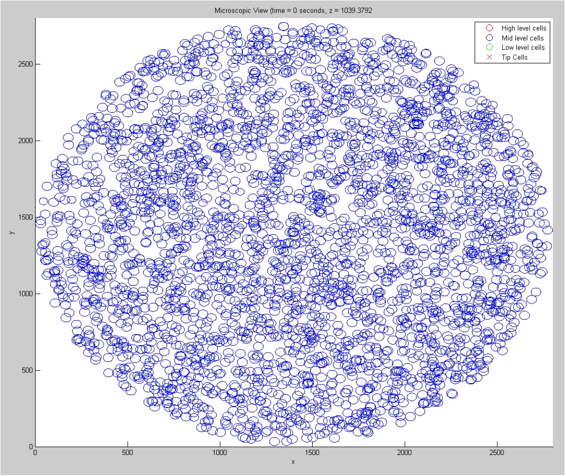

Figure 5.35: $E_F = 1, t = 0$

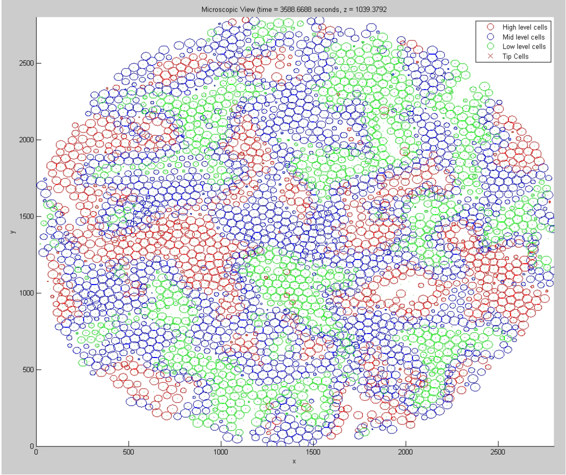

Figure 5.36: $E_F = 10, t \approx 3500$

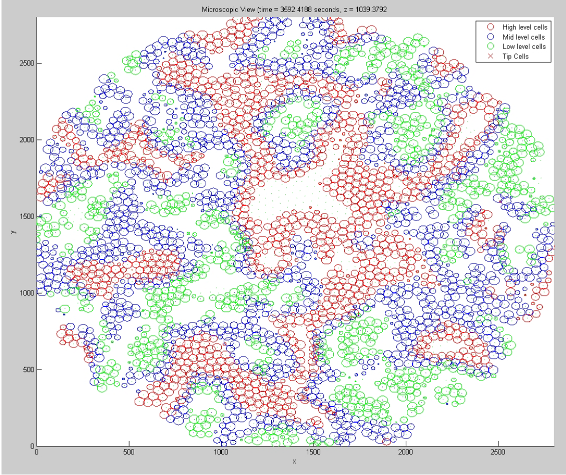

Figure 5.37: $E_F = 2, t \approx 3500$

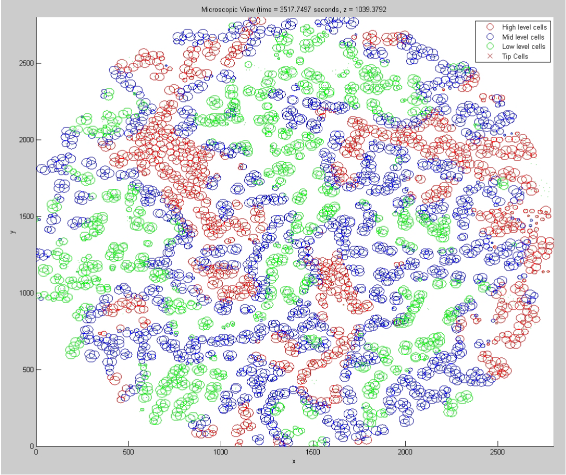

Figure 5.38: $E_F = 1, t \approx 3500$

6

CONCLUSIONS AND RECOMMENDATIONS

6.1. CONCLUSIONS

Our proposes SDCBM is qualitatively successful in describing the *in vitro* angiogenesis sprouting assay as performed by the VU medical center dermatology department. We modeled the degrading of the substrate by proteases secreted by ECs as a continuous process dependent on the properties of the substrate itself. Cell motility is modeled using a cell based formalism based on mechano-biological principles that are well established in cell biology. A probabilistic model based on local chemical conditions is proposed to model the differentiation of ECs into tip cells and stalk cells.

The proposed metrics of "the amount of sprouting" seem to align with the *in vitro* results on a qualitative level. Quantitative comparison is hard due to many uncertainties, both in the proposed computational model as well as in the measurement techniques used for the *in vitro* experiment. Sprout morphology is of the form witnessed in the experimental setting.

The metrics over time produced by the model respond to variation in parameters as we would expect from biological reasoning. Only the variation of the VEGF concentration is performed in the laboratory setting and the results are comparable. The area of sprouted perimeter range from 1% to 5% in the *in vitro* experiments and range from 0.5% to 6% in the simulations for varying concentrations VEGF.

VEGF concentrations, protease secretion rates and the probabilistic model for tip cell selection are important factors in sprout formation process. We postulate that it is the tip cell's ability to degrade the substrate in its surroundings that drives the successfulness of producing a viable sprout, the sprouts proliferation speed and its final depth. This factor is of greater importance than the chemotactic response to a higher concentration VEGF or the adhesive properties. The success rate of sprout formation for a tip cell are between 50 % and 60 %, independent of the number of tip cells present. We postulate that also *in vitro* we have more tip cells than actual sprouts.

The SDCBM was built to simulate angiogenesis. Vasculogenesis is another process witnessed in studies containing ECs as described by Namy et al. [18] and Merks et al. [5]. Since our SDCBM describes EC behavior in a general sense, we also witness vasculogenesis-like structure formation for varying values of the substrate elasticity. Since modeling vasculogenesis was not the scope of this study, we leave further investigation of this phenomenon for future research.

6.2. DISCUSSION AND RECOMMENDATIONS

In the modeling process, we made choices and performed analyses as presented in this thesis. For some of these, other choices could have been made and we present an overview of them.

We based most parameters and scaling factors in the derivation of the cell movement model on physical or biological principles. The only parameter that forms the exception is the dimensionless scaling factor $\hat{\lambda}$.

Although we have seen in our sensitivity analysis that this parameter does not play an important role in angiogenesis, it does mediate the contiguity of the monolayer of cells. Further investigation of the adhesive process and the way to capture it in a mathematical formalism is advised.

Proteins decay naturally over time, a property that is not reflected in the chemical model as used. This property may be implemented by adding a decay factor to the system of PDEs. E.g. for the concentration VEGF, we add $-d_V c_V$ to the right hand side of the PDE. Here, d_V is a decay factor with dimension $[\frac{1}{s}]$. In our FEM, this would entail an extra term in the mass matrix S_V.

Limited by computational resources, we have only performed a sensitivity analysis on five parameters and we only did twelve model runs for the estimator of the mean of all sprouting metrics. Extra computational power or parallelizing the code could improve these numbers.

We used a FEM scheme with linear basis functions. Moving to a higher order basis functions could improve the accuracy of the computational scheme. However, using Newton-Cotes integration over the mass matrix M to avoid spurious oscillations introduces a $\mathcal{O}(h)$ error. Implementing a higher order scheme is only useful if the oscillatory problem is dealt with in another way and to do so we present a still not fruitful onset in Appendix E.4.3. Furthermore, all the interpolations we made for the cell movement parameters are linear. It might be useful to validate the derivation and the modeled linearity of the terms α, γ and λ.

It might be useful to conduct further investigation into the chosen parameters. Sources in the literature give very different values for for example the diffusive speed D_V. Other parameters were not found in literature and estimated based on the known ones. Our initial concentrations VEGF are very different from the real values used in the *in vitro* study. We compensate by scaling down the chemotactic response to the VEGF concentration accordingly. Substituting these factors with more realistic values will probably not alter the model outcome but will make the model more understandable. Validation of all these choices will make the model more solid and can maybe solve te problem of the wrong time scale.

In the current model, the edges of the domain do not act forces on the cells, making it possible for cells to move out of the computational domain. Cells that have moved out of the domain are not within an element of the FEM mesh and therefore can not sense or source any chemicals or react to the substrate properties. This fact on itself forms no problem for the rest of the computational model, but does require much useless computational effort, predominantly in trying to find the (non existing) element a cell is located in. An improvement would be to remove these cells from the computations. Another approach could be to give the boundaries contact mechanical properties or to lay a monolayer of ghost cells on the boundaries that provide the contact mechanical forces to keep the cells in the problem domain.

In the formulation of the rates $\tilde{\lambda}_{ST}$ and $\tilde{\lambda}_{ST}$ of tip cell selection, we normalize the VEGF and DLL4 concentrations with the initial concentration VEGF c_v^0. In hindsight, this is no reasonable assumption since tip cell selection is now not dependent on the absolute VEGF concentration, but rather on a saturation with respect to the initial condition. It would be an improvement to remove this normalizing factor and reconsider these rates.

We model the contact mechanics between cells and this seems to work well. It would be interesting to see what happens if we incorporate cell-matrix contact mechanical properties. We can also incorporate matrix porosity and permeability to improve the model for cell-matrix interaction. As an improvement upon this work, viability of cells and cell proliferation can be modeled.

It would be very interesting to see if we can verify more of our simulation results with laboratory measurements. This incorporates measurement of other metrics than only $P(t)$ and maybe 3D visualization of the sprouting assay using multi-focal plane microscopy or other techniques.

Extensions of the proposed model can be made to work towards the *in vivo* situation. We can model cells contained in the ECM that consume oxygen and secrete VEGF when deprived of oxygen. We could additionally monitor the oxygen concentrations. Oxygen sources from existing vessels at a constant rate and reacts all types of cells proportional to the concentration. We will have a similar diffusion-reaction-source equation governing the concentration of oxygen c_O:

$$\frac{\partial c_O}{\partial t} = \nabla \cdot [D_O(f_F, f_B, f_E)\nabla c_O] - \sum_{q\in\theta} r_O \delta(\mathbf{x}-\mathbf{x}_q)c_O + S_O\delta(\mathbf{x}-\mathbf{x}_l),$$

where D_O is a diffusive function, S_O is the source strength, $\delta(\mathbf{x}-\mathbf{r}_l)$ is 1 inside the lumen and r_O is the reaction constant. The cells secrete VEGF reversely proportional to the oxygen concentration. For a certain concentration c_O^s, the secretion of VEGF stops. Hence the source strength is proportional to $\max\left(0, 1-\frac{c_O}{c_O^s}\right)$. The diffusion-reaction-source equation governing the concentration of VEGF c_V looks like:

$$\frac{\partial c_V}{\partial t} = \nabla \cdot [D_V(f_F, f_B, f_E)\nabla c_V] - \sum_{q\in\theta} r_V \delta(\mathbf{x}-\mathbf{x}_q)c_V + \sum_{q\in\theta} S_V \max\left(0, 1-\frac{c_O}{c_{O_s}}\right)\delta(\mathbf{x}-\mathbf{x}_q),$$

where D_V is the diffusion constant, S_V is the source strength and r_V is the reaction constant. This model to some extent follows the reasoning of Maggelakis in [33].

A

GLOSSARY OF BIOCHEMICAL TERMS AND PROCESSES

A.1. PROCESSES

- *Angiogenesis:* Creation of new blood vessels from pre-existing vessels.
- *Vasculogenesis:* Creation of new blood vessels by forming *endothelial* cells from endothelial progenitor cells.
- *Proliferation:* Cell division.
- *Chemotaxis:* Active cell migration in response to a chemical stimulus. Mostly in the direction of the gradient of a concentration field solvent in the surroundings. The substance that cells are being attracted towards is called the *chemoattractant.*
- *Haptotaxis:* Active cell migration in response to adhesion to proteins fixed in the *extracellular matrix*. *Fibronectin* is an example of a protein in the basement membrane causing haptotaxis.
- *Elongation:* Changing shape towards an attractant.
- *Contact Inhibition:* A cell not being respondent to autocrine chemotaxis when the membrane is in contact with another cell. For example, *VE-cadherin* which binds cells together causes cells to not respond to *autocrine chemotaxis.*
- *Autocrine Chemotaxis:* Chemotaxis caused by a chemical gradient secreted by the cell itself.
- *Anastomosis:* The process in angiogenesis where sprouts join. Sprouts can join tip-to-tip or the tip cell of a sprout can join halfway with another sprout.

A.2. PHYSIOLOGICAL DEFINITIONS

- *In vitro:* In a laboratory setting
- *In vivo:* In a living organism
- *De novo:* Newly formed
- *Endothelial cells:* Cells that line the inside of a blood vessel in a mono-layer. They rest on the *basement membrane.*
- *Endothelium:* The monolayar of *endothelial cells* forming the inner layer of a blood vessel.
- *HUVECs.* Human Umbilical Vein Endothelial Cells. Endothelial cells acquired from the Umbilical Vein.
- *Motility:* Ability to move and migrate.

- *Mesoderm:* The skin layer between the ectoderm and the endoderm.
- *Fibroblast:* Cells that, amongst other functions, form the *ECM*.
- *Granulation Tissue:* New connective tissue in the wound healing process that is filled with blood vessels formed by angiogenesis. It is deposited by *fibroblasts*, which rely on oxygen from the blood vessels to do so.
- *ECM:* Extra Cellular Matrix. Everything outside the cells in a multi-cellular structure. Consists of fiber like structures such as *collagen*,*elastin* and *fibronectin*. The *Basement membrane* is part of the ECM.
- *Basement membrane:* Thin sheet of fibres beneath the *endothelium*.
- *Hypoxic tissue:* Tissue that is low on oxygen supply. Hypoxic tissue secretes, among other things, *VEGF*.
- *Matrix:* A substance used to grow cell cultures on. Examples are fibrin matrices or matrigel matrices.
- *Sprout:* Start of a new micro vessel.
- *Tip Cells:* Endothelial cells that are leading the growth of a sprout. Tip cells secrete a signal substance that inhibit *stalk cells* to differentiate into tip cells. Tip cells secrete proteases that degrade the fibrin matrix and the boundary membrane. The selection of the tip cell is regulated by VEGF, DLL4 and Notch1 signaling [52].
- *Stalk Cells:* Endothelial cells that follow a tip cell.
- *Lumen:* The space between endothelial cells in which blood can flow.
- *Pseudopodia:* Temporary longitudinal bulges of the cell membrane. In chemotaxis towards higher concentrations of chemoattractant.

A.3. SUBSTANCES

- *Angiogenesis inhibitor:* Group of substances that can slow down the process of angiogenesis.
- *Angiogenic Growth Factors:* Group of substances that can speed up the process of angiogenesis.
- *VEGF:* Vascular Endothelial Growth Factor. An angiogenic growth factor. A signal protein given off by *hypoxic tissue* to induce angiogenesis. It activates *endothelial cells* in pre-existing blood vessels to degrade the basement membrane.
- *bFGF:* basic Fibroblast Growth Factor, sometimes FGF-2. An angiogenetic growth factor.
- *Collagen:* Structural protein in skin.
- *Fibrin:* Structural protein formed in wound beds.
- *VE-cadherin:* A homophilic, trans-membrane cell-adhesion cadherin type protein that binds cells to one another. Besides its adhesive function, it plays an inhibiting role in the *VEGF* signaling pathway [53]. The contact inhibited chemotaxis is modeled after this effect [16].
- *Proteolytic enzymes:* Enzymes that degrade proteins.
- *TNFα:* Tumor necrosis factor alpha. Induces receptor bound u-PA (urokinase-type plasminogen activator) activity, a proteolytic enzyme, which degrades fibrin matrices. It is used in fibrin mono layer experiments to maintain the mono-layer.
- *MMP:* matrix metalloproteinases. Proteolytic enzymes that degrades boundary membrane.
- *uPA:* urokinase-type plasminogen activator. A proteolytic enzyme that degrades fibrin.
- *DLL4:* Enzyme secreted by tip cells to prevent stalk cells to transform into tip cells and make them chemotactically move towards the tip cell.
- *fibronectin:* a matrix macromolecule which occurs in two different forms. 1. As a soluble glycoprotein found in various body fluids (including blood), known as plasma fibronectin. 2. As an insoluble constituent of the extracellular matrix and basement membranes of cells, known as cellular fibronectin

B

CPM IMPLEMENTATION

As a way of getting acquainted with the existing CPM models as used by Merks [16] during the literature study, a stripped-down version of a CPM was implemented. This chapter briefly summarizes the choices made in the implementation of this model. In our computational model, we solve the PDEs on a grid identical to the lattice sites using a finite volumes scheme. Each time step consists of three phases. First, the chemicals are updated. Based on the new distribution of the chemicals, the substrate sites are stochastically degraded. At last, we calculate the maximal and minimal energy lattice site for each cell and acquire and repel the lattice sites successively.

B.1. DIFFERENTIAL EQUATIONS GOVERNING THE CHEMICALS

Our domain consists of a square lattice of size $N \times M$. Each lattice site has a spin σ_x, describing the content inside. The spin can a number $c \in \theta = \{1, \ldots, n\}$, meaning that the lattice site belongs to the biological cell c or one of the substrate components fibrin F, BM B, ECF E or Lumen L. Opposed to our newly proposed SDCBM, we distinguish between lattice sites that have fluid (ECF) in them and which are in direct contact with the lumen and those lattice sites that are not in direct contact. Sites not in contact have spin E and sites in direct contact with the "blood flow" have spin L We denote the set of stalk cells θ_s and the set of tip cells θ_t. We define indicator functions

$$\delta_{\sigma_x,\theta} = \begin{cases} 1 \text{ if } \sigma_x \in \theta, \\ 0 \text{ otherwise,} \end{cases} \qquad \delta_{\sigma_x,\theta_t} = \begin{cases} 1 \text{ if } \sigma_x \in \theta_t, \\ 0 \text{ otherwise,} \end{cases} \qquad \delta_{\sigma_x,\theta_s} = \begin{cases} 1 \text{ if } \sigma_x \in \theta_s, \\ 0 \text{ otherwise.} \end{cases}$$

$$\delta_{\sigma_x,F} = \begin{cases} 1 \text{ if } \sigma_x = F, \\ 0 \text{ otherwise,} \end{cases} \qquad \delta_{\sigma_x,B} = \begin{cases} 1 \text{ if } \sigma_x = B, \\ 0 \text{ otherwise,} \end{cases} \qquad \delta_{\sigma_x,E} = \begin{cases} 1 \text{ if } \sigma_x = E, \\ 0 \text{ otherwise.} \end{cases}$$

In analogy to Gamba [13], Serini [14] and Merks [5], the concentration of the chemoattractant VEGF c_V is governed by the diffusion-reaction PDE

$$\frac{\partial c_V}{\partial t} = D_V \nabla^2 c_V - r_V \delta_{\sigma_x,\theta} c_V,$$

where D_V is a diffusive constant, r_V is the reaction speed. Diffusion is assumed to be independent of the type of medium it is in. Besides this assumption, VEGF reacts with endothelial cells at a rate that is proportional to the concentration c_V.

The three enzymes MMP, uPA and DLL4 are secreted by tip cells and diffuse through the tissue. Their concentrations are denoted by c_M, c_U and c_D. MMP reacts with the boundary membrane to degrade it. uPA reacts with fibrin to degrade it. DLL4 reacts within stalk cells. The governing equations are

$$\begin{aligned} \frac{\partial c_M}{\partial t} &= D_M \nabla^2 M & &- r_M \delta_{\sigma_x,B} c_M & &+ S_M \delta_{\sigma_x,\theta_t}, \\ \frac{\partial c_U}{\partial t} &= D_U \nabla^2 U & &- r_U \delta_{\sigma_x,F} c_U & &+ S_U \delta_{\sigma_x,\theta_t}, \\ \frac{\partial c_D}{\partial t} &= D_D \nabla^2 D & &- r_D \delta_{\sigma_x,\theta_s} c_D & &+ S_D \delta_{\sigma_x,\theta_t}. \end{aligned}$$

We model the boundary conditions as “no flux” boundaries. Chemicals can not pass through the boundaries. This is unlike the model uses by Merks [5], where a Dirichlet boundary condition is used to be “absorbing” the chemoattractant. Merks uses a 500 × 500 lattice where each site is around $4\mu m^2$ in area. Cells contain around 45 lattice sites, giving them a radius of 7.5 μm.

We solve the equations for the chemicals on the lattice using a finite volume method upon which we will not elaborate here.

B.2. INITIAL CONDITIONS

Initially, the upper two fifth of the lattice sites get spin L. The lower three fifth get spin F and in between there is a single row of lattice sites having spin B. We specify a number of rectangular cell morphologies as initial states. We randomly select a cell morphology and place the cells next to each other on the BM layer, changing the spins of the lattice sites accordingly. One in every seven cells is appointed to be a tip cell. We give each cell a distinct color and we fill the lattice sites of tip cells with asterisks.

The initial conditions of the chemical is consistent with the initial conditions in our SDCBM. They are all of value 0, except for the concentration VEGF which is c_V^0 within the fibrin. The initial distribution of the lattice sites can be seen in Figure B.1.

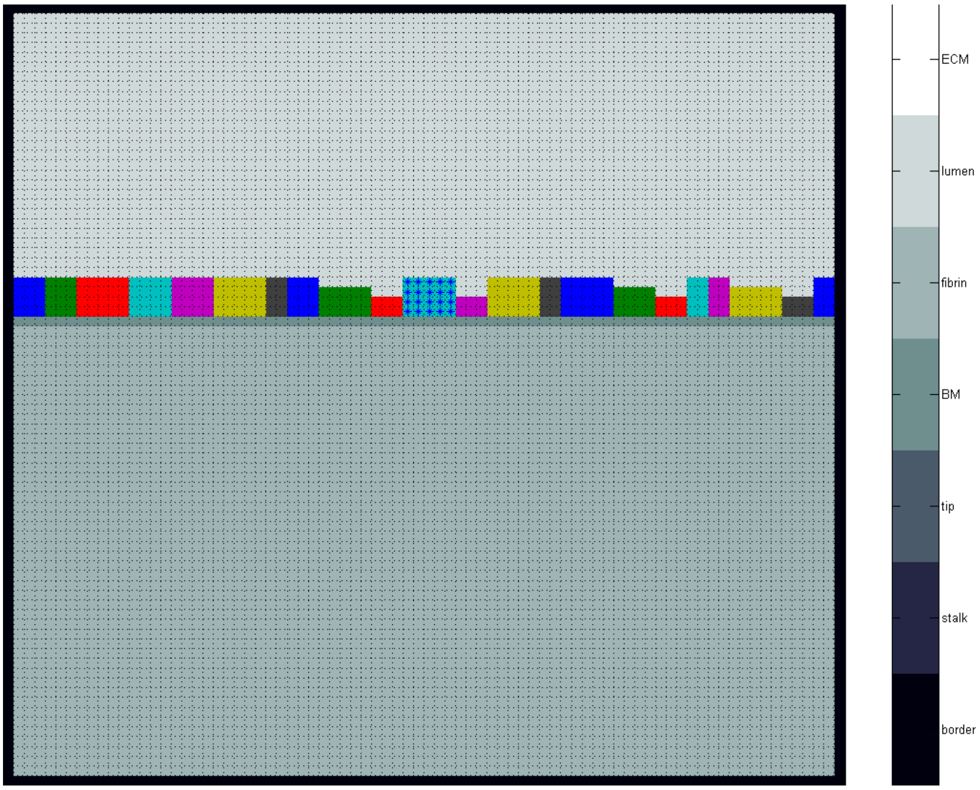

Figure B.1: Initial distribution of the lattice sites in our CPM model.The tip cell is marked with asterisks.

B.3. STOCHASTIC DEGRADING OF THE SUBSTRATE

The BM degrades into ECF with a probability proportional to the concentration MMP. For each lattice site we formulate a probability function $\mathbb{P}(E|B) : c_M \to [0,1]$ giving the probability that a lattice site with spin B changes to spin E per unit of time and we define

$$\mathbb{P}(E|B) = \delta_{\sigma_x,B}\left[1 - e^{-\frac{c_M}{\mu_B^-}}\right],$$

Here, μ_B^- is a reaction coefficient determining the “durability” of the BM. Note that thanks to the factor $\delta_{\sigma_x,B}$, we only have non-zero probabilities for lattice sites that actually have spin B. Likewise for the lattice sites with a fibrin spin F, we define a probability of a spin change to E per unit of time dependent on the concentration uPA given by

$$\mathbb{P}(E|F) = \delta_{\sigma_x,F}\left[1 - e^{-\frac{c_U}{\mu_F}}\right].$$

Lattice sites with spin E that are a direct neighbor of a lattice site with spin L immediately change their spin to L as if they “fill up” with the blood stream. BM can form between stalk cells (not tip cells) and either fibrin or the ECF. The concentration MMP should be sufficiently small. We model per unit of time

$$\mathbb{P}(B|E) = \delta_{\sigma_x,E}e^{-\frac{c_M}{\mu_B^+}}.$$

We empirically set the parameters $\mu_B^- = 10$, $\mu_B^- = 5$ and $\mu_B^+ = 0.2$.

B.4. STOCHASTIC ELONGATION OF THE CELLS

Cells stay at the same size. Every time step, the most positive and the most negative lattice site in the cell and it’s surrounding is calculated and they are acquired and repulsed respectively. This is the largest difference compared to the CPM implemented by Merks. We implement a Hamiltonian function $\mathcal{H}$ as is usual when implementing a cellular Potts model and we define the probability of a spin change using the same function Merks uses in Equation 3.1. Both tip and stalk cells chemo-attract towards a gradient of VEGF. Stalk cells also chemo-attract towards a gradient of DLL4. We implement this by modeling

$$\mathcal{H}_{chemo} = \lambda_V c_V + \lambda_D c_D$$

for stalk cells. For tip cells, we omit the c_D term. We set $\lambda_V = \lambda_D = 50$. Cells adopt lattice sites more easily in ascending order from the BM, Lumen, Fibrin and ECF. Cells never add any lattice sites from the boundary. The Hamiltonian energies are chosen such that this order is attained. We implement this by modeling

$$\mathcal{H}_{substrate} = \delta_{\sigma_x,E}\mu_E + \delta_{\sigma_x,F}\mu_F + \delta_{\sigma_x,B}\mu_B + \delta_{\sigma_x,L}\mu_L,$$

and setting penalties $\mu_F = -200$ and $\mu_B = -600$ and bonuses $\mu_E = 50$ and $\mu_L = 0$. Cells tend to stay in a compact shape. Lattice sites in the cell further away from the center of gravity get smaller positive energies. For a cell i we denote the center of gravity by $\mathbf{r}_i$ and for a given lattice site (n,m) we model

$$\mathcal{H}_{shape} = \frac{\sigma}{\|(n,m) - \mathbf{r}_i\| + 1},$$

and we set $\sigma = 200$. Cells tend to stick together. Lattice sites directly adjacent to lattice sites in other cells get positive energies. For a cell i we model

$$\mathcal{H}_{Cell-Cell} = \delta_{\sigma_x,\theta\setminus i}\lambda_c,$$

and we set $\lambda_c = 100$. Cells tend to stick to the fibrin matrix and to the BM. Lattice sites directly adjacent to elements in the BM or the fibrin scaffold get positive energies. We model

$$\mathcal{H}_{Cell-Matrix} = \delta_{\sigma_x,B}\lambda_B + \delta_{\sigma_x,F}\lambda_F,$$

and we set $\lambda_B = 200$ and $\lambda_F = 100$.

The total energy of a lattice site (n,m) for a given cell i is given by the sum of all the individual Hamiltonian functions.

B.5. RESULTS

We run two separate simulations for a different number of time steps in Figures B.2 and B.3. It is clear that the mechanism of this model gives results that we would expect, but since CPM’s are not the main subject of this thesis, we will not go into detail on how to tune all the parameters and speed up the model to work reasonable for a large number of cells. It can be concluded that the set of biochemical and biomechanical mechanisms implemented indeed causes angiogenic-like behavior. This strengthens us in implementing these same mechanisms in our newly proposed SDCBM.

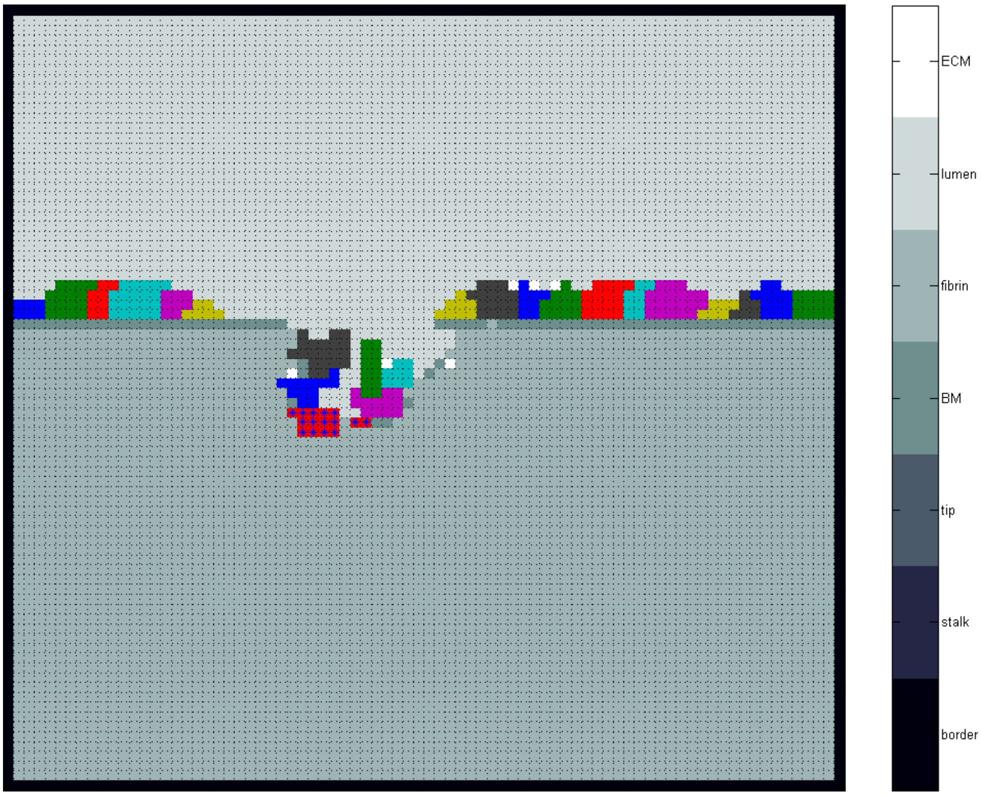

Figure B.2: The elongated cells in our CPM after several time steps.

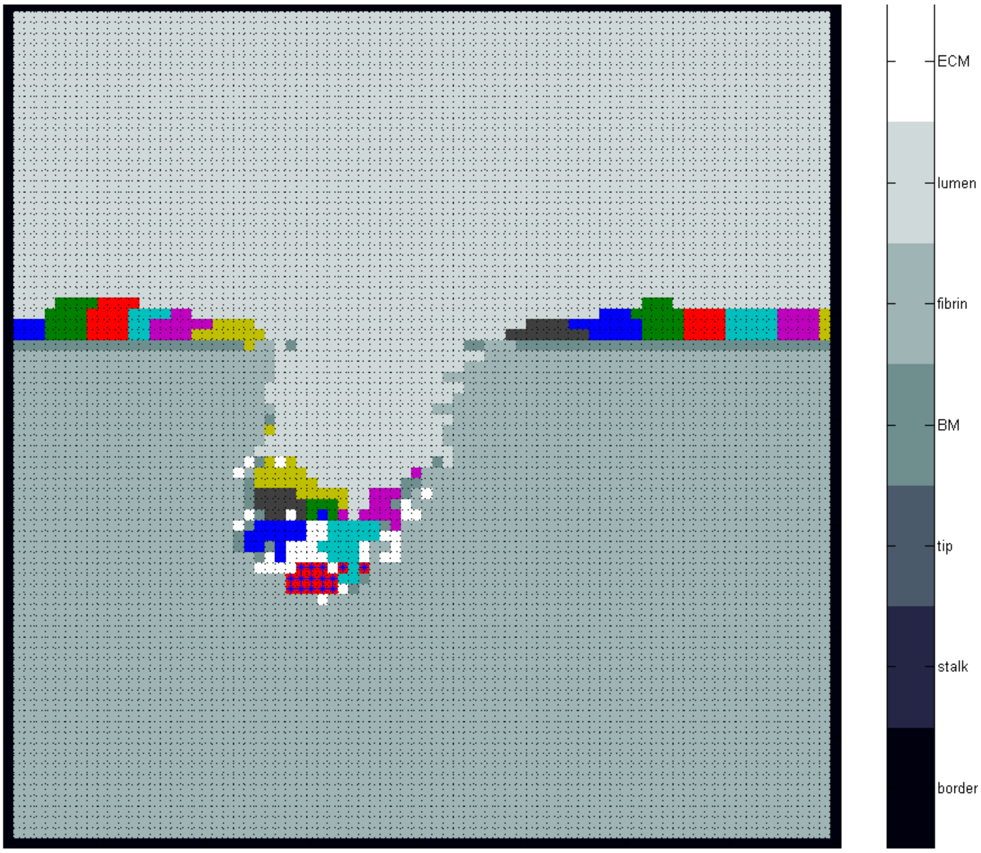

Figure B.3: The elongated cells in our CPM after several time steps.

C

THE FEM FOR THE PDE LAYER

C.1. GALERKIN EQUATIONS FOR THE PDE OF c_M

We derive the Galerkin equations for the PDE of only one of these equations. The derivations for the other equations follow the same principles. Consider the PDE on $\Omega \subset \mathbb{R}^3$ for the concentration of MMP c_M where we abbreviate $D_M = D_M(f_F, f_B, f_E)$ to shorten notation:

$$\frac{\partial c_M}{\partial t} = \nabla \cdot [D_M \nabla c_M] - r_M c_M f_B + \sum_{q \in \theta_t} s_M \delta(\mathbf{x} - \mathbf{x}_q) c_V,$$

with a no-flux boundary condition $\frac{\partial c_M}{\partial n} = 0$ on the boundary Γ. We multiply by a test function $\varphi \in H^1(\Omega)$ and integrate over Ω:

$$\int_\Omega \frac{\partial c_M}{\partial t} \varphi dV = \int_\Omega \nabla \cdot [D_M \nabla c_M] \varphi dV - \int_\Omega r_M c_M f_B \varphi dV + \int_\Omega \sum_{q \in \theta_t} s_M \delta(\mathbf{x} - \mathbf{x}_q) c_V \varphi dV.$$

Using $\nabla \cdot [D_M \nabla c_M] \varphi = \nabla \cdot [D_M \nabla c_M \varphi] - (\nabla \varphi) \cdot (D_M \nabla c_M)$ and Gauss' divergence theorem we see

$$\int_\Omega \frac{\partial c_M}{\partial t} \varphi dV = \int_\Omega \nabla \cdot [D_M \nabla c_M \varphi] dV - \int_\Omega (\nabla \varphi) \cdot (D_M \nabla c_M) dV - \int_\Omega r_M c_M f_B \varphi dV + \int_\Omega \sum_{q \in \theta_t} s_M \delta(\mathbf{x} - \mathbf{x}_q) c_V \varphi dV,$$

and

$$\begin{aligned}\int_\Omega \frac{\partial c_M}{\partial t} \varphi dV &= \int_\Gamma [D_M \nabla c_M \varphi] \cdot n d\Gamma - \int_\Omega (\nabla \varphi) \cdot (D_M \nabla c_M) dV - \int_\Omega r_M c_M f_B \varphi dV + \int_\Omega \sum_{q \in \theta_t} s_M \delta(\mathbf{x} - \mathbf{x}_q) c_V \varphi dV. \\ &= \int_\Gamma D \frac{\partial c_M}{\partial n} \varphi d\Gamma \quad - \int_\Omega D (\nabla c_M) \cdot (\nabla \varphi) dV \quad - \int_\Omega r_M c_M f_B \varphi dV + \int_\Omega \sum_{q \in \theta_t} s_M \delta(\mathbf{x} - \mathbf{x}_q) c_V \varphi dV.\end{aligned}$$

Because of the boundary condition, we see that the boundary term drops out and we end up with the weak formulation

$$\int_\Omega \frac{\partial c_M}{\partial t} \varphi dV = -\int_\Omega D_M (\nabla c_M) \cdot (\nabla \varphi) dV - \int_\Omega r_M c_M f_B \varphi dV + \int_\Omega \sum_{q \in \theta_t} s_M \delta(\mathbf{x} - \mathbf{x}_q) c_V \varphi dV, \tag{C.1}$$

and we have to find a $c_M \in L^2([0, T], H^1(\Omega))$ that satisfies Equation C.1 $\forall \varphi \in H^1(\Omega)$ on our domain Ω and for $t \in [0, T]$. The concentration MMP c_M is varying in both time and space and we may write $c_M = c_M(\mathbf{x}, t)$. We introduce a time independent discretization into n_{el} tetrahedral elements with in total n nodal points (nodes). We denote the elements by e_l for $l = 1, \ldots, n_{el}$. We denote the nodal points by n_j for $j = 1, \ldots, n$ and we denote their spacial coordinates by $\mathbf{x}_j = (x_j, y_j, z_j)^T$. Corresponding with each node n_j we introduce a piecewise linear basis function $\varphi_j(\mathbf{x}) = \alpha_j + \beta_j x + \gamma_j y + \delta_j z$. We choose the parameters $\alpha_j, \ldots, \delta_j$ (inside each element) such that on each nodal point n_i we have $\varphi_j = 1$ if $i = j$ and 0 otherwise, so called tent functions.

On every element e_l we introduce a local numbering and we reserve the only subscript notation for global numbering and the superscript-subscript notation for local numbering. Element e_l has four nodal points $n_p^{e_l}$ for $p = 1,\dots,4$ and we denote their spacial coordinates by $\mathbf{x}_p^{e_l} = (x_p^{e_l}, y_p^{e_l}, z_p^{e_l})^T$. Inside the element, the parameters $\alpha,\dots,\delta$ are constant for each $\varphi_p^{e_l}$ and we denote the parameters using $\alpha_p^{e_l},\dots,\delta_p^{e_l}$. For the concentration c_M we introduce a vector $[c_m]$ of length n and we say that the j-th element $[c_m]_j$ coincides with the value of the concentration MMP c_M on the nodal point n_j at location $\mathbf{x}_j$. Since the concentration on the nodal points may change over time, we can write $[c_m] = [c_m](t)$. In local numbering we will denote this as $[c_m]_p^{e_l}$. Note that for the concentration MMP we use c_M with capital M and for the corresponding vector of parameters we use $[c_m]$ with lower case m. We can now approximate the concentration $c_M(\mathbf{x}) \approx \sum_{j=1}^n [c_m]_j \varphi_j(\mathbf{x})$. To conclude, we define

- elements e_l for $l = 1,\dots,n_{el}$;
- using global numbering, nodes n_j for $j = 1,\dots,n$ having spacial coordinates $\mathbf{x}_j = (x_j, y_j, z_j)^T$. We denote possibly different nodes on the global scale with numbers i and j;
- using local numbering, the four vertices $n_p^{e_l}$ of an element e_l for $p = 1,\dots,4$ having spacial coordinates $\mathbf{x}_p^{e_l} = (x_p^{e_l}, y_p^{e_l}, z_p^{e_l})^T$. We denote possibly different nodes on the local scale with numbers p and k
- using global numbering, basis functions $\varphi_j(\mathbf{x}) = \alpha_j + \beta_j x + \gamma_j y + \delta_j z$ on a node n_j such that $\varphi_j(\mathbf{x}_i) = 1$ for $i = j$ and 0 otherwise;
- using local numbering, basis functions $\varphi_p^{e_l}(\mathbf{x}) = \alpha_p^{e_l} + \beta_p^{e_l} x + \gamma_p^{e_l} y + \delta_p^{e_l} z$ on a node $n_p^{e_l}$ such that $\varphi_p^{e_l}(\mathbf{x}_k^{e_l}) = 1$ for $p = k$ and 0 otherwise;
- using global numbering, a vector of parameters $[c_m](t)$ with values $[c_m]_j(t)$ on each node n_j equal to the value of $c_M(\mathbf{x}_j)$ at that nodal point;
- using local numbering, a vector of parameters $[c_m](t)$ with values $[c_m]_p^{e_l}(t)$ on each node $n_p^{e_l}$ equal to the value of $c_M(\mathbf{x}_p^{e_l})$ at that nodal point;
- an approximation $c_M(\mathbf{x}, t) \approx \sum_{j=1}^n [c_m]_j(t) \varphi_j(\mathbf{x})$.
- biological cells numbered $q = 1,\dots,N$.
- the index set of cells θ and the subsets θ_t for tip cells and θ_s for stalk cells.

For notational simplicity, we will often use $[c_v]$ instead of $[c_v](t)$ and φ_j instead of $\varphi_j(\mathbf{x})$. Substituting the approximate form for c_V into the weak formulation in Equation C.1 and choosing $\varphi = \varphi_i$ for $i = 1,\dots,n$ we see

$$\begin{aligned}\int_\Omega \frac{\partial}{\partial t}\left(\sum_{j=1}^n [c_m]_j \varphi_j\right)\varphi_i dV = &-\int_\Omega (\nabla\varphi_i)\cdot(D_M \nabla\left(\sum_{j=1}^n [c_m]_j \varphi_j\right))dV \\ &-\int_\Omega r_M\left(\sum_{j=1}^n [c_m]_j \varphi_j\right) f_B \varphi_i dV + \int_\Omega \sum_{q\in\theta_t} s_M \delta(\mathbf{x}-\mathbf{x}_q) c_V \varphi_i dV \quad \text{for } i = 1,\dots,n.\end{aligned}$$

Changing the order of integration and summation yields a system $M\frac{\partial c_m}{\partial t} + Sc_m = Q$ where the matrix elements M_{ij} and S_{ij} and the vector elements Q_i are given by

$$\sum_{j=1}^n \underbrace{\int_\Omega \varphi_j \varphi_i dV}_{M_{ij}} \frac{\partial [c_m]_j}{\partial t} + \sum_{j=1}^n \underbrace{\int_\Omega D_M \nabla\varphi_i \cdot \nabla\varphi_j + r_M f_B \varphi_i \varphi_j dV}_{S_{ij}} [c_m]_j = \underbrace{\int_\Omega \sum_{q\in\theta_t} s_M \delta(\mathbf{x}-\mathbf{x}_q) c_V \varphi_i dV}_{Q_i} \quad \text{for } i = 1,\dots,n.$$

We calculate the matrix entries M_{ij} and S_{ij} and the vector elements Q_i by splitting up the integrals over all elements, i.e.

$$\begin{aligned}
M_{ij} &= \int_\Omega \varphi_j \varphi_i \, dV && = \sum_{l=1}^{n_{el}} \underbrace{\int_{e_l} \varphi_j \varphi_i \, dV}_{M_{ij}^{e_l}}, \\
S_{ij} &= \int_\Omega D_M \nabla\varphi_i \cdot \nabla\varphi_j + r_M f_B \varphi_i \varphi_j \, dV && = \sum_{l=1}^{n_{el}} \underbrace{\int_{e_l} D_M \nabla\varphi_i \cdot \nabla\varphi_j + r_M f_B \varphi_i \varphi_j \, dV}_{S_{ij}^{e_l}}, \\
Q_i &= \int_\Omega \sum_{q\in\theta_t} s_M \delta(\mathbf{x}-\mathbf{x}_q) c_V \varphi_i \, dV && = \sum_{l=1}^{n_{el}} \underbrace{\int_{e_l} \sum_{q\in\theta_t} s_M \delta(\mathbf{x}-\mathbf{x}_q) c_V \varphi_i \, dV}_{Q_i^{e_l}}.
\end{aligned}$$

C.2. LINEAR BASIS FUNCTIONS

By the nature of the basis functions $\varphi_p^{e_l}$ with $p = 1,\dots,4$ within an element e_l, we know that they must attain values 1 on their corresponding node p and attain values 0 at all other nodes. If we write $\varphi_p^{e_l} = \alpha_p^{e_l} + \beta_p^{e_l} x + \gamma_p^{e_l} y + \delta_p^{e_l} z$ for $p = 1,\dots,4$, we can write these equalities as a system

$$\begin{bmatrix} 1 & x_1^{e_l} & y_1^{e_l} & z_1^{e_l} \\ 1 & x_2^{e_l} & y_2^{e_l} & z_2^{e_l} \\ 1 & x_3^{e_l} & y_3^{e_l} & z_3^{e_l} \\ 1 & x_4^{e_l} & y_4^{e_l} & z_4^{e_l} \end{bmatrix} \begin{bmatrix} \alpha_1^{e_l} & \alpha_2^{e_l} & \alpha_3^{e_l} & \alpha_4^{e_l} \\ \beta_1^{e_l} & \beta_2^{e_l} & \beta_3^{e_l} & \beta_4^{e_l} \\ \gamma_1^{e_l} & \gamma_2^{e_l} & \gamma_3^{e_l} & \gamma_4^{e_l} \\ \delta_1^{e_l} & \delta_2^{e_l} & \delta_3^{e_l} & \delta_4^{e_l} \end{bmatrix} = \begin{bmatrix} 1 & 0 & 0 & 0 \\ 0 & 1 & 0 & 0 \\ 0 & 0 & 1 & 0 \\ 0 & 0 & 0 & 1 \end{bmatrix},$$

and we can solve for our parameters $\alpha_p^{e_l},\dots,\delta_p^{e_l}$ for $p = 1,\dots,4$ by matrix inversion. Since our mesh is constant in time, this can be done once prior to the time stepping.

C.3. (APPROXIMATE) INTEGRATION OVER TETRAHEDRA

For the integrals over tetrahedra involving the basis functions, we use the Holand-Bell integration formulas for linear basis functions over simplices proved in [54]. Each element e_l has four corresponding nodes (vertices), denoted by $n_p^{e_l}$ for $p = 1,\dots,4$. If φ_p are linear basis functions on the nodes $n_p^{e_l}$ of the tetrahedral element e_l (simplex in 3d), then we have the exact integral

$$\int_{e_l} (\varphi_1^{e_l})^a \, (\varphi_2^{e_l})^b \, (\varphi_3^{e_l})^c \, (\varphi_4^{e_l})^d \, dV = \|\Delta\|^{e_l} \frac{a!\, b!\, c!\, d!}{(a+b+c+d+3)!}, \tag{C.2}$$

where $\frac{\|\Delta\|^{e_l}}{6}$ is the volume of the element e_l. We calculate $\|\Delta\|$ using the determinant

$$\|\Delta\|^{e_l} = \begin{vmatrix} 1 & 1 & 1 & 1 \\ x_1^{e_l} & x_2^{e_l} & x_3^{e_l} & x_4^{e_l} \\ y_1^{e_l} & y_2^{e_l} & y_3^{e_l} & y_4^{e_l} \\ z_1^{e_l} & z_2^{e_l} & z_3^{e_l} & z_4^{e_l} \end{vmatrix}. \tag{C.3}$$

Next, we introduce Newton-Cotes integration for approximation of volume integrals of other than basis functions over a tetrahedron e_l. We see

$$\int_{e_l} f(\mathbf{x}) dV \approxeq \frac{\|\Delta\|^{e_l}}{6} \left(\frac{1}{4} \sum_{p=1}^{4} f(\mathbf{x}_p^{e_l}) \right) = \frac{\|\Delta\|}{24} \sum_{p=1}^{4} f(\mathbf{x}_p^{e_l}), \tag{C.4}$$

where equality holds if $f(\mathbf{x})$ is linear.

C.4. BARYCENTRIC COORDINATES, LINEAR INTERPOLATION AND DIRAC DELTA INTEGRATION

Cells secrete the different chemoattractants where they are located. In the numerical model, the chemicals source within an element of the finite element mesh and it is therefore essential to know in which element

e_l a certain cell n is located. Hence, we have to develop a test to see whether a cell is inside a tetrahedron. Furthermore, we would like to easily linearly interpolate in space inside a tetrahedron. Both challenges can be taken care of by introducing barycentric coordinates.

Assume that element e_l has vertices $n_p^{e_l}$ for $p = 1, \ldots, 4$ with Cartesian coordinates $\mathbf{x}_p^{e_l} = (x_p^{e_l}, y_p^{e_l}, z_p^{e_l})^T$ and we have a point $\mathbf{x}_q$ inside the tetrahedron having coordinates $(x_q, y_q, z_q)^T$. To each vertex $p = 1, \ldots, 4$ we associate a parameter $\zeta_p^{e_l}$ such that point $\mathbf{x}_q$ is a linear combination of the vertex coordinates with weight factors $\zeta_p^{e_l}$. Since we only need three points to describe a point in 3D, we furthermore constraint $\zeta_1^{e_l} + \zeta_2^{e_l} + \zeta_3^{e_l} + \zeta_4^{e_l} = 1$. These constraints in matrix form give

$$\begin{bmatrix} 1 \\ x_q \\ y_q \\ z_q \end{bmatrix} = \begin{bmatrix} 1 & 1 & 1 & 1 \\ x_1^{e_l} & x_2^{e_l} & x_3^{e_l} & x_4^{e_l} \\ y_1^{e_l} & y_2^{e_l} & y_3^{e_l} & y_4^{e_l} \\ z_1^{e_l} & z_2^{e_l} & z_3^{e_l} & z_4^{e_l} \end{bmatrix} \begin{bmatrix} \zeta_1^{e_l} \\ \zeta_2^{e_l} \\ \zeta_3^{e_l} \\ \zeta_4^{e_l} \end{bmatrix},$$

and we find the ζ's by explicit inversion. Since for our problem the finite element mesh is constant in time, so is the matrix of node coordinates for each element e_l. It is therefore computationally advantageous to calculate and store the inverses beforehand. Assume we have a function c_V approximated at the vertices $\mathbf{x}_p^{e_l}$ by values $[c_v]_p^{e_l}$. If we have a point $\mathbf{x}_q$ inside e_l and we want to linearly interpolate between the vertices to get the value of c_V at P, we simply take the inner product of the values c_v and the barycentric coordinates, i.e.

$$c_v(P) = \sum_{p=1}^{4} \zeta_p^{e_l} [c_v]_p^{e_l} = \zeta_1^{e_l} [c_v]_1^{e_l} + \zeta_2^{e_l} [c_v]_2^{e_l} + \zeta_3^{e_l} [c_v]_3^{e_l} + \zeta_4^{e_l} [c_v]_4^{e_l}.$$

To check whether a point (e.g. a cell center) is inside an element e_l, we calculate the barycentric coordinates. The point lies inside of the tetrahedron if and only if we have $0 < \zeta_p^{e_l} < 1$ for all p. When the point lies on the boundary of the tetrahedron we have $0 \le \zeta_p^{e_l} \le 1$ for all p and $\zeta_p^{e_l} = 0$ for at least one p. It is therefore sufficient to check whether these conditions apply. Every cell lies within exactly one element, and we begin our search with the elements with the smallest distance between the element center and the cell center.

We finally introduce integration over tetrahedra for integrands involving Dirac delta distributions $\delta(\mathbf{x} - \mathbf{x}_q)$. We know that $\int f(\mathbf{x})\delta(\mathbf{x} - \mathbf{x}_q) d\Omega = f(\mathbf{x}_q)$. For the integrals that contain linear basis functions we see

$$\int_{e_l} \varphi_p^{e_l} \delta(\mathbf{x} - \mathbf{x}_q) dV = \varphi_p^{e_l}(\mathbf{x}_q) = \zeta_p^{e_l}(q),$$

where $\zeta_p^{e_l}$ is the p^{th} barycentric coordinate of the point $\mathbf{x}_q$ whenever $\mathbf{x}_q$ lies within e_l.

C.5. THE ELEMENTS MATRICES AND VECTORS FOR THE PDE OF c_M

We derive approximations for the integrals $M_{ij}^{e_l}$, $S_{ij}^{e_l}$ and $f_i^{e_l}$. We apply Holand-Bell integration (Equation C.2) to $M_{ij}^{e_l}$. We note that, integrating over e_l, we only have non-zero values for $i, j \in \{n_p^{e_l} | p = 1, \ldots, 4\}$ and this entails

$$M_{ij}^{e_l} = \begin{cases} 0 & \text{for } n_i, n_j \notin \{n_p^{e_l} | p = 1, \ldots, 4\}, \\ \frac{\|\Delta\|^{e_l}}{120} & \text{for } p \neq k, \\ \frac{\|\Delta\|^{e_l}}{60} & \text{for } p = k. \end{cases}$$

We now calculate $M_{ij}^{e_l}$ for all $n_i, n_j \in \{n_p^{e_l} | p = 1, \ldots, 4\}$ and we call this M^{e_l}:

$$M^{e_l} = \frac{\|\Delta\|^{e_l}}{120} \begin{bmatrix} 2 & 1 & 1 & 1 \\ 1 & 2 & 1 & 1 \\ 1 & 1 & 2 & 1 \\ 1 & 1 & 1 & 2 \end{bmatrix}. \quad \textit{(Holand-Bell)}$$

Note that M^{e_l} is an $n \times n$ matrix, but only the rows and columns of the nodes $n_p^{e_l}$ corresponding to element e_l are shown here and the rest of the elements are equal zero.

However, we find that the element matrix M^{e_l} derived using Holand-Bell has an unwanted diffusive effect and we calculate the “lumped” mass matrix using Newton-Cotes integration. We note that we introduce an $\mathcal{O}(h^2)$ error using this approximation. This is however acceptable since we have already introduced an $\mathcal{O}(h^2)$ using linear basis functions under the assumption that our solutions are smooth enough. We see

$$M^{e_l} = \frac{\|\Delta\|^{e_l}}{24}\begin{bmatrix} 1 & 0 & 0 & 0 \\ 0 & 1 & 0 & 0 \\ 0 & 0 & 1 & 0 \\ 0 & 0 & 0 & 1 \end{bmatrix}. \quad \textit{(Newton-Cotes)}$$

We approximate $S_{ij}^{e_l}$ by using Newton-Cotes integration (Equation C.4) and Holand-Bell integration (Equation C.2). Since the basis function on node i reads $\varphi_i = \alpha_i + \beta_i x + \gamma_i y + \delta_i z$, we see that $\nabla\varphi_i \cdot \nabla\varphi_j = (\beta_i\beta_j + \gamma_i\gamma_j + \delta_i\delta_j)$. Therefore

$$\begin{aligned}
S_{ij}^{e_l} &= \int_{e_l} D_M \nabla\varphi_i \cdot \nabla\varphi_j + r_M f_B \varphi_i \varphi_j dV, \\
&= \begin{cases} 0 & \text{for } n_i, n_j \notin \{n_p^{e_l} | p = 1, \ldots, 4\} \\ (\beta_p^{e_l}\beta_k^{e_l} + \gamma_p^{e_l}\gamma_k^{e_l} + \delta_p^{e_l}\delta_k^{e_l}) \int_{e_l} D_M dV + r_M \int_{e_l} f_B \varphi_i \varphi_j dV & \text{otherwise} \end{cases} \\
&\approx \begin{cases} 0 & & \text{for } n_i, n_j \notin \{n_p^{e_l} | p = 1, \ldots, 4\} \\ (\beta_p^{e_l}\beta_k^{e_l} + \gamma_p^{e_l}\gamma_k^{e_l} + \delta_p^{e_l}\delta_k^{e_l}) & \frac{\|\Delta\|^{e_l}}{24} \sum_{p=1}^4 D_M(f_F(\mathbf{x}_p^{e_l}), f_B(\mathbf{x}_p^{e_l}), f_E(\mathbf{x}_p^{e_l})) & \text{for } p \neq k, \\ ((\beta_p^{e_l})^2 + (\gamma_p^{e_l})^2 + (\delta_p^{e_l})^2) & \frac{\|\Delta\|^{e_l}}{24} \sum_{p=1}^4 D_M(f_F(\mathbf{x}_p^{e_l}), f_B(\mathbf{x}_p^{e_l}), f_E(\mathbf{x}_p^{e_l})) + r_M \frac{\|\Delta\|^{e_l}}{24} f_B(\mathbf{x}_p^{e_l}) & \text{for } p = k. \end{cases}
\end{aligned}$$

Here, by definition of the parameters for the different chemical variables, we have $f_F(\mathbf{x}_p^{e_l}) = [f_f]_p^{e_l}$, $f_B(\mathbf{x}_p^{e_l}) = [f_b]_p^{e_l}$ and $f_E(\mathbf{x}_p^{e_l}) = [f_e]_p^{e_l}$, hence

$$S_{ij}^{e_l} \approx \begin{cases} 0 & & \text{for } n_i, n_j \notin \{n_p^{e_l} | p = 1, \ldots, 4\} \\ (\beta_p^{e_l}\beta_k^{e_l} + \gamma_p^{e_l}\gamma_k^{e_l} + \delta_p^{e_l}\delta_k^{e_l}) & \frac{\|\Delta\|^{e_l}}{24} \sum_{p=1}^4 D_M([f_f]_p^{e_l}, [f_b]_p^{e_l}, [f_e]_p^{e_l}) & \text{for } p \neq k, \\ ((\beta_p^{e_l})^2 + (\gamma_p^{e_l})^2 + (\delta_p^{e_l})^2) & \frac{\|\Delta\|^{e_l}}{24} \sum_{p=1}^4 D_M([f_f]_p^{e_l}, [f_b]_p^{e_l}, [f_e]_p^{e_l}) + r_M \frac{\|\Delta\|^{e_l}}{24} [f_b]_p^{e_l} & \text{for } p = k. \end{cases}$$

Now, if we define

$$L^{e_l} = \begin{bmatrix} \beta_1^{e_l} & \gamma_1^{e_l} & \delta_1^{e_l} \\ \vdots & \vdots & \vdots \\ \beta_4^{e_l} & \gamma_4^{e_l} & \delta_4^{e_l} \end{bmatrix},$$

then for an element e_l we see that the element matrix becomes

$$S^{e_l} = \frac{\|\Delta\|^{e_l}}{24} \sum_{p=1}^{4} D_M([f_f]_p^{e_l}, [f_b]_p^{e_l}, [f_e]_p^{e_l}) L^{e_l} (L^{e_l})^T + r_M \frac{\|\Delta\|^{e_l}}{24} \begin{bmatrix} [f_b]_1^{e_l} & & \emptyset \\ & \ddots & \\ \emptyset & & [f_b]_4^{e_l} \end{bmatrix}.$$

The mixed terms $[f_f]_p^{e_l}, [f_b]_p^{e_l}, [f_e]_p^{e_l}$ must be taken explicit care of when we try to implement an implicit time stepping scheme. More on this issue will be discussed in Appendix E.1.

We finally calculate the element vector $Q_i^{e_l} = \int_{e_l} \sum_{q \in \theta_t} s_M \delta(\mathbf{x} - \mathbf{x}_q) c_V \varphi_i dV$. We see that the Dirac delta distributions give only non-zero contributions whenever $\mathbf{x}_q \in e_l$

$$\begin{aligned}
Q_i^{e_l} = \int_{e_l} \sum_{q\in\theta_t} s_M \delta(\mathbf{x}-\mathbf{x}_q) c_V \varphi_i \, dV = s_M &\sum_{q\in\theta_t} \int_{e_l} \delta(\mathbf{x}-\mathbf{x}_q) c_V \varphi_i \, dV \\
&= s_M \sum_{q\in\theta_t, \mathbf{x}_q\in e_l} \int_{e_l} \delta(\mathbf{x}-\mathbf{x}_q) c_V \varphi_p^{e_l} \, dV \\
&= s_M \sum_{q\in\theta_t, \mathbf{x}_q\in e_l} c_V(\mathbf{x}_q) \varphi_p^{e_l}(\mathbf{x}_q) \\
&= s_M \sum_{q\in\theta_t, \mathbf{x}_q\in e_l} \left[\sum_{p=1}^{4} [c_v]_p^{e_l} \zeta_p^{e_l}(q) \right] \zeta_p^{e_l}(q).
\end{aligned}$$

Hence the element vector becomes

$$Q^{e_l} = s_M \cdot \sum_{q\in\theta_t, \mathbf{x}_q\in e_l} \left(\left[\sum_{p=1}^{4} [c_v]_p^{e_l} \zeta_p^{e_l}(q) \right] \cdot \begin{bmatrix} \zeta_1^{e_l}(q) \\ \zeta_2^{e_l}(q) \\ \zeta_3^{e_l}(q) \\ \zeta_4^{e_l}(q) \end{bmatrix} \right).$$

In this derivation, we make the assumption that the cell centers do not lie precisely on the boundary between two or more elements, i.e. $\zeta_p^{e_l} = 0$ for some node p in element e_l. If this were to happen, the sourcing from the cell would be added to all elements and we would count the sourcing term multiple times. However, since the boundaries of our elements form a null-set in our domain Ω, the chances of this happening are negligibly small.

C.6. Rest of the element matrices and vectors

Likewise, we derive the elements matrices and vectors for all other equations. We use the same nodal points, hence we have the same basis functions φ_j and the same matrices L. We approximate

$$\begin{aligned}
&c_V \approx \sum_{j=1}^{n} [c_v]_j \varphi_j, \quad && c_D \approx \sum_{j=1}^{n} [c_d]_j \varphi_j, \quad && c_U \approx \sum_{j=1}^{n} [c_u]_j \varphi_j, \quad && c_M \approx \sum_{j=1}^{n} [c_m]_j \varphi_j, \\
&c_F \approx \sum_{j=1}^{n} [c_f]_j \varphi_j, && c_B \approx \sum_{j=1}^{n} [c_b]_j \varphi_j, && c_E \approx \sum_{j=1}^{n} [c_e]_j \varphi_j. &&
\end{aligned}$$

We write $M_V^{e_l}, \ldots, M_E^{e_l}$ and $S_V^{e_l}, \ldots, S_E^{e_l}$ for the element matrices and $Q_V^{e_l}, \ldots, Q_E^{e_l}$ for the element vectors for each variable. Again note that all matrices M^{e_l} and S^{e_l} are $n \times n$ matrices equal zero except for the entries $(n_p^{e_l}, n_k^{e_l})$ for $n, k = 1, \ldots, 4$. The vectors Q^{e_l} are vectors of length n. Hence we derive systems

$$\begin{gathered}
\sum_{l=1}^{n_{el}} M_V^{e_l} \frac{\partial [c_v]}{\partial t} + \sum_{l=1}^{n_{el}} S_V^{e_l} [c_v] = \sum_{l=1}^{n_{el}} Q_V^{e_l}, \\
\vdots \\
\sum_{l=1}^{n_{el}} M_E^{e_l} \frac{\partial [c_e]}{\partial t} + \sum_{l=1}^{n_{el}} S_E^{e_l} [c_e] = \sum_{l=1}^{n_{el}} Q_E^{e_l},
\end{gathered}$$

C.6.1. Element matrices M^{e_l} for the time derivative

M^{e_l} is the same for all PDE's

$$M^{e_l} = \frac{\|\Delta\|^{e_l}}{120} \begin{bmatrix} 2 & 1 & 1 & 1 \\ 1 & 2 & 1 & 1 \\ 1 & 1 & 2 & 1 \\ 1 & 1 & 1 & 2 \end{bmatrix}.$$

C.6.2. Element matrices S^{e_l} for the spacial derivatives

S^{e_l} is different for each PDE:

$$S_V^{e_l} = \frac{\|\Delta\|^{e_l}}{24}\sum_{p=1}^{4} D_V([f_f]_p^{e_l},[f_b]_p^{e_l},[f_e]_p^{e_l})L^{e_l}(L^{e_l})^T \quad + r_V \begin{bmatrix} \sum_{q\in\theta,\mathbf{x}_q\in e_l}\left(\zeta_1^{e_l}(q)\right)^2 & \cdots & \sum_{q\in\theta,\mathbf{x}_q\in e_l}\zeta_1^{e_l}(q)\zeta_4^{e_l}(q) \\ \vdots & \ddots & \vdots \\ \sum_{q\in\theta,\mathbf{x}_q\in e_l}\zeta_4^{e_l}(q)\zeta_1^{e_l}(q) & \cdots & \sum_{q\in\theta,\mathbf{x}_q\in e_l}\left(\zeta_4^{e_l}(q)\right)^2 \end{bmatrix}.$$

$$S_D^{e_l} = \frac{\|\Delta\|^{e_l}}{24}\sum_{p=1}^{4} D_D([f_f]_p^{e_l},[f_b]_p^{e_l},[f_e]_p^{e_l})L^{e_l}(L^{e_l})^T \quad + r_D \begin{bmatrix} \sum_{q\in\theta_s,\mathbf{x}_q\in e_l}\left(\zeta_1^{e_l}(q)\right)^2 & \cdots & \sum_{q\in\theta_s,\mathbf{x}_q\in e_l}\zeta_1^{e_l}(q)\zeta_4^{e_l}(q) \\ \vdots & \ddots & \vdots \\ \sum_{q\in\theta_s,\mathbf{x}_q\in e_l}\zeta_4^{e_l}(q)\zeta_1^{e_l}(q) & \cdots & \sum_{q\in\theta_s,\mathbf{x}_q\in e_l}\left(\zeta_4^{e_l}(q)\right)^2 \end{bmatrix}.$$

$$S_U^{e_l} = \frac{\|\Delta\|^{e_l}}{24}\sum_{p=1}^{4} D_U([f_f]_p^{e_l},[f_b]_p^{e_l},[f_e]_p^{e_l})L^{e_l}(L^{e_l})^T \quad + r_U\frac{\|\Delta\|^{e_l}}{24} \begin{bmatrix} [f_f]_1^{e_l} & & \emptyset \\ & \ddots & \\ \emptyset & & [f_f]_4^{e_l} \end{bmatrix}.$$

$$S_M^{e_l} = \frac{\|\Delta\|^{e_l}}{24}\sum_{p=1}^{4} D_M([f_f]_p^{e_l},[f_b]_p^{e_l},[f_e]_p^{e_l})L^{e_l}(L^{e_l})^T \quad + r_M\frac{\|\Delta\|^{e_l}}{24} \begin{bmatrix} [f_b]_1^{e_l} & & \emptyset \\ & \ddots & \\ \emptyset & & [f_b]_4^{e_l} \end{bmatrix}.$$

$$S_F^{e_l} = \quad + r_F\frac{\|\Delta\|^{e_l}}{24} \begin{bmatrix} [c_u]_1^{e_l} & & \emptyset \\ & \ddots & \\ \emptyset & & [c_u]_4^{e_l} \end{bmatrix}.$$

$$S_B^{e_l} = \quad + r_B\frac{\|\Delta\|^{e_l}}{24} \begin{bmatrix} [c_m]_1^{e_l} & & \emptyset \\ & \ddots & \\ \emptyset & & [c_m]_4^{e_l} \end{bmatrix}.$$

$$S_E^{e_l} = [\emptyset]$$

C.6.3. Element vectors

Q^{e_l} is different for all variables

$$Q_V^{e_l} = [\emptyset],$$

$$Q_D^{e_l} = s_D \cdot \sum_{q\in\theta_t,\mathbf{x}_q\in e_l}\left(\left[\sum_{p=1}^{4}[c_v]_p^{e_l}\zeta_p^{e_l}(q)\right]\cdot\begin{bmatrix}\zeta_1^{e_l}(q)\\ \zeta_2^{e_l}(q)\\ \zeta_3^{e_l}(q)\\ \zeta_4^{e_l}(q)\end{bmatrix}\right),$$

$$Q_U^{e_l} = s_U \cdot \sum_{q\in\theta_t,\mathbf{x}_q\in e_l}\left(\left[\sum_{p=1}^{4}[c_v]_p^{e_l}\zeta_p^{e_l}(q)\right]\cdot\begin{bmatrix}\zeta_1^{e_l}(q)\\ \zeta_2^{e_l}(q)\\ \zeta_3^{e_l}(q)\\ \zeta_4^{e_l}(q)\end{bmatrix}\right),$$

$$Q_M^{e_l} = s_M \cdot \sum_{q\in\theta_t,\mathbf{x}_q\in e_l}\left(\left[\sum_{p=1}^{4}[c_v]_p^{e_l}\zeta_p^{e_l}(q)\right]\cdot\begin{bmatrix}\zeta_1^{e_l}(q)\\ \zeta_2^{e_l}(q)\\ \zeta_3^{e_l}(q)\\ \zeta_4^{e_l}(q)\end{bmatrix}\right),$$

$$Q_F^{e_l} = [\emptyset],$$

$$Q_B^{e_l} = [\emptyset],$$

$$Q_E^{e_l} = -r_F\frac{\|\Delta\|^{e_l}}{24}\begin{bmatrix} [c_u]_1^{e_l} & & \emptyset \\ & \ddots & \\ \emptyset & & [c_u]_4^{e_l} \end{bmatrix}\begin{bmatrix}[f_f]_1^{e_l}\\ \vdots \\ [f_f]_4^{e_l}\end{bmatrix} - r_B\frac{\|\Delta\|^{e_l}}{24}\begin{bmatrix} [c_m]_1^{e_l} & & \emptyset \\ & \ddots & \\ \emptyset & & [c_m]_4^{e_l} \end{bmatrix}\begin{bmatrix}[f_b]_1^{e_l}\\ \vdots \\ [f_b]_4^{e_l}\end{bmatrix}.$$

D

CELL MOVEMENT TIME STEPPING ALGORITHM

Assume at time step k cell i is at location $\mathbf{r}_i^k$. We calculate all parameters and gradients at this location and approximate $\frac{\partial \mathbf{r}_i}{\partial t} \approx \frac{\mathbf{r}_i^{k+1} - \mathbf{r}_i^k}{\Delta t}$. We use this time stepping scheme to predict the new location $\tilde{\mathbf{r}}_i^{k+1}$, i.e.

$$\tilde{\mathbf{r}}_i^{k+1} = \mathbf{r}_i^k + \Delta t \left[\alpha(\mathbf{r}_i^k) M(\mathbf{r}_i^k) \hat{z}(\mathbf{r}_i^k) + \gamma(\mathbf{r}_i^k)(\delta_{i\in\theta_s} \nabla c_D(\mathbf{r}_i^k) + \delta_{i\in\theta_t} \nabla c_V(\mathbf{r}_i^k)) + \lambda(\mathbf{r}_i^k) \nabla \rho_S(\mathbf{r}_i^k) + v_g(\mathbf{r}_i^k) + \frac{\sigma_W}{\sqrt{\Delta t}} N \right],$$

where $N \sim \mathcal{N}(0,1)$. We may now use $\mathbf{r}_i^{k+1} = \tilde{\mathbf{r}}_i^{k+1}$ as the new cell location at time step $k+1$, or we can make use of a predictor-corrector scheme[1]. In order to do so, we calculate all parameters at the predicted location $\tilde{\mathbf{r}}_i^{k+1}$ and take the average values of these predicted parameters and the parameters at the initial location

$$\tilde{\alpha} = \frac{\alpha(\mathbf{r}_i^k) + \alpha(\tilde{\mathbf{r}}_i^{k+1})}{2}, \qquad \tilde{\gamma} = \frac{\gamma(\mathbf{r}_i^k) + \gamma(\tilde{\mathbf{r}}_i^{k+1})}{2}, \qquad \tilde{\lambda} = \frac{\lambda(\mathbf{r}_i^k) + \lambda(\tilde{\mathbf{r}}_i^{k+1})}{2},$$

$$\tilde{v}_g = \frac{v_g(\mathbf{r}_i^k) + v_g(\tilde{\mathbf{r}}_i^{k+1})}{2}, \qquad \tilde{M} = \frac{M(\mathbf{r}_i^k) + M(\tilde{\mathbf{r}}_i^{k+1})}{2}, \qquad \tilde{\hat{z}} = \frac{\hat{z}(\mathbf{r}_i^k) + \hat{z}(\tilde{\mathbf{r}}_i^{k+1})}{2},$$

$$\widetilde{\nabla c}_D = \frac{\nabla c_D(\mathbf{r}_i^k) + \nabla c_D(\tilde{\mathbf{r}}_i^{k+1})}{2}, \qquad \widetilde{\nabla c}_V = \frac{\nabla c_V(\mathbf{r}_i^k) + \nabla c_V(\tilde{\mathbf{r}}_i^{k+1})}{2}, \qquad \widetilde{\nabla \rho}_S = \frac{\nabla \rho_S(\mathbf{r}_i^k) + \nabla \rho_S(\tilde{\mathbf{r}}_i^{k+1})}{2},$$

and calculate

$$\mathbf{r}_i^{k+1} = \mathbf{r}_i^k + \Delta t \left[\tilde{\alpha} \tilde{M} \tilde{\hat{z}} + \tilde{\gamma}(\delta_{i\in\theta_s} \widetilde{\nabla c}_D + \delta_{i\in\theta_t} \widetilde{\nabla c}_V) + \tilde{\lambda} \widetilde{\nabla \rho}_S + \tilde{v}_g + \frac{\sigma_W}{\sqrt{\Delta t}} N \right]. \tag{D.1}$$

Especially in the first time steps, one can notice differences between the predictor displacement and the corrector displacement. This is due to the fact that initially gravity and contact mechanics are dominant over the other forces. After the formation of a confluent mono-layer of cells, these forces decrease in magnitude and we notice that the predictor and corrector displacements are almost equal.[2]

Since the magnitude of the cell movements can change drastically over time, we implement a variable time stepping scheme. We want to limit the maximal displacement of cells in a time step to a certain maximum $\hat{d}_{\max}$. We use the maximal displacement of all cells in the last time step $k-1$ to k to determine the Δt in the next time step from k to $k+1$. Assume that for time step $k-1$ to k we have Δt^{k-1} and define the maximal displacement as $d_{\max}^{k-1} = \max_{i\in\theta}\{\|\mathbf{r}_i^k - \mathbf{r}_i^{k-1}\|\}$. Then for time step k to $k+1$ we raise Δt by a factor 1.2 whenever the maximal displacement is a factor 1.2 below the threshold and lower Δt whenever the maximal displacement is above the threshold. I.e.

---

[1] In our computational model, the option `g.cell0.displacementCorrector` is used to implement this predictor-corrector scheme.

[2] In our computational model, the option `g.plot.plotMovements` is used to plot the predictor and corrector movements.

$$\Delta\hat{t}^k = \begin{cases} 1.2\cdot\Delta t^{k-1} & \text{for } d^k_{\max} < \frac{1}{1.2}\cdot\hat{d}_{\max}, \\ \frac{1}{1.2}\cdot\Delta t^{k-1} & \text{for } d^k_{\max} > \qquad \hat{d}_{\max}, \\ \Delta t^{k-1} & \text{otherwise.} \end{cases}$$

We furthermore set a hard minimal and maximal permitted time step $\Delta t_{\min}$ and $\Delta t_{\max}$ and set

$$\Delta t^k = \min\{\max\{\Delta\hat{t}^k, \Delta t_{\min}\}, \Delta t_{\max}\},$$

and we replace Δt in Equation D.1 with Δt^k.

Numerically, the gradient of a concentration is easily calculated using the basis functions of our FEM. We refer the reader to Appendix C for a detailed description and further notes on used notation. We know that within an element $c_V \approx \sum_{p=1}^4 c_v(n_p^{e_l})\varphi_p^{e_l}$ where $\varphi_p^{e_l} = \alpha_p^{e_l} + \beta_p^{e_l} x + \gamma_p^{e_l} y + \delta_p^{e_l} z$ are basis functions. The gradient is then given by $\nabla c_V \approx \nabla \sum_{p=1}^4 c_v(n_p^{e_l})\varphi_p^{e_l} = \sum_{p=1}^4 c_v(n_p^{e_l})\nabla\varphi_p^{e_l}$ and hence

$$\nabla c_V \approx \left(\sum_{p=1}^{4} c_V(n_p^{e_l})\right)\begin{bmatrix} \beta_p^{e_l} \\ \gamma_p^{e_l} \\ \delta_p^{e_l} \end{bmatrix}.$$

E

Numerical Considerations

E.1. Implicit/Explicit (IMEX) time stepping for PDEs

We now approximate the time derivative for the equation for variable $[c_m]$ at time step $k+1$ by a Euler backward discretization $\frac{\partial[c_m]}{\partial t} \approx \frac{[c_m]^{k+1}-[c_m]^k}{\Delta t_k}$, for a time step Δt_k, possibly depending on the time step. We begin with the original system

$$M_M \frac{\partial[c_m]}{\partial t} + S_M[c_m] = Q_M,$$

which is integrated by

$$M_M \frac{[c_m]^{k+1} - [c_m]^k}{\Delta t^k} + S[c_m]^{k+1} = Q_M,$$

and gives

$$(M_M + \Delta t^k S_M)[c_m]^{k+1} = M_M[c_m]^k + \Delta t^k Q_M,$$

and can be rewritten to

$$[c_m]^{k+1} = (M_M + \Delta t^k S_M)^{-1}(M_M[c_m]^k + \Delta t^k Q_M).$$

We would have liked to conclude that we have derived a fully implicit scheme. However, there are explicit terms coming from the cross terms in the reactive parts in the matrices S and in the vectors Q_D, Q_U, Q_M and Q_E. Furthermore, the diffusive functions and the indicator functions make the matrices S and the vectors Q time dependent. Fortunately, because both M and S are symmetric and non-diagonal, inverting $(M+\Delta t S)$ is not computationally harder than inverting M as we would have to do in the explicit scheme.

We have to take special care when assembling the element vector Q_E. We want to maintain conservation of mass and therefore the amount of Fibrin and BM dissolving must be added to the ECF. The amount of fibrin dissolving at time step $k+1$ in element e_l is equal to

$$r_F \frac{\|\Delta\|^{e_l}}{24} \begin{bmatrix} ([c_u]_1^{e_l})^k & & \emptyset \\ & \ddots & \\ \emptyset & & ([c_u]_4^{e_l})^k \end{bmatrix} \begin{bmatrix} ([f_f]_1^{e_l})^{k+1} \\ \vdots \\ ([f_f]_4^{e_l})^{k+1} \end{bmatrix} = r_F \frac{\|\Delta\|^{e_l}}{24} \begin{bmatrix} ([c_u]_1^{e_l})^k([f_f]_1^{e_l})^{k+1} \\ \vdots \\ ([c_u]_4^{e_l})^k([f_f]_4^{e_l})^{k+1} \end{bmatrix},$$

and we have a similar relation for the reaction of the BM. This together constitutes for the element vector for the ECF $Q_E^{e_l}$:

$$Q_E^{e_l} = -r_F \frac{\|\Delta\|^{e_l}}{24} \begin{bmatrix} ([c_u]_1^{e_l})^k([f_f]_1^{e_l})^{k+1} \\ \vdots \\ ([c_u]_4^{e_l})^k([f_f]_4^{e_l})^{k+1} \end{bmatrix} - r_B \frac{\|\Delta\|^{e_l}}{24} \begin{bmatrix} ([c_m]_1^{e_l})^k([f_b]_1^{e_l})^{k+1} \\ \vdots \\ ([c_m]_4^{e_l})^k([f_b]_4^{e_l})^{k+1} \end{bmatrix}.$$

Note that the signs change due to the fact that the source terms Q_E are on the right hand side of the equation whilst the reactive counterparts are on the left hand side.

E.2. MESHING AND NODE NUMBERING

For the 3D mesh generation we use an open source application ISO2Mesh created by Fang and Boas [55]. The domain used is given by the parameters in Table 4.1 and the result is depicted in Figure E.1. To gain extra computational speed, we use Cuthill-McKee bandwith reduction[1] [56] for our node ordering built into MATLAB by the function `symrcm`. The results of the bandwidth reduction can be seen in Figure E.2.

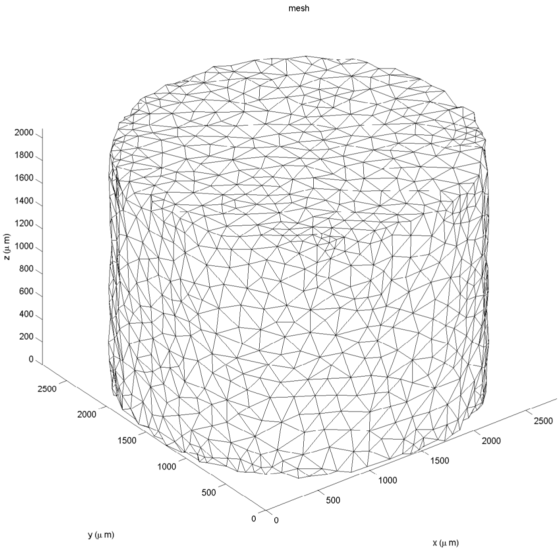

Figure E.1: Meshed domain by the ISO2Mesh mesh generator written by Fang and Boas [55].

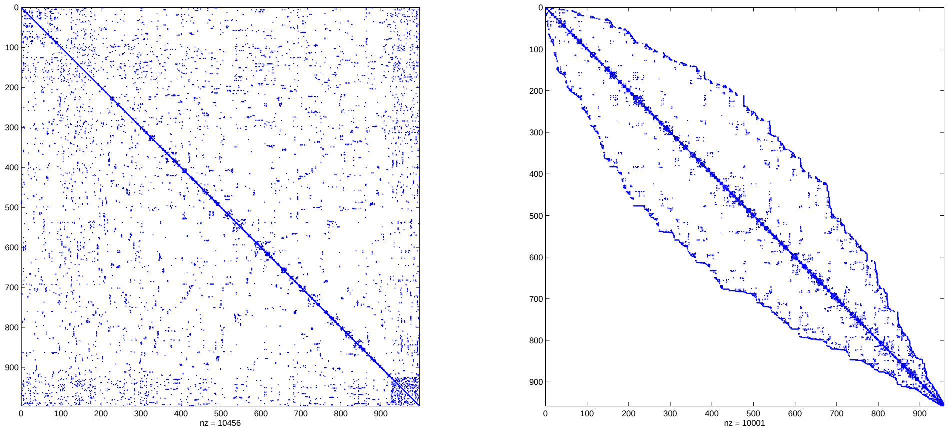

Figure E.2: Spy plots for our mass matrix M. The left figure is in default node order, the right figure numbered the nodes using Cuthill-McKee numbering and we see a reduction in the matrix bandwidth. Computational time reduced from 160 seconds to 140 seconds.

---

[1] In the computational model, the option of Cuthill McKee numbering can be used by setting `g.num.CuthillMckee` = 1.

E.3. TRUNCATION VERY LOW SUBSTRATE DENSITIES

Due to the exponential decaying behavior of the fibrin and the boundary membrane, the fractions f_F and f_B can become very close to 0, causing numerical errors in the calculation of the fraction in Equation 4.12. Therefore, we use a threshold[2] f_0 and say that fractions f_F and f_B passing below the threshold are truncated towards 0 in favor of the fraction f_E. It is hard to find any references on what a physically sensible value for f_0 should be, so we empirically set $f_0 = 10^{-4}$.

E.4. SPURIOUS OSCILLATIONS ON SOURCE TERMS USING HOLAND-BELL

In our 3D setting, we witness oscillation behavior of the solution around point sources, even when we do not take the diffusive and reactive terms into account. We investigate this behavior by examining the 1D situation. Consider the concentration c with initial condition $c_0(x) = 0$ on every node $j = 1, \dots, n$ of a 1D domain. The nodes divide the domain into $l = 1, \dots, (n-1)$ elements of width $\|\Delta\| = h$. We model the time dependent differential equation with point source at rate s at x_q in the middle of element e_k for which we have the weak form

$$\int \frac{\partial c}{\partial t} \varphi dV = S\varphi(x_q).$$

The analytical solution is $c(x,t) = St\delta(x - x_q) + c_0(x) = St\delta(x - x_q)$ and we do not expect any oscillating or diffusive solution. Approximating $c(t,x) = \sum_{j=1}^{n} c_j \varphi_j(x)$, the Galerkin equations for this PDE are

$$\sum_{j=1}^{n} \int \varphi_i \varphi_j dV \frac{\partial c}{\partial t} = \int S\delta(x - x_q)\varphi_i dV, \quad \text{for } i = 1, \dots, n.$$

Assuming $x_q = \frac{x_k + x_{k+1}}{2}$, this gives rise to a system $Mc' = Q$ with

$$M = \frac{h}{6}\begin{bmatrix} 2 & 1 & & & & & \\ 1 & 4 & 1 & & & & \\ & & & & & & \\ & 1 & 4 & \ddots & & & \\ & & \ddots & \ddots & 1 & & \\ & & & 1 & 4 & 1 & \\ & & & & 1 & 4 & 1 \\ & & & & & 1 & 2 \end{bmatrix} \quad \text{and} \quad Q = s\begin{array}{c} \begin{bmatrix} \\ \emptyset \\ \\ \frac{1}{2} \\ \frac{1}{2} \\ \\ \emptyset \\ \\ \end{bmatrix} \end{array} \begin{array}{l} \\ \\ \\ \leftarrow k^{th} \\ \leftarrow (k+1)^{th}. \\ \\ \\ \\ \end{array}$$

Time stepping gives the iterative scheme $c^{k+1} = M^-1(Mc^k + \Delta t Q)$. We simulate $n = 100$ nodes, sourcing in element $k = 50$, grid width $h = 0.05$, sourcing at rate $S = 1$ and time step $\Delta t = 0.1$. We also use Newton-Cotes integration on the element matrix $M_{ij}^{e_l}$ to derive the 'lumped' matrix M^{lumped}:

$$M^{\text{lumped}} = \frac{h}{6}\begin{bmatrix} 3 & & & & & & \\ & 6 & & & & & \\ & & 6 & & & & \\ & & & \ddots & & & \\ & & & & 6 & & \\ & & & & & 6 & \\ & & & & & & 3 \end{bmatrix},$$

and we perform the time stepping with this matrix too. The results after 3.6 seconds is given in Figure E.3. We clearly see the unwanted spurious oscillations using the Holand-Bell integration. This effect is occurs for every size of the time step and the grid width. As expected, the lumped matrix does not have the spurious oscillations since it has identity support[3]. In the following chapter, we will show that the oscillations are independent of the problem and the time step. We therefore use the lumped mass matrix.

---

[2] In our computational model, the option of truncating small substrate fractions is used by setting `g.chem0.truncateSubstrate` = 1.

[3] In our computational model, the option of "lumping" the mass matrix M can be used by setting `g.num.lumped` = 1.

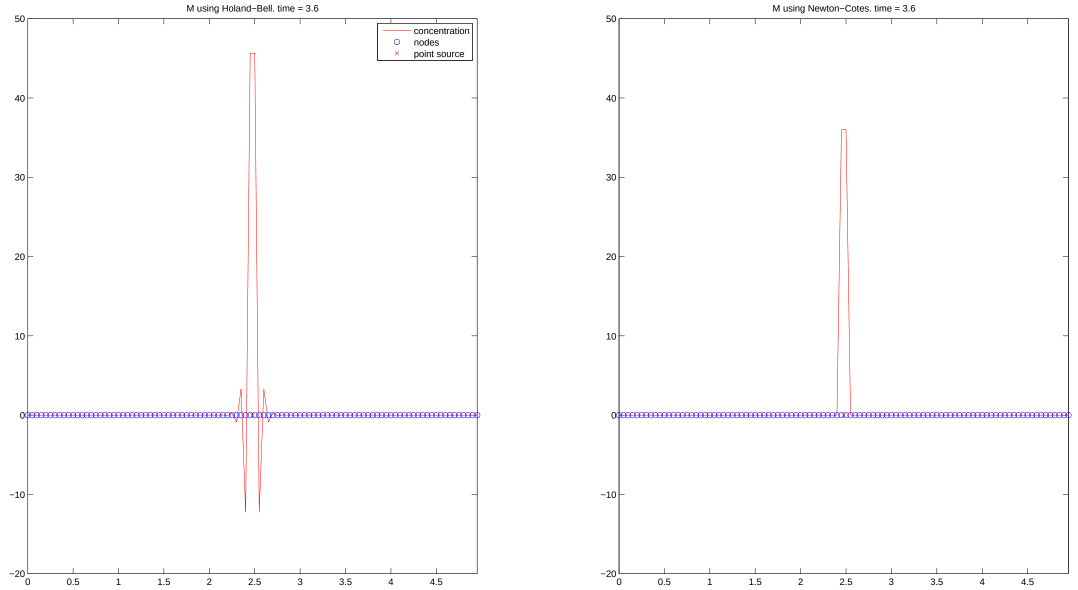

Figure E.3: Spurious oscillations using Holand-Bell (left) integration on mass matrix M. Oscillations do not occur for Newton-Cotes (right) integration.

E.4.1. Proof existence time step and grid size independent spurious oscillations in 1D

Consider a 1D FEM discretization with constant grid width h, nodes $j = 1,\dots,n$ and a concentration c with zero initial condition. Let us first consider the discretized equations without a diffusive term and a point source with rate $s > 0$ precisely on the first node, i.e. $Mc' = Q$ with

$$M = \frac{h}{6}\begin{bmatrix} 2 & 1 & & & & & \\ 1 & 4 & 1 & & & & \\ & 1 & 4 & \ddots & & & \\ & & \ddots & \ddots & 1 & & \\ & & & 1 & 4 & 1 & \\ & & & & 1 & 4 & 1 \\ & & & & & 1 & 2 \end{bmatrix} \quad \text{and} \quad Q = S\begin{bmatrix} 1 \\ \\ 0 \\ \\ \end{bmatrix}.$$

We discretize in time to get $Mc^{k+1} = Mc^k + \Delta t Q, i.e.$

$$\frac{h}{6}\begin{bmatrix} 2 & 1 & & & & & \\ 1 & 4 & 1 & & & & \\ & 1 & 4 & \ddots & & & \\ & & \ddots & \ddots & 1 & & \\ & & & 1 & 4 & 1 & \\ & & & & 1 & 4 & 1 \\ & & & & & 1 & 2 \end{bmatrix}\begin{bmatrix} c_1^{k+1} \\ \\ \vdots \\ \\ c_n^{k+1} \end{bmatrix} = \frac{h}{6}\begin{bmatrix} 2 & 1 & & & & & \\ 1 & 4 & 1 & & & & \\ & 1 & 4 & \ddots & & & \\ & & \ddots & \ddots & 1 & & \\ & & & 1 & 4 & 1 & \\ & & & & 1 & 4 & 1 \\ & & & & & 1 & 2 \end{bmatrix}\begin{bmatrix} c_1^{k} \\ \\ \vdots \\ \\ c_n^{k} \end{bmatrix} + \Delta t S \begin{bmatrix} 1 \\ \\ 0 \\ \\ \end{bmatrix}. \tag{E.1}$$

We now prove by induction over the time steps $k = 0,\dots,t_{\text{end}}$ that we have a oscillating solution over the nodes for every time step. First consider the time step from $k = 0$ to $k = 1$. Since we have a zero initial condition, this time step reduces to $Mc^{k+1} = \Delta t Q$. The first equation in this system is

$$\frac{h}{6}(2c_1^1 + c_2^1) = \Delta t S.$$

As an Ansatz, we look for solutions that satisfy the recursive relation

$$c^1_{j+1} = \alpha c^1_j. \tag{E.2}$$

Then we have

$$\frac{h}{6}(2c^1_1 + \alpha c^1_1) = \Delta t S,$$

and

$$c^1_1 = \frac{6\Delta t s}{h(2+\alpha)} := B.$$

The j^{th} ($j \neq 1, j \neq n$) equation of the this system is

$$\frac{h}{6}(c^1_{j-1} + 4c^1_j + c^1_{j+1}) = 0.$$

Substituting the recursive relation from Equation E.2 we see

$$\frac{h}{6}(c^1_{j-1} + 4\alpha c^1_{j-1} + \alpha^2 c^1_{j-1}) = 0,$$

and we have

$$\frac{h}{6}(1 + 4\alpha + \alpha^2)c^1_{j-1} = 0.$$

For a non-trivial solution we must have $1+4\alpha+\alpha^2 = 0$ and hence $\alpha_{1,2} = -2 \pm \sqrt{3}$. Both values of α are negative, so we have an oscillating solution. Only $\alpha_1 = -2+\sqrt{3}$ satisfies $-1 \leq \alpha \leq 1$, which constitutes damping. The value $\alpha = -2-\sqrt{3}$ would constitute a negative value for B, entailing that the response in concentration to positive sourcing would be negative. So we choose $\alpha = -2+\sqrt{3}$ and we see that $B = \frac{6\Delta t S}{h\sqrt{3}} = \frac{2\sqrt{3}\Delta t S}{h}$. We now have a recursive relation for time step $k = 1$, i.e. $c^1_{j+1} = \alpha c^1_j$ with initial condition $c^1_1 = B$. This entails a direct relation $c^1_j = B(\alpha)^{j-1}$ that forms an oscillating solution c at time step 1. Since the solution to the system must be unique, the Ansatz in Equation E.2 must indeed hold.

Now assume (induction assumption) at time step k we have a direct relation for the solution of $c^k_j = kB(-\alpha)^{j-1}$. The first equation in the system from time step $t = k$ to $t = k+1$ is

$$\frac{h}{6}\begin{bmatrix} 2 & 1 & & & & & \\ 1 & 4 & 1 & & & & \\ & 1 & 4 & \ddots & & & \\ & & \ddots & \ddots & 1 & & \\ & & & 1 & 4 & 1 & \\ & & & & 1 & 4 & 1 \\ & & & & & 1 & 2 \end{bmatrix}\begin{bmatrix} c^{k+1}_1 \\ \\ \vdots \\ \\ c^{k+1}_n \end{bmatrix} = \frac{h}{6}\begin{bmatrix} 2 & 1 & & & & & \\ 1 & 4 & 1 & & & & \\ & 1 & 4 & \ddots & & & \\ & & \ddots & \ddots & 1 & & \\ & & & 1 & 4 & 1 & \\ & & & & 1 & 4 & 1 \\ & & & & & 1 & 2 \end{bmatrix}\begin{bmatrix} kB \\ \\ \vdots \\ \\ kB(-\alpha)^{n-1} \end{bmatrix} + \Delta t S \begin{bmatrix} 1 \\ \\ \emptyset \\ \\ \end{bmatrix}.$$

We again assume an oscillating recursive relation

$$0 < \beta < 1 \quad \text{such that} \quad c^{k+1}_{j+1} = -\beta c^{k+1}_j. \tag{E.3}$$

We would like to show that the factor $\beta = \alpha$ and that $c^{k+1}_j = (k+1)B(-\alpha)^{j-1}$. The first equation in the system is

$$\frac{h}{6}(2c^{k+1}_1 + c^{k+1}_2) = \frac{h}{6}(2kB - kB\alpha) + \Delta t S.$$

Substituting the recursive relation from equation E.3 gives

$$\frac{h}{6}(2c^{k+1}_1 - \beta c^{k+1}_1) = \frac{h}{6}(2kB - kB\alpha) + \Delta t S,$$

and we have

$$c_1^{k+1} = kB\frac{2-\alpha}{2-\beta} + \frac{6\Delta t S}{h(2-\beta)}. \tag{E.4}$$

The j^{th} equation ($j \neq 1, j \neq n$) of the system is

$$\begin{aligned}
\frac{h}{6}(c_{j-1}^{k+1} + 4c_j^{k+16} + c_{j+1}^{k+1}) &= \frac{h}{6}(kB(-\alpha)^{j-2} + 4kB(-\alpha)^{j-1} + kB(-\alpha)^{j}) \\
\frac{h}{6}(c_{j-1}^{k+1} - 4\beta c_{j-1}^{k+1} + \beta^2 c_{j-1}^{k+1}) &= \frac{h}{6}kB(-\alpha)^{j-2}(1-4\alpha+\alpha^2) \\
\frac{h}{6}(1-4\beta+\beta^2)c_{j-1}^{k+1} &= 0,
\end{aligned}$$

since $(1-4\alpha+\alpha^2) = 0$ by choice of α. Hence, for non-trivial c^{k+1} we must have $\beta = 2-\sqrt{3} = \alpha$. Then Equation E.4 reduces to

$$\begin{aligned}
c_1^{k+1} &= kB\frac{2-\alpha}{2-\alpha} + \frac{6\Delta t S}{h(2-\alpha)} \\
&= kB + B \\
&= (k+1)B,
\end{aligned}$$

and the recursive relation for c^{k+1} reads $c_{j+1}^{k+1} = -\alpha c_j^{k+1}$ with $c_1^{k+1} = (k+1)B = \frac{6(k+1)\Delta t S}{h(2-\alpha)}$. This proves by recursion that that for every time step k we have an oscillating decaying solution characterized by the function value at the source location and a fixed decay rate $-\alpha$. Furthermore, the rate α only depends on the structure of the mass matrix M and not on the time step of grid width.

E.4.2. ADDING DIFFUSION TO SMEAR OUT THE OSCILLATIONS

If we add a diffusive term

$$\frac{\partial c}{\partial t} - D\nabla^2 c = Q,$$

we end up with a system $Mc' + Sc = f$, leading to the implicit time stepping scheme $(M + \Delta t S)c^{k+1} = Mc^k + \Delta t f$, with the same matrix M and the same vector f. S becomes

$$S = \frac{D}{h}\begin{bmatrix}
1 & -1 & & & & & \\
-1 & 2 & -1 & & & & \\
 & -1 & 2 & \ddots & & & \\
 & & \ddots & \ddots & -1 & & \\
 & & & -1 & 2 & -1 & \\
 & & & & -1 & 2 & -1 \\
 & & & & & -1 & 1
\end{bmatrix}.$$

We know that we cancel the spurious oscillations whenever matrix $(M+\Delta t S)$ is a diagonal dominant Z-matrix. We see

$$(M+\Delta t S) = \frac{1}{6h}\begin{bmatrix}
(2h^2+6\Delta t D) & (h^2-6\Delta t D) & & & & \\
(h^2-6\Delta t D) & (4h^2+12\Delta t D) & (h^2-6\Delta t D) & & & \\
 & (h^2-6\Delta t D) & \ddots & \ddots & & \\
 & & \ddots & \ddots & (h^2-6\Delta t D) & \\
 & & & (h^2-6\Delta t D) & (4h^2+12\Delta t D) & (h^2-6\Delta t D) \\
 & & & & (h^2-6\Delta t D) & (2h^2+6\Delta t D)
\end{bmatrix}.$$

For sure, diagonal dominance is fine. $(M+\Delta t X)$ becomes a Z-matrix whenever all non-diagonal elements are negative. This is the case whenever $\frac{h}{6} < \frac{\Delta t D}{h}$, i.e. $\frac{6\Delta t D}{h^2} > 1$. We expect that a similar stability relation $M\frac{\Delta t D}{h^2} > 1$ holds in the 3-d setting where h is the radius of the elements and $M \in \mathbb{R}$ is some factor.

E.4.3. COMPENSATING THE SPURIOUS OSCILLATIONS BY OTHER NUMERICAL SCHEMES

John et al. [57] and Fries et al. [58] describe the Streamline Upwind/Petrov Galerkin (SUPG) method. The method introduces a certain amount of artificial diffusion in streamline direction only of which the amount is controlled by a variable θ. Much research has been devoted to finding suitable values, but no general method to find the optimum exists. John [57] also describes various Spurious Oscillations at Layers Diminishing (SOLD) methods and compares them. SOLD methods add another stabilization term to the SUPG method to reduce its spurious oscillations. Most commonly, this is an anisotropic diffusion term. At last, John et al. [59] give an overview of finite element methods for solving time dependent 3D convection-diffusion-reaction equations. They focus on the effect of spurious oscillations in the computed solutions. They compare a SUPG scheme with two choices of SOLD schemes and two variants of a Finite Element Method Flux–Corrected–Transport (FEM–FCT) scheme. They conclude that, both for damping spurious oscillations, as well as for computational time, it is best to use a FEM-FCT scheme, either the linear or the non-linear variant. All these schemes however are used to damp oscillations in advection dominated flow problems. We however do not have an advective term and hence this does not seem suitable for our problem.

E.5. ON THE EQUILIBRIUM POINTS AND STABILITY OF THE PDES

We try to find stable solutions of the system of Equations 4.1 - 4.7. We start with the substrate fractions. From Equation 4.5 we see that $\frac{\partial f_F}{\partial t} = 0$ only if $f_F = 0$ or $c_U = 0$. From Equation 4.6 we see that $\frac{\partial f_B}{\partial t} = 0$ only if $f_B = 0$ or $c_M = 0$. Whenever we have these two equations stable, Equation 4.7 is automatically stable. This means that in equilibrium, the substrate if fully vanished and we have $f_F = f_B = 0$ and $f_E = 1$ (by initial condition), or we have a non-trivial equilibrium substrate together with $c_U = c_M = 0$. In practice this entails we have no proteases to degrade the substrate.

The case for a non-trivial equilibrium substrate gives a trivial solution for the chemicals. If $c_U = 0$, than in Equation 4.3 we also have $\frac{\partial c_U}{\partial t} = 0$, $\nabla^2 c_U = 0$ and the reactive term vanishes, leaving us with

$$0 = \sum_{q \in \theta_t} s_U \delta(\mathbf{x} - \mathbf{x}_q) c_V.$$

This must hold for all possible cell positions $\mathbf{x}_q$ and we must have $c_V = 0$. The same holds for Equation 4.4. Since $c_V = 0$, Equation 4.1 is automatically stable. This leaves us with the reduced version of Equation 4.2. This equation is only stationary whenever $\frac{\partial c_D}{\partial t} = 0$ and we must have

$$\nabla \cdot [D_D(f_F, f_B, f_E) \nabla c_D] = \sum_{q \in \theta_s} r_D c_D \delta(\mathbf{x} - \mathbf{x}_q). \tag{E.5}$$

Only the trivial solution $c_D = 0$ satisfies this relation. We can see this by integrating over the left hand and use Greens divergence theorem and integrating over the right hand side and applying the definition of the Dirac distribution.

Next we consider the the stationary substrate solution $f_F = f_B = 0$ and $f_E = 1$. The diffusive functions reduce to $D_D(0,0,1) = D_D \cdot D_E$ and the reactive terms in Equations 4.3 and 4.4 drop out. The system for our four chemicals, with the time derivative set to zero in order to find stationary solutions, reduces to

$$\begin{aligned}
0 &= D_V D_E \nabla^2 c_V && - \sum_{q \in \theta} r_V c_V \delta(\mathbf{x} - \mathbf{x}_q), && \\
0 &= D_D D_E \nabla^2 c_D && - \sum_{q \in \theta_s} r_D c_D \delta(\mathbf{x} - \mathbf{x}_q) && + \sum_{q \in \theta_t} s_D \delta(\mathbf{x} - \mathbf{x}_q) c_V, \\
0 &= D_U D_E \nabla^2 c_U && && + \sum_{q \in \theta_t} s_U \delta(\mathbf{x} - \mathbf{x}_q) c_V, \\
0 &= D_M D_E \nabla^2 c_M && && + \sum_{q \in \theta_t} s_M \delta(\mathbf{x} - \mathbf{x}_q) c_V.
\end{aligned}$$

Following the same reasoning as in Equation E.5, we see that $c_V = 0$ and all the source terms drop out. The equation for c_D reduces to the form we just encountered for c_V and we conclude that $c_D = 0$. The equation for c_U and c_M reduce to $D_U D_E \nabla^2 c_U = 0$ and $D_M D_E \nabla^2 c_M = 0$, which have linear functions as solutions. Our no-flux boundary conditions dictate that this solution must be a constant.

Having our stationary point, we can linearize around it and we see that we can write the equation for the concentration VEGF as

$$\frac{\partial c_V}{\partial t} + Lc_V = 0,$$

with $L = -D_V D_E \nabla^2 + \sum_{q\in\theta} r_V \delta(\mathbf{x} - \mathbf{x}_q)$. Since all our concentrations c_V take real values, self-adjointness of the operator L is almost trivial. Positive definiteness is proven when we see

$$\begin{aligned}
< Lc_V, c_V >= \int_\Omega L(c_V) c_V dV = & \quad -D_V D_E \int_\Omega (\nabla^2 c) c dV + \int_\Omega \sum_{q\in\theta} r_V \delta(\mathbf{x} - \mathbf{x}_q) c_V^2 dV \\
= & \quad -D_V D_E \int_\Omega \nabla \cdot (c\nabla c) dV + D_V D_E \int_\Omega (\nabla c)^2 dV + \sum_{q\in\theta} r_V c_V (\mathbf{x}_q)^2 \\
= & \quad -D_V D_E \int_\Gamma c\nabla c \cdot n \, d_V + D_V D_E \int_\Omega (\nabla c)^2 dV + \sum_{q\in\theta} r_V c_V (\mathbf{x}_q)^2 \\
= & \quad 0 + D_V D_E \int_\Omega (\nabla c)^2 dV + \sum_{q\in\theta} r_V c_V (\mathbf{x}_q)^2 > 0.
\end{aligned}$$

This together makes the equation stationary point stable. The same analysis holds for the other equations. All this makes physical sense. If our entire substrate is degraded and all the initially present VEGF is consumed by the cells, the sourcing of the three other chemicals will stop. DLL4 will be consumed by the cells and the “left over” uPA and MMP will smear out over the entire domain.

F

COMPUTATIONAL MODEL OPTIONS

Numerical parameters

Parameter	Code name	Value
Time step	`g.num.dt`	1
Final time	`g.num.finalTime`	48*3600
Maximal element radius	`g.num.maxVolSize`	[2.5 - 3.0]
Number of points in domain model	`g.num.nx`	100
Use Cuthill-Mckee numbering	`g.num.CuthillMckee`	boolean
Use lumped mass matrix	`g.num.lumped`	boolean
Print execution time per time step	`g.num.timeKeeping`	boolean
Print all parameters	`g.num.plotParams`	boolean

Plotting output parameters

Parameter	Code name	Value
The type of plot wanted	`g.plot.plotType`	[1 - 10]
Resolution of the structured grid	`g.plot.resolution`	[20 - 30]
Plot quivers in movement directions	`g.plot.quiverOn`	boolean
Plot histograms of motilities	`g.plot.plotMovements`	boolean
Plot frame every so many time steps	`g.plot.plotInterval`	[1,2,...]
Figure number main plot	`g.plot.fig`	1

Video output parameters

Parameter	Code name	Value
Store plotted frames as video file	`g.vid.movieOn`	boolean
Number of frames per second	`g.vid.fps`	24
Duration of the video	`g.vid.length`	60
Use transcoder to convert ras video	`g.vid.transcode`	boolean
Keep raw video after transcoding	`g.vid.keepOriginal`	boolean

Chemical simulation options

Parameter	Code name	Value
Include diffusive terms in PDEs	`g.chemO.difusionOn`	boolean
Include reactive terms in PDEs	`g.chemO.reactionOn`	boolean
Include sourcing terms in PDEs	`g.chemO.sourcingOn`	boolean
Use non-linear diffusion functions	`g.chemO.nonLinearDiffusion`	boolean
Truncate low substrate fractions	`g.chemO.truncateSubstrate`	boolean

Cell movement and initial distribution options

Parameter	**Code name**	**Value**
Use predictor-corrector scheme	`g.cell0.displacementCorrector`	boolean
Include haptotactic movement	`g.cell0.haptotaxisOn`	boolean
Include chemotactic movement	`g.cell0.chemotaxisOn`	boolean
Include movement due to gravity	`g.cell0.gravityOn`	boolean
Include cell-matrix adhesion	`g.cell0.celMatrixAdhesionOn`	boolean
Include stochastic movement	`g.cell0.stochasticOn`	boolean
Use stochastic cell differentiation	`g.cell0.cellDifferentiation`	boolean
Use random layer as initial distribution	`g.cell0.randomLayer`	boolean
Use structured monolayer as initial distribution	`g.cell0.monoLayer`	boolean
Dissolve cells in ECF as initial distribution	`g.cell0.suspended`	boolean
Use a test case with 2 cells	`g.cell0.twoCells`	boolean
Use a test case with 4 cells	`g.cell0.fourCells`	boolean
Use a test case with 8 cells	`g.cell0.eightCells`	boolean

BIBLIOGRAPHY

[1] P. Carmeliet *et al.*, *Mechanisms of angiogenesis and arteriogenesis,* Nature medicine **6**, 389 (2000).

[2] H. Rossiter, C. Barresi, J. Pammer, M. Rendl, J. Haigh, E. F. Wagner, and E. Tschachler, *Loss of vascular endothelial growth factor a activity in murine epidermal keratinocytes delays wound healing and inhibits tumor formation,* Cancer research **64**, 3508 (2004).

[3] F. m. c. Graner and J. A. Glazier, *Simulation of biological cell sorting using a two-dimensional extended potts model,* Physical Review Letters **69**, 2013 (1992).

[4] J. A. Glazier and F. Graner, *Simulation of the differential adhesion driven rearrangement of biological cells,* Physical Review E **47**, 2128 (1993).

[5] R. M. Merks, S. A. Newman, and J. A. Glazier, *Cell-oriented modeling of in vitro capillary development,* in *Cellular Automata* (Springer, 2004) pp. 425–434.

[6] R. M. Merks, S. V. Brodsky, M. S. Goligorksy, S. A. Newman, and J. A. Glazier, *Cell elongation is key to in silico replication of in vitro vasculogenesis and subsequent remodeling,* Developments in Biologicals **289**, 44 (2006).

[7] R. M. H. Merks and J. A. Glazier, *Dynamic mechanisms of blood vessel growth,* Nonlinearity **19**, C1 (2006).

[8] F. Vermolen and A. Gefen, *A semi-stochastic cell-based formalism to model the dynamics of migration of cells in colonies,* Biomechanics and modeling in mechanobiology **11**, 183 (2012).

[9] F. Vermolen and O. van Rijn, *A mathematical model for wound contraction and angiogenesis,* (2012).

[10] D. Form, B. Pratt, and J. Madri, *Endothelial cell proliferation during angiogenesis. in vitro modulation by basement membrane components.* Laboratory investigation; a journal of technical methods and pathology **55**, 521 (1986).

[11] H. H. Marti and W. Risau, *Angiogenesis in ischemic disease,* THROMBOSIS AND HAEMOSTASIS-STUTTGART- **82**, 44 (2000).

[12] D. Bray, *Cell movements: from molecules to motility* (Garland Science, 2001).

[13] A. Gamba, D. Ambrosi, A. Coniglio, A. De Candia, S. Di Talia, E. Giraudo, G. Serini, L. Preziosi, and F. Bussolino, *Percolation, morphogenesis, and burgers dynamics in blood vessels formation,* Physical review letters **90**, 118101 (2003).

[14] G. Serini, D. Ambrosi, E. Giraudo, A. Gamba, L. Preziosi, and F. Bussolino, *Modeling the early stages of vascular network assembly,* The EMBO Journal **22**, 1771 (2003).

[15] D. e. a. Horstmann, *From 1970 until present: the keller-segel model in chemotaxis and its consequences,* (2003).

[16] R. M. H. Merks, E. D. Perryn, A. Shirinifard, and J. A. Glazier, *Contact-inhibited chemotaxis in de novo and sprouting blood-vessel growth,* PLoS Computational Biology **4**, e1000163 (2008).

[17] R. B. Vernon and E. H. Sage, *Between molecules and morphology. extracellular matrix and creation of vascular form.* The American journal of pathology **147**, 873 (1995).

[18] P. Namy, J. Ohayon, and P. Tracqui, *Critical conditions for pattern formation and in vitro tubulogenesis driven by cellular traction fields,* Journal of Theoretical Biology **227**, 103 (2004).

[19] D. Manoussaki, S. Lubkin, R. Vemon, and J. Murray, *A mechanical model for the formation of vascular networks in vitro,* Acta Biotheoretica **44**, 271 (1996).

[20] D. Manoussaki, *A mechanochemical model of angiogenesis and vasculogenesis,* ESAIM: Mathematical Modelling and Numerical Analysis **37**, 581 (2003).

[21] C. A. Reinhart-King, M. Dembo, and D. A. Hammer, *Cell-cell mechanical communication through compliant substrates,* Biophysical journal **95**, 6044 (2008).

[22] M. G. Urbanchek, E. B. Picken, L. K. Kalliainen, and W. M. Kuzon, *Specific force deficit in skeletal muscles of old rats is partially explained by the existence of denervated muscle fibers,* The Journals of Gerontology Series A: Biological Sciences and Medical Sciences **56**, B191 (2001).

[23] N. Chen, J. A. Glazier, J. A. Izaguirre, and M. S. Alber, *A parallel implementation of the cellular potts model for simulation of cell-based morphogenesis,* Computer physics communications **176**, 670 (2007).

[24] T. Alarcón, H. M. Byrne, P. K. Maini, and J. Panovskac, *Mathematical modelling of angiogenesis and vascular adaptation,* Studies in Multidisciplinarity **3**, 369 (2005).

[25] E. Gaffney, K. Pugh, P. Maini, and F. Arnold, *Investigating a simple model of cutaneous wound healing angiogenesis,* Journal of mathematical biology **45**, 337 (2002).

[26] A. R. Anderson and M. Chaplain, *Continuous and discrete mathematical models of tumor-induced angiogenesis,* Bulletin of mathematical biology **60**, 857 (1998).

[27] M. Orme and M. A. Chaplain, *Two-dimensional models of tumour angiogenesis and anti-angiogenesis strategies,* Mathematical Medicine and Biology **14**, 189 (1997).

[28] H. A. Levine, S. Pamuk, B. D. Sleeman, and M. Nilsen-Hamilton, *Mathematical modeling of capillary formation and development in tumor angiogenesis: penetration into the stroma,* Bulletin of mathematical biology **63**, 801 (2001).

[29] F. Vermolen, *Simplified finite-element model for tissue regeneration with angiogenesis,* Journal of engineering mechanics **135**, 450 (2009).

[30] R. C. Schugart, A. Friedman, R. Zhao, and C. K. Sen, *Wound angiogenesis as a function of tissue oxygen tension: a mathematical model,* Proceedings of the National Academy of Sciences **105**, 2628 (2008).

[31] C. Xue, A. Friedman, and C. K. Sen, *A mathematical model of ischemic cutaneous wounds,* Proceedings of the National Academy of Sciences **106**, 16782 (2009).

[32] F. Vermolen and E. Javierre, *A finite-element model for healing of cutaneous wounds combining contraction, angiogenesis and closure,* Journal of mathematical biology **65**, 967 (2012).

[33] S. Maggelakis, *Modeling the role of angiogenesis in epidermal wound healing,* (2003).

[34] F. Vermolen and A. Gefen, *A phenomenological model for chemico-mechanically induced cell shape changes during migration and cell–cell contacts,* Biomechanics and modeling in mechanobiology **12**, 301 (2013).

[35] R. Merkel, N. Kirchgeßner, C. M. Cesa, and B. Hoffmann, *Cell force microscopy on elastic layers of finite thickness,* Biophysical journal **93**, 3314 (2007).

[36] A. Gefen, *Effects of virus size and cell stiffness on forces, work, and pressures driving membrane invagination in a receptor-mediated endocytosis,* Journal of biomechanical engineering **132**, 084501 (2010).

[37] C. A. Reinhart-King, M. Dembo, and D. A. Hammer, *Endothelial cell traction forces on rgd-derivatized polyacrylamide substrata,* Langmuir **19**, 1573 (2003).

[38] F. Vermolen and A. Gefen, *A semi-stochastic cell-based model for in vitro infected 'wound'healing through motility reduction: A simulation study,* Journal of Theoretical Biology **318**, 68 (2013).

[39] v. d. M. R. v. E. M. G. A. W. D. Vermolen, F. J., *Towards a mathematical formalism for semi-stochastic cell-level computational models for tumor initiation,* Annals of Biomedical Engineering (2013).

[40] A. G. M. Dudaie, F.J. Vermolen, *Modeling the migration behavior of cell colonies in two- and three dimensions,* (2014).

[41] K. L. Johnson and K. L. Johnson, *Contact mechanics* (Cambridge university press, 1987).

[42] T. G. Kuznetsova, M. N. Starodubtseva, N. I. Yegorenkov, S. A. Chizhik, and R. I. Zhdanov, *Atomic force microscopy probing of cell elasticity,* Micron **38**, 824 (2007).

[43] A. Ganz, M. Lambert, A. Saez, P. Silberzan, A. Buguin, R. M. Mège, and B. Ladoux, *Traction forces exerted through n-cadherin contacts,* Biology of the Cell **98**, 721 (2006).

[44] S. L. Rowe, S. Lee, and J. P. Stegemann, *Influence of thrombin concentration on the mechanical and morphological properties of cell-seeded fibrin hydrogels,* Acta biomaterialia **3**, 59 (2007).

[45] Y. Zhu, Z. Dong, U. C. Wejinya, S. Jin, and K. Ye, *Determination of mechanical properties of soft tissue scaffolds by atomic force microscopy nanoindentation,* Journal of biomechanics **44**, 2356 (2011).

[46] M. Plank, B. Sleeman, and P. Jones, *A mathematical model of an in vitro experiment to investigate endothelial cell migration,* Computational and Mathematical Methods in Medicine **4**, 251 (2002).

[47] A. L. Bauer, T. L. Jackson, and Y. Jiang, *Topography of extracellular matrix mediates vascular morphogenesis and migration speeds in angiogenesis,* PLoS computational biology **5**, e1000445 (2009).

[48] T. Miura and R. Tanaka, *In vitro vasculogenesis models revisited-measurement of vegf diffusion in matrigel,* Mathematical Modelling of Natural Phenomena **4**, 118 (2009).

[49] M. Lutolf, J. Lauer-Fields, H. Schmoekel, A. Metters, F. Weber, G. Fields, and J. Hubbell, *Synthetic matrix metalloproteinase-sensitive hydrogels for the conduction of tissue regeneration: engineering cell-invasion characteristics,* Proceedings of the National Academy of Sciences **100**, 5413 (2003).

[50] V. L. Streeter, E. B. Wylie, and K. W. Bedford, *Fluid mechanics, wcb,* (1998).

[51] P. Ehrlich, S. Shulman, and J. D. Ferry, *The conversion of fibrinogen to fibrin. viii. sedimentation and viscosity studies on clotting systems inhibited by urea and on solutions of fibrin in urea1, 2,* Journal of the American Chemical Society **74**, 2258 (1952).

[52] M. Hellström, L.-K. Phng, J. J. Hofmann, E. Wallgard, L. Coultas, P. Lindblom, J. Alva, A.-K. Nilsson, L. Karlsson, N. Gaiano, *et al.*, *Dll4 signalling through notch1 regulates formation of tip cells during angiogenesis,* Nature **445**, 776 (2007).

[53] E. Dejana, *Endothelial cell–cell junctions: happy together,* Nature Reviews Molecular Cell Biology **5**, 261 (2004).

[54] I. Holand and K. Bell, *Finite element methods in stress analysis* (Tapir, 1970).

[55] Q. Fang and D. A. Boas, *Tetrahedral mesh generation from volumetric binary and grayscale images,* in *Biomedical Imaging: From Nano to Macro, 2009. ISBI'09. IEEE International Symposium on* (IEEE, 2009) pp. 1142–1145.

[56] E. Cuthill and J. McKee, *Reducing the bandwidth of sparse symmetric matrices,* in *Proceedings of the 1969 24th national conference* (ACM, 1969) pp. 157–172.

[57] V. John and P. Knobloch, *On spurious oscillations at layers diminishing (sold) methods for convection–diffusion equations: Part i–a review,* Computer Methods in Applied Mechanics and Engineering **196**, 2197 (2007).

[58] T.-P. Fries and H. G. Matthies, *A review of petrov–galerkin stabilization approaches and an extension to meshfree methods,* Technische Universitat Braunschweig, Brunswick (2004).

[59] V. John and E. Schmeyer, *On finite element methods for 3d time-dependent convection-diffusion-reaction equations with small diffusion,* in *BAIL 2008-Boundary and Interior Layers* (Springer, 2009) pp. 173–181.